THEORETICAL STUDIES OF HYDROGEN-BONDED CLUSTERS

by

Richard A. Christie

B. Sc. Applied Chemistry

Robert Gordon Universtry

1997

Submitted to the Graduate Faculty of

the Department of Chemistry in partial fulfillment

of the requirements for the degree of

Doctor of Philosophy

University of Pittsburgh

2004

UNIVERSITY OF PITTSBURGH

DEPARTMENT OF CHEMISTRY

This dissertation was presented

by

Richard A. Christie

It was defended on

December 7th, 2004

and approved by

Kenneth D. Jordan, Ph. D.

Rob D. Coalson, Ph. D.

David Pratt, Ph. D.

Jeffry Madura, Ph. D. (Duquesne University)

Dissertation Director: Kenneth D. Jordan, Ph. D.

THEORETICAL STUDIES OF HYDROGEN-BONDED CLUSTERS

Richard A. Christie, PhD

University of Pittsburgh, 2004

Recent experimental findings and theoretical predictions have stimulated considerable interest in the properties of Hydrogen-bonded clusters. In this dissertation, the water hexamer $(H_2O)_6$ and small protonated water clusters $H^+(H_2O)_n$ $(n = 4, 5, 6, 8, 21)$ are investigated by theoretical means. $H^+(H_2O)_5$ is the smallest protonated water cluster with a H_2O molecule in the secondary solvation shell of H^+, and is investigated here with a variety of model potentials, density functionals and large basis set MP2 calculations. Upon inclusion of zero-point energy, the global minimum structure of $H^+(H_2O)_5$ can be considered as the Eigen-cation with a H_2O H-bonded to a first-solvation shell molecule. Analysis of the harmonic vibrational spectra of energetically low-lying $H^+(H_2O)_{4,5}$ isomers reveals the spectroscopic signatures for the proton solvated in both the Eigen and Zundel forms. The parallel tempering Monte Carlo method is used to explore the configuration space of $H^+(H_2O)_6$ and $H^+(H_2O)_8$ for the lowest-lying isomers, and to simulate the finite temperature properties of these clusters. A property of particular interest is the phase-change behavior of $n = 6, 8$. The dependence of the isomer populations of both $n = 6$ and 8 with temperature is found to be in good agreement with the recent experimental findings of Jiang *et al.* [*J. Am. Chem. Soc.* **2000**, *122*, 1398]. The thermodynamic behavior of the $(H_2O)_6$ cluster has been the subject of several theoretical studies employing model potentials. However, the results from these investigations vary considerably due to the different model potentials employed. New results are presented from studies employing an *ab initio* intermolecular potential. Canonical Monte Carlo simulations using a 2+3-body MP2-level potential are combined with finite histogram method of Ferrenberg and Swendsen [*Phys. Rev. Lett.* **1988**, *61*, 2635] to simulate the finite temperature

properties of $(H_2O)_6$. The *magic number* behavior of $H^+(H_2O)_{21}$ has stirred debate in the literature since the initial report by Searcy and Fenn [*J. Chem. Phys.*, **1974**, *61*, 5282]. The OH stretching vibrational spectra for the $6 \leq n \leq 27$ clusters are analyzed with the aid of MP2-level calculations, and a dodecahedral-based configuration for $n = 21$ is confirmed.

TABLE OF CONTENTS

LIST OF TABLES

LIST OF FIGURES

PREFACE

I would like to thank my advisor Prof. Kenneth D. Jordan for all his help and mentoring these past years. This dissertation is dedicated to my wife Maria for her seemingly limitless patience and support.

1.0 INTRODUCTION

1.1 ATOMIC AND MOLECULAR CLUSTERS

Atomic and molecular clusters are defined as the aggregation of a finite number of constituent components, N. In clusters, N can vary in magnitude anywhere from 2 through 10^4, and thus clusters are considered an intermediate form of matter, lying between that of independent atoms/molecules ($N = 1$) and bulk matter ($N \rightarrow \infty$). Clusters are further classified by both their means of preparation, and the interparticle forces which bind the constituent atoms or molecules together.[1] For example, $(KCl)_{32}$ can be formed by laser ablation of the bulk solid and is stabilized by the electrostatic attraction between K^+ and Cl^- ions. Perhaps the most thoroughly studied of all clusters thus far is Buckminsterfullerene, which can be prepared in the laboratory by laser ablation of graphite and consists of sixty covalently bonded Carbon atoms.

The field of cluster science now encompasses a wide range of classes of clusters, varying in the type and number of constituent components[1,2,3,4,5] The studies presented in this dissertation, however, are concerned with one class of molecular clusters; small hydrogen-bonded clusters comprised of closed shell molecules, such as $(H_2O)_n$ and $H_3O^+(H_2O)_n$ which are prepared in the gaseous state.

The field of atomic and molecular clusters has expanded and matured considerably in recent years. The investigation of clusters is motivated by several reasons. One such motivation is perhaps the most classical; scientific curiosity about the fundamental nature of matter. In the natural world, clusters have been found to be important species in the chemistry of a wide range of environments; from interstellar space,[6] to the upper atmosphere of earth.[7,8]

Another motivation for studying clusters is the interesting intrinsic properties of the systems themselves. Experimental studies have uncovered phenomena unique to clusters such as *magic number* behavior, in which one particular cluster size is found to dominate the mass spectrum of an ensemble of clusters. For example, Wei *et al.*[9] found $H_3O^+(H_2O)_{20}$ to be considerably more stable than other cluster sizes and proposed a configuration to account for this stability. Theoretical simulations have predicted that some clusters undergo *phase changes* in analogy with the phase transitions of infinite systems. However, in contrast with the bulk, these phase-changes occur over a range of temperatures and involve "slush-like" states[10] which involve both the solid-like and liquid-like phases.

Clusters also provide an accessible means of achieving a deeper understanding of the properties of condensed matter without some of the complications of the bulk phase. A direct outcome of the intense research in cluster physics over the last decade has been the development and maturation of the field of *energy landscape theory* where amongst other successes, a thorough insight into cluster potential energy surfaces has lead to an enchanced understanding of the conformational folding of biomolecules (*e.g.*, see Wales[11]).

A further motivation for studying clusters is related to their unique properties. These properties are foreseen to potentially give rise to a variety of technological uses. For example, the structural properties of C_{60} have led to the prediction that it is to be an important component of Drexler's *Nanotechnology revolution*.[12] The size-dependent melting temperature property of clusters has led to the proposed use of clusters as site-specific drug delivery agents.[13] Another application of clusters as highly specific catalysts has been suggested from their size-dependent electronic properties.[14]

While it is widely believed that cluster science will play an important role in the development of future technologies, the current state of the field owes much to the rapid technological evolution of the last decades. The developments in cluster science are strongly correlated to the technological advances. As the technology behind experimental and theoretical studies has improved, a deeper insight into the nature of clusters has been made possible. Such insight has, in turn, stimulated further studies to understand newly found phenomena. Experimental advances have come about through improvements in cluster generation technology together with amazing developments in investigation and detection hardware.[1,2] It is now

possible to create a wider range of cluster-types, with a more size specific size selectivity and characterize them with more detail and accurate probing than was feasible when the first cluster studies began. For example, early studies carried out on protonated water clusters in the late 1960s were limited to estimations of hydration enthalpies of an ensemble of cluster sizes, whereas experimental studies carried out three decades later could identify individual structural configurations of highly size-selected clusters by means of an accurate analysis of the cluster vibrational modes.

From the theoretical standpoint, many of the advances in understanding clusters have been correlated to Moore's Law of device integration in computer chips (*e.g.*, see Turton[15]). As a representative example, early computational investigations into the nature of protonated water clusters were limited to rather inaccurate methods and small systems. In more recent years, chemically accurate (*i.e.*, errors less than 1 kcal/mol in magnitude) methods have been applied to smaller N clusters, and the studies extended to investigating the finite temperature properties of these clusters. Such demanding computations have only been possible through advances in computer hardware, such as CPU clock speed and the development of parallel architectures, together with algorithm advances.

Theoretical methods have proven to be an indispensible complement to the experimental studies of clusters. Cluster energetics, such as the relative energies of stable isomers and barriers to isomerization, as well as the finite temperature properties are difficult to analyze in the laboratory. However, theoretical methods are particularly suited to studying cluster properties such as these. For example, the splitting in the peaks of vibrational-rotational spectra of water clusters found by Liu *et al.*[16] have been explained by means of computational studies of the cluster rearrangement pathways by Wales *et al.*[17]

1.2 PROTONATED WATER CLUSTERS

Protonated water clusters are comprised of neutral water molecules with an excess proton, H^+. In aqueous solution or water cluster, the highly reactive H^+ immediately associates with the oxygen atom of a neighbouring water molecule. A common form for the solvated

proton is the *oxonium* or *hydronium* ion, H_3O^+,[18] and hence protonated water clusters are often defined in the literature as $H_3O^+(H_2O)_n$. At the same time however, protonated water clusters are also denoted as $H^+(H_2O)_{(n+1)}$; the use of different nomenclatures is a manifestation of the historical uncertainty about the exact nature of the solvated proton.

Protonated water clusters are thought to be present in a wide range of natural environments. Duley[6] has proposed that protonated clusters form in interstellar gas clouds by cosmic-ray heating of dust grains. Furthermore, Duley[6] speculates that these interstellar clusters may act as a seed for accretion of carbon-based clusters and molecules.[19]

$H_3O^+(H_2O)_n$ clusters have also been found to be an influential element in the chemistry of the upper atmosphere.[7] Indeed, Schindler *et al.*[8] have proposed that protonated water clusters could act as a catalyst for the annual depletion of stratospheric ozone over the Antarctic. The chemistry of the ionosphere has been shown to be strongly influenced by the abundant presence of $H_3O^+(H_2O)_n$[20,21] in this region of the atmosphere.

Another important role of protonated water clusters is in the restricted spaces and cavities of proteins and biomolecules. For example, Baciou and Michel[22] found that water chains in *Rhodobacter sphaeroides* were a crucial component in the photosynthetic ability of the purple bacteria. *Rhodobacter sphaeroides* produces electrochemical energy by a series of photon induced electron- and proton-transfers; the water chain in the photosynthesis reaction center serves as a conduit for the proton migration from one part of the reaction center to another. Chain-like protonated water clusters are believed to be crucial to proton transfer events in biomolecules.[23]

The field of protonated water cluster studies first emerged amid a climate of intense interest in solvated protons in the bulk liquid phase (*e.g.*, see Schuster *et al.*[24,25]). A unifying interest of these studies was the structural nature of the solvated proton and deeper insight into the mechanism[26] for the anomalously high mobility (*e.g.*, see Atkins[27]) for the proton in aqueous solution. Two important solvation models for H^+ were discussed in the literature; the *Eigen*[18,28,29] and *Zundel*[30,31,32,33] models. The Eigen model considers the proton localized in a hydronium molecule with each equivalent H in H_3O^+ donating a H-bond to solvating H_2O molecules, giving a $H_9O_4^+$ species. In the Zundel model, the proton is delocalized between two water molecules in a $H_5O_2^+$ species. Much of the subsequent work in the following decades

focussed on identifying and characterizing these $H_9O_4^+$ and $H_5O_2^+$ species.

Despite the future interest in protonated water clusters, and the discovery of $H^+(H_2O)_n$ in a wide range of natural environments, some of the earliest investigations of protonated water clusters actually came about by accident. Kebarle and Godbole[34] unexpectedly discovered the presence of protonated water clusters when studying ion-molecule reactions involving a trace quantity of water vapour. This discovery came about a decade after the influential work of Eigen and co-workers on the solvation of H^+ in bulk liquid water,[18,28,29] and around the same time period as the work of Zundel.[30,31,32,33] The discovery of $H_3O^+(H_2O)_n$ gave rise to the opportunity of studying the nature of the solvated H^+ with relatively little interference from the bulk solution water molecules, and thus greater insight into the recently proposed solvation models of Eigen and Zundel.

Following their initial discovery, the Kebarle group[34,35,36,37] studied the energetics and kinetics of protonated water cluster hydration using the mass spectometry of an ion source. From the resulting ion intensities, Kebarle *et al.*[36] estimated the cluster partial pressures and thus could calculate the cluster ΔG and ΔH for the hydration reactions

$$H_3O^+(H_2O)_n + H_2O \rightarrow H_3O^+(H_2O)_{(n+1)}. \tag{1.1}$$

For the simplest $n = 0$ reaction, Kebarle *et al.*[36] calculated an enthalpy of $\Delta H = -36$ kcal/mol, a value in suprisingly good agreement with recent theoretical predictions[38] of $\Delta H = -34.4$ kcal/mol. These findings were not universally accepted, and a later study by the same group[37] was carried out in response to the conflicting results of Beggs and Field[39] and the Friedman group.[40,41] In their later study,[37] the calculated enthalpy for the $n = 0$ reaction of Equation 1.1 was determined to be $\Delta H = -31.6$ kcal/mol.

The next major development in the field of protonated water clusters occurred when the vibrational spectra of the small clusters, $H_3O^+(H_2O)_n$, $n = 1, 6$, were first recorded by Schwarz[42] in 1977 using a pulsed radiolysis ion source. The vibrational modes were assigned with the assistance of complementary *ab initio* calculations by Newton.[43] The findings of Schwarz[42] included the identification of peaks at 3000 and 2660 cm^{-1} corresponding to the signature symmetric and asymmetric stretches of H_3O^+, respectively. Distinct bands of the $H_3O^+(H_2O)_4$ cluster were also found at 2180, 2860 and 3200 cm^{-1}. The work of

Schwarz[42] and Newton[43] also provided information on the extended solvation structure of H^+. Vibrational bands found at 3170 and 3620 cm^{-1} were predicted to have arisen from molecules in the secondary solvation shell of H_3O^+.

The first mass selected studies on protonated water clusters were carried out by Y. T. Lee and coworkers using vibrational predissociation spectroscopy.[44,45,46,47] This newly developed instrumentation allowed for a more accurate insight into the vibrational spectra of $H_3O^+(H_2O)_n$, $n = 1, 3$, although no structural assigments were made. The first successful structural assignments from mass-selected vibrational spectra was achieved by the same group[48] in 2000. In this latter study, the spectroscopic evidence for the Zundel entity $H_5O_2^+$ in the gas phase (in $H^+(H_2O)_6$) was identified for the first time.

Considerable experimental and theoretical work has also been carried out on the larger protonated water clusters. Motivation for much of this work was the pioneering $H_3O^+(H_2O)_{20}$ *magic number* studies of the Fenn[49] and Castleman groups[9] in which a dodecahedron-based structure was used to account for the unique stability of this cluster. The deduction of a dodecahedral structure for $H_3O^+(H_2O)_{20}$ linked the study of protonated water clusters with another field of study; clathrates. Clathrates are crystal structures in which a dodecahedral-cage structure surrounds a host molecule such as methane (*e.g.*, see Sloan[50]), and are of considerable interest to chemical and petroleum engineers.

Amongst the early theoretical work on protonated clusters were *ab initio* studies on $H_5O_2^+$ by Kraemer[51] and Kollman[52] and a CNDO/2 semi-empirical investigation by De Paz.[53] The primary focus of these early works, and the influential studies of Newton and Ehrenson[54] concerned the solvation structure of the solvated proton, and the reproduction of the aforementioned experimental reaction enthalpies of the Kebarle[36,37] and Friedman groups.[40,41] As mentioned previously, the vibrational spectra of Schwarz[42] were interpreted by *ab initio* calculations of Newton,[43] who also considered some important properties of protonated water clusters, such as the Grotthuss mechanism of proton transfer.[26,55]

The early theoretical work[43,52,54] on protonated water clusters, together with the experimental findings of the Lee group[44,45,46,47] stimulated considerable interest in the nature of $H_5O_2^+$ throughout the 1980s and 1990s.[56,57,58] An interesing feature of these studies was that SCF treatments predicted a C_s global minimum structure, whereas methods including

correlation predicted a C_2 configuration. It was not until the CCSD(T)/TZP studies of Xie *et al.*[59] and Valeev and Schaefer[60] in the mid to late 1990s that the global minimum of $H_5O_2^+$ was indeed proven to be a C_2 structure.

Theoretical interest in the smaller protonated clusters, $H_3O^+(H_2O)_n$, $n = 1, 4$, began to increase in the early nineties through the work of Rahmouni *et al.*[61] and Corongiu *et al.*[62] The former of these studies occured 5 years after the 1985 British Antarctic Survey discovered the hole in the Ozone layer (and 3 years after the *Montreal Protocol on Substances That Deplete the Ozone Layer*[63] was first published) during a time of considerable interest in the chemistry of the upper atmosphere. At this time, there was considerable speculation that protonated water species played an important role in the mechanism for stratospheric Ozone depletion. A primary concern of these investigations, apparently unresolved since the study of Newton,[43] was whether or not there existed stable clusters with four water molecules in the first solvation shell of H_3O^+. Corongiu *et al.*[62] employed a Monte Carlo simulation to sample the configuration space of $H_3O^+(H_2O)_4$, and density functional theory to optimize and characterize the structural minima.

The next development in protonated water cluster studies was the investigation of clusters larger than $H_5O_2^+$, and the study of the finite temperature properties of these clusters. An extensive *ab initio* study of $H_5O_2^+$ and $H_3O^+(H_2O)_3$ was carried out by Ojamäe *et al.*,[38] including the incorporation of anharmonic effects in the vibrational spectra and a detailed study of the low-lying regions of the potential energy surface of $H_5O_2^+$. The continuation of this study led to the construction of a model potential for $H_3O^+(H_2O)_n$ by Ojamäe *et al.*,[64] and the application of this potential to study some of the thermodynamics of $H_3O^+(H_2O)_7$ by Ciobanu *et al.*[65] and $H_3O^+(H_2O)_{15}$ by Singer *et al.*[66]

Further interest in the finite temperature properties of protonated water clusters led to the development of several new model potentials. In comparison with model potentials for noble gases or neutral water, protonated water clusters are inherently more difficult to treat. This is due to the distinguishing property of protonated water clusters; the high mobility of H^+ being difficult to treat with an analytical model potential. Protonated water cluster model potentials must be able to treat not only the intermolecular forces, but also the breaking of chemical bonds (*i.e.*, in $H_2O\cdots H\text{–}OH_2$). For this reason, the use of an "on-

the-fly" forcefield has been employed by Chandler and coworkers.[67] Early protonated water cluster model potentials included those of Stillinger and Weber,[68] Kozack and Jordan[69] and Halley *et al.*[70] which were all based upon a dissociative model approach. The potentials of Lobaugh and Voth,[71] Sagnella and Tuckerman,[72] Schmitt and Voth[73,74] and Vuileimer and Borgis[75,76] were developed using a different approach, the Empirical Valence Bond (EVB) method of Warshel.[77] The model potentials of Hodges and Stone[78] and Shevkunov and Vegiri[79,80] were based upon a more traditional rigid-molecule approach, and thus cannot model proton transfer events. The development of treating protonated water clusters remains an area of extensive current interest.

2.0 THEORETICAL INVESTIGATION OF $H_3O^+(H_2O)_4$

This work was published as

Christie, R. A.; Jordan, K. D. *J. Phys. Chem. A* **2001**, *105*, 7551

2.1 ABSTRACT

The low-lying minima on the Born-Oppenheimer potential energy surface of the $H_3O^+(H_2O)_4$ cluster are investigated by effective valence bond (EVB), density functional, and MP2 methods. Although Becke3LYP and MP2 calculations predict the same global minimum structure, the relative energies of various structures obtained by these two approaches differ by up to 1.7 kcal/mol. Even larger differences are found between the relative energies calculated at the EVB and MP2 levels of theory. Vibrational spectra are calculated for each of the minimum energy species.

2.2 INTRODUCTION

Small protonated water clusters have been the subject of numerous theoretical studies.[38,43,54,60,62,64,67,69,70,72,74,75,76,78,81,82,83,84,85,86] While the Born-Oppenheimer potential energy surface for the $H_3O^+(H_2O)_n$, $n = 1 - 3$, clusters are fairly well characterized, much less is known about the larger protonated water clusters. In this work we consider the $H_3O^+(H_2O)_4$ system, which is of particular interest in that it is the smallest protonated water cluster with a water molecule outside the first solvation shell of H_3O^+.[54] The pertur-

bation of the first solvation shell by surrounding solvent molecules is a vital phenomenon in aqueous phase chemistry and biology, and has been invoked to account for the anomolously high rate of proton transfer in bulk water.[84]

In this study five potential energy minima of $H_3O^+(H_2O)_4$ (see Figures 1-5) have been characterized. Four of these (**I**, **II**, **IV** and **V**) were considered in earlier theoretical studies.[62,78] Species **III** is reported here for the first time. In isomers **I**, **II**, and **III** the H_3O^+ entity is directly bonded to three water monomers, and in **IV** and **V** it is bonded to two water monomers. **I-III** can be viewed as Eigen-like[28] $H_9O_4^+$ ions solvated by an additional water monomer. In **I**, the H_3O^+ is incorporated into a four-membered ring and is bonded to two waters in the ring as well as to a non-ring water. **II** and **III**, which may be viewed as an $H_9O_4^+$ ion solvated by a H_2O molecule, can interconvert by inversion of the central H_3O^+ species. **IV** is a chain-like structure with the H_3O^+ located in the middle of the chain, and **V** has a five-membered ring structure.

The most thorough earlier theoretical studies of $H_3O^+(H_2O)_4$ are those of Hodges and Stone[78] and Corongiu *et al.*.[62] Whereas Hodges and Stone employed a model potential to describe the cluster, Corongiu *et al.*[62] used density functional theory (DFT) with the Becke-Perdew (BP) exchange correlation functional.[87,88,89] Both of these approaches predict the global minimum structure to be **I**, with the next most stable structure (**II**) lying about 1.5 kcal/mol higher in energy. The relative stabilities predicted by these calculations cannot be viewed as conclusive as the BP functional used by Corongiu *et al.*[62] considerably overestimates H-bond strengths in water clusters[90,91,92,93] and the model potential of Hodges and Stone employs a rigid H_3O^+ entity.

In the present work three additional theoretical methods are brought to bear on the $H_3O^+(H_2O)_4$ system. These include second-order many-body perturbation theory (MP2), density functional theory with the Becke3LYP exchange-correlation functional[94,95,96] and the multistate empirical valence bond (MSEVB) approach of Schmitt and Voth.[74] Previous studies have proven that the MP2 method allows an accurate characterization of smaller $H_3O^+(H_2O)_n$ clusters.[38,56,64] Hence, comparison with the MP2 results will prove valuable in assessing the reliability of the Hodges-Stone[78] and MSEVB model potential approaches as well as of the BP and Becke3LYP density functional methods for describing $H_3O^+(H_2O)_4$

and larger protonated water clusters.

2.3 METHODOLOGY

The geometries of the clusters were first optimized using the MSEVB[74] method, combined with a Monte Carlo quenching procedure. The MSEVB approach has been described in detail in Schmitt and Voth,[74] and here we note only that it combines a modified non-rigid monomer TIP3P[97] model potential for describing the $H_2O\cdots H_2O$ interactions and a parameterized valence bond treatment of the $H_3O^+\cdots H_2O$ interactions. Starting from the MSEVB structures, the geometries were then optimized at both the Becke3LYP and MP2 levels of theory using the aug-cc-pVDZ basis set.[98,99]

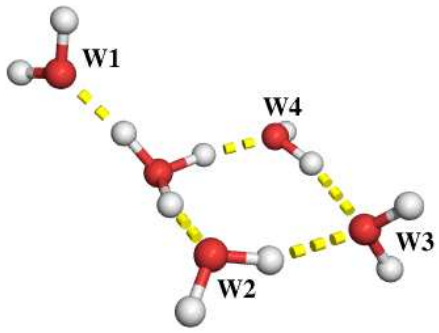

Figure 1: $H_3O^+(H_2O)_4$ MP2/aug-cc-pVDZ minimum **I**

In order to determine whether differences in the relative energies obtained at the B3LYP and MP2 levels of theory were due to the differences in the geometries, single-point MP2/aug-cc-pVDZ calculations were carried out at the B3LYP potential energy minima. To check the convergence of the results with the respect to the atomic basis set, MP2 calculations were carried out using the larger aug-cc-pVTZ basis set.[98,99]

As is well known, basis set superposition error (BSSE) can cause interaction energies to be overestimated. Corrections for BSSE have been estimated by use of the counterpoise procedure.[100] In order to obtain insight into the nature of the interactions for each cluster,

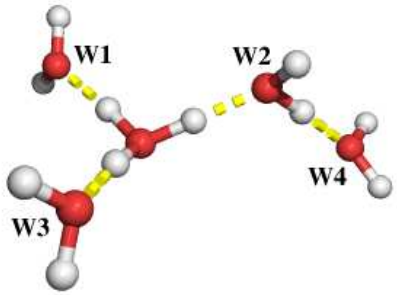

Figure 2: $H_3O^+(H_2O)_4$ MP2/aug-cc-pVDZ minimum **II**

the net MP2 interaction energies were decomposed into their n-body (n = 2, 3, 4 and 5) contributions. This was accomplished by carrying out calculations on appropriate fragment combinations as will be described in more detail below.

The relative energies obtained from the Becke3LYP/aug-cc-pVDZ calculations were found to differ appreciably from the BP results of Corongiu *et al.*[62] However there are two major differences between these two DFT calculations: (1) the exchange-correlation functionals differ, and (2) the basis set used for our calculations contains diffuse functions, whereas that used by Corongiu *et al.*[62] did not. To determine which of these two factors is responsible for the discrepancies between the two sets of DFT results, we also undertook BP calculations using both the cc-pVDZ basis set which lacks diffuse functions and the aug-cc-pVDZ basis set which includes such functions. These calculations were carried out using the Becke3LYP optimized geometries. Finally the IR spectra were calculated for isomers **I**, **II**, **IV** and **V** using the harmonic approximation and the Becke3LYP/aug-cc-pVDZ procedure.

The electronic structure calculations were performed with the Gaussian 98 program,[96] and the MSEVB calculations were carried out using a program developed in our group.

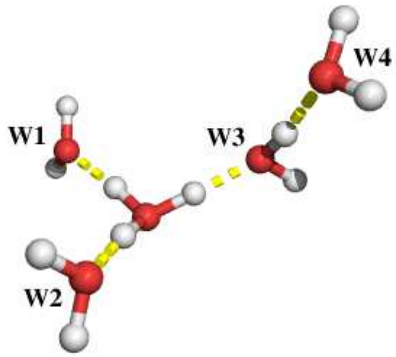

Figure 3: $H_3O^+(H_2O)_4$ MP2/aug-cc-pVDZ minimum **III**

2.4 RESULTS AND DISCUSSION

2.4.1 Energies of the Isomers I-V

Table 1 summarizes the formation energies for the different isomers calculated at the various levels of theory. A subset of the results is also summarized in Figure 6. The formation energies are calculated using

$$\Delta E = E(H_3O^+(H_2O)_4) - E(H_3O^+) - 4 \cdot E(H_2O), \tag{2.1}$$

where $E(H_3O^+(H_2O)_4)$, $E(H_3O^+)$, and $E(H_2O)$ are the energies of the $H_3O^+(H_2O)_4$ cluster, the H_3O^+ ion, and the H_2O molecule, respectively.

The MP2/aug-cc-pVDZ calculations predict that **I** is the global minimum structure, lying energetically about 1.2 kcal/mol below the nearly isoenergetic minima **II** and **III**. At the MP2 level of theory, **IV** and **V** are predicted to be less stable than **I** by 4.68 and 4.27 kcal/mol, respectively.

The formation energies calculated at the MP2/aug-cc-pVTZ level are very close to those obtained at the MP2/aug-cc-pVDZ level, both without correction for BSSE. However, the counterpoise corrections for the BSSE in the MP2 formation energies range from 5.9-6.9 kcal/mol with the aug-cc-pVDZ basis set and from 2.9-3.5 kcal/mol with the aug-cc-pVTZ

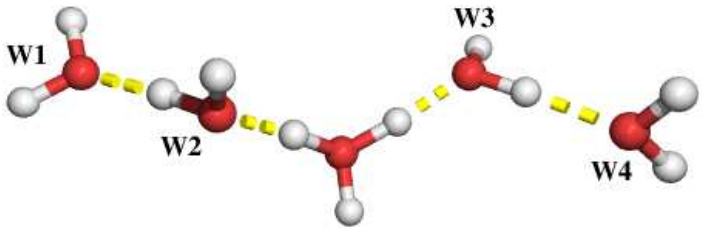

Figure 4: $H_3O^+(H_2O)_4$ MP2/aug-cc-pVDZ minimum **IV**

basis set (see Table 2). Based upon the trends in Table 2, and on the results for neutral water clusters employing still larger basis sets, we expect the complete basis set (CBS) limit MP2 level formation energies to be very close to the uncorrected MP2/aug-cc-pVTZ results. For this reason, unless noted otherwise, in assessing the reliability of the DFT and MSEVB results, comparison will be made with the MP2/aug-cc-pVTZ results.

For **II**, **III** and **IV**, the Becke3LYP and MP2 calculations give similar formation energies. However, for **I** and **V**, the Becke3LYP calculations give formation energies 0.8-0.9 kcal/mol smaller in magnitude than the corresponding MP2 values. As a result, the Becke3LYP calculations predict minima **II** and **III** to be nearly isoenergetic with **I** and predict **IV** to be more stable than **V**, in contrast with the MP2 results. Interestingly, of the five isomers of $H_9O_4^+$, only **I** and **V** have a double-acceptor water monomer. Thus it appears that the Becke3LYP functional is inadequate for describing the interactions involving double-acceptor water molecules. This is consistent with an earlier observation that for $(H_2O)_6$, Becke3LYP calculations incorrectly predict the ring isomer to be more stable than the cage and prism isomers, both of which have double acceptor water molecules.[101] This problem is not unique to the Becke3LYP functional, as similar behaviour is also displayed by BP/aug-cc-pVDZ calculations.

At the Becke3LYP/aug-cc-pVDZ level the inversion barrier of **III** is 0.47 kcal/mol, nearly identical to that (0.52 kcal/mol) for the $H_9O_4^+$ Eigen-like ion. In contrast, the inversion barrier (at the same level of theory) for H_3O^+ is 1.36 kcal/mol.

As is seen from the results in Table 1 and Figure 6, although the BP calculations of

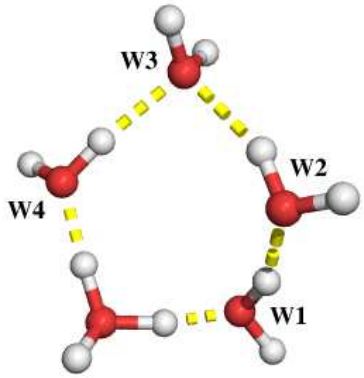

Figure 5: $H_3O^+(H_2O)_4$ MP2/aug-cc-pVDZ minimum **V**

Corongiu *et al.*[62] predict **I** to be the global minimum form of $H_3O^+(H_2O)_4$ in agreement with our MP2 calculations, this agreement is fortuitous, being the result of the use of a basis set lacking diffuse functions. BP calculations with the aug-cc-pVDZ basis set, in fact, predict **II** and **III** to be about 0.2 kcal/mol more stable than **I**.

MP2 calculations using Becke3LYP optimized geometries give relative energies for the different isomers nearly identical to those obtained using MP2 optimized geometries, which is not surprising given that the formation energies for the Becke3LYP calculations are fairly close to the MP2 results.

With the inclusion of counterpoise corrections (Table 2), **I** is predicted, at the MP2/aug-cc-pVTZ level, to be more stable (by $\approx$ 0.7 kcal/mol) than **II**/**III**. The vibrational zero-point energy (calculated using Becke3LYP/aug-cc-pVDZ harmonic frequencies) for **I** is 9.0 kcal/mol, but only about 7.6 to 7.8 kcal/mol for **II** and **III**. When the MP2/aug-cc-pVTZ level formation energies are combined with the B3LYP/aug-cc-pVDZ ZPE corrections, **II** and **III** are predicted to be slightly more stable than **I**.

We now turn our attention to the model potential results. Although the Hodges and Stone (HS) potential underestimates the formation energies by up to about 7.3 kcal/mol, it does a fairly good job at reproducing the relative stabilities obtained at the MP2 level. Presumably, with a more exhaustive search for local minima, isomers **III** and **IV** would be

identified for this potential.

The MSEVB calculations, in contrast to the MP2 calculations, place structures **II** and **III** below **I** (by about 1.0 kcal/mol). They also place **IV** and **V** 3-5 kcal/mol too high in energy, which seems to imply that the MSEVB procedure is biased towards a fully solvated over a partially solvated H_3O^+ ion. We return to this issue in the next section where the individual n-body contributions to the formation energies are examined.

MP2 calculations carried out using the MSEVB geometries underestimate the magnitude of the formation energies by up to 1.8-3.2 kcal/mol (as compared to the results obtained using the MP2 or Becke3LYP optimized geometries). The approximate near constancy of the error introduced by the use of the MSEVB geometries is an encouraging finding as it is much less computationally demanding to optimize structures at the MSEVB than at the MP2 (or Becke3LYP) level of theory.

To elucidate the effect of the secondary solvation shell molecule upon the relative energies, it is instructive to compare the results for the $H_3O^+(H_2O)_4$ cluster with those for the $H_3O^+(H_2O)_3$. To this end, the $H_3O^+(H_2O)_3$ species, **I'**, **II'**, and **IV'**, were optimized at the MP2/aug-cc-pVDZ level of theory. The three unique $H_3O^+(H_2O)_3$ isomers obtained are illustrated in Figure 7-9. **I'** corresponds to minima **I** without the **W1** H_2O monomer (see Figure 1). **II'** is formed by removing the secondary shell water molecule (**W4** in Figure 2) from **II** to leave the Eigen cation. **IV'** corresponds to **IV** with one of the terminal H_2O monomers (**W1** or **W4**) removed. For the $H_3O^+(H_2O)_3$ cluster, the Eigen cation **II'** is predicted to be 4.0 kcal/mol more stable than **I'**. This is in contrast to $H_3O^+(H_2O)_4$ for which **I** is predicted to be more stable than **II**. The reversal of the order of these two structures upon addition of a water monomer is the result of the much greater strength of the $H_3O^+ \cdots H_2O$ interaction compared to the $H_2O \cdots H_2O$ interaction (see Figure 14).

Table 1: Comparison of formation energies (kcal/mol) for the five $H_3O^+(H_2O)_4$ minima calculated using various theoretical methods.[a]

Isomer	MP2/aDZ[b] at MP2	MP2/aTZ[b] at MP2	MP2/aDZ at B3LYP	B3LYP/aDZ at B3LYP	BP[c]	BP86/aDZ at B3LYP	MSEVB	Hodges Stone[d]	MP2/aDZ at MSEVB
I	-92.71	-92.60	-92.67	-91.71	-97.04	-91.56	-91.08	-85.88	-90.54
II	-91.53	-91.72	-91.43	-91.67	-95.36	-91.71	-92.07	-84.43	-89.48
III	-91.58	-91.74	-91.48	-91.63	-	-91.74	-92.01	-	-89.61
IV	-88.03	-88.47	-87.89	-88.76	-92.74	-89.68	-83.96	-	-85.26
V	-88.44	-88.60	-88.27	-87.84	-94.42	-88.53	-85.37	-83.71	-86.77

[a] For those entries with two theoretical methods listed, the first method refers to that used to calculate the energy and the second to the method at which the geometry was optimized. The MP2 and Becke3LYP geometries were optimized using the aug-cc-pVDZ basis set.

[b] aDZ and aTZ denote the aug-cc-pVDZ and aug-cc-pVTZ basis sets, respectively.

[c] From Corongiu *et al.*[62]

[d] From Hodges and Stone.[78]

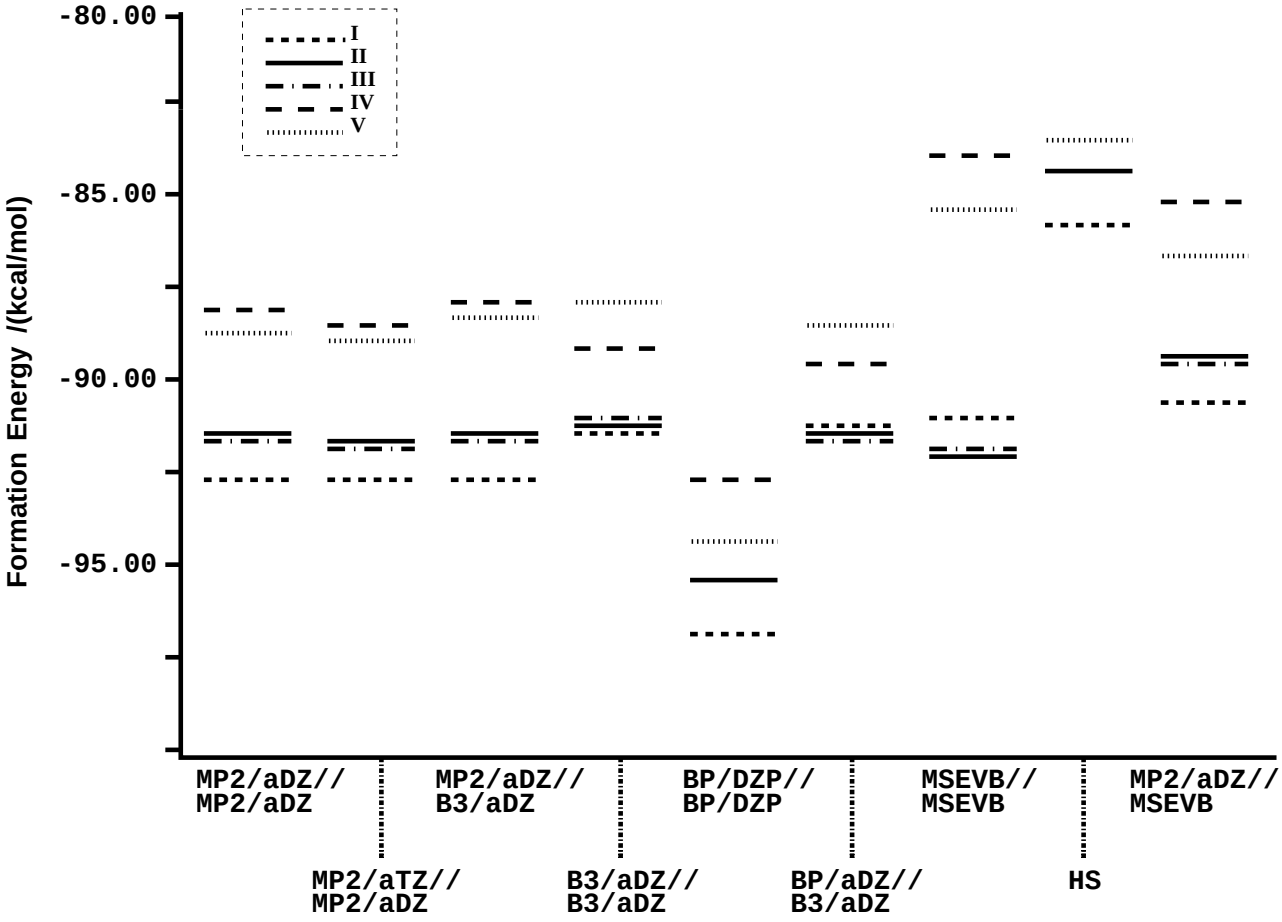

Figure 6: From left to right on absissca; MP2/aDZ//MP2/aDZ, MP2/aTZ//MP2/aVDZ, MP2/aDZ//B3LYP/aDZ, B3LYP/aDZ//B3LYP/aDZ, BP/DZP//BP/DZP, BP86/aDZ//B3LYP/aDZ, MSEVB//MSEVB, HS//HS and MP2/aDZ//MSEVB results respectively, where aDZ and aTZ denote aug-cc-pVDZ and aug-cc-pVTZ respectively, and where the quantity to the left of the double slash indicates the level of theory used to calculate the energies and that to the right, the geometries employed. HS denotes the model potential of Hodges and Stone[78] and the BP/DZP//BP/DZP results are from Corongiu *et al.*[62]

Table 2: MP2 n-body contributions to the formation energies (kcal/mol) for **I**, **II**, **IV** and **V**.

interaction	**I**		**II**		**IV**		**V**	
	aDZ[a]	aTZ[a]	aDZ	aTZ	aDZ	aTZ	aDZ	aTZ
1-body	2.39	2.89	2.88	3.36	6.90	7.60	6.73	7.45
2-body	-107.06	-107.56	-103.81	-104.49	-92.99	-94.19	-96.51	-97.39
	(-100.71)[b]	(-104.41)	(-97.89)	(-101.62)	(-86.81)	(-91.10)	(-89.59)	(-93.91)
3-body	11.59	11.69	9.39	9.36	-3.09	-3.00	0.10	0.12
	(11.69)	(11.71)	(9.47)	(9.44)	(-2.93)	(-2.94)	(0.10)	(0.15)
4-body	0.44	0.43	0.03	0.08	1.13	1.09	1.18	1.19
	(0.41)	(0.42)	(0.07)	(0.07)	(1.07)	(1.07)	(1.14)	(1.13)
5-body	-0.07	-0.05	-0.02	-0.03	0.02	0.03	0.06	0.03
	(-0.05)	(-0.05)	(-0.03)	(-0.03)	(0.02)	(0.03)	(0.05)	(0.05)
net	-92.71	-92.60	-91.53	-91.72	-88.03	-88.47	-88.44	-88.60
	(-86.27)	(-89.44)	(-85.50)	(-88.78)	(-81.75)	(-85.34)	(-81.57)	(-85.13)

[a] The aug-cc-pVDZ and aug-cc-pVTZ basis sets are denoted aDZ and aTZ respectively.

[b] Terms in parenthesis correspond to the counterpoise-corrected values.

2.4.2 n-body Interaction Energies

The Becke3LYP, MP2 and MSEVB interaction energies were decomposed into their various n-body contributions.[101,102] This was accomplished by carrying out calculations on all possible cluster fragments. For example, in order to estimate the two-body interaction energies, calculations were carried out on each $H_3O^+ \cdots H_2O$ and $H_2O \cdots H_2O$ pair, as well as on each monomer in the cluster, using the geometries "extracted" from that of the $H_3O^+(H_2O)_4$ isomer of interest. The two-body contributions to the interaction energies were then calculated by subtracting from the "dimer" energies the appropriate monomer energies. To obtain the three and four-body interaction energies calculations on all trimer and tetramer combinations were required. The n-body decomposition analysis was carried out using both the aug-cc-pVDZ and aug-cc-pVTZ basis sets in the case of the MP2 calculations, but only the aug-cc-pVDZ basis set in the case of the B3LYP calculations. MP2/aug-cc-pVDZ geometries were used in each case, to remove differences caused by variations in the geometries from one theoretical approach to another.

The results of the n-body decomposition calculations are summarized in Tables 2-5. Interaction energies with and without the counterpoise correction for BSSE are reported. The table also reports 1-body relaxation energies which are the energies required to distort isolated H_3O^+ and H_2O species to the geometries they possess in the cluster. We examine first the results from the MP2 calculations summarized in Table 2. In the absence of the counterpoise correction, the individual n-body contributions, and consequently the net interaction energies, are relatively independent of whether the aug-cc-pVDZ or aug-cc-pVTZ basis sets is employed. In particular, the $n \geq 3$ n-body interaction energies calculated with the aug-cc-pVDZ and aug-cc-pVTZ basis sets agree to within 0.1 kcal/mol. Counterpoise corrections to the $n \geq 3$ n-body interactions are found to be very small. However, they are sizable for the two-body interaction energies, ranging from 5.9-6.9 kcal/mol with the aug-cc-pVDZ basis set and from 2.9-3.5 kcal/mol with the aug-cc-pVTZ basis set. Thus the relative insensitivity of the 2-body interaction energies (and, hence, the net binding energies) to the basis set is in part fortuitous, reflecting the opposing tendencies of the BSSE to decrease and the "true" binding energy to increase in magnitude with increasing basis set flexibilty.

The complete-basis-set limit MP2 level 2-body interaction energies are expected to fall close to the uncorrected aug-cc-pVTZ results. This was confirmed by carrying out MP2/aug-cc-pVQZ[98,99] calculations of the two-body interaction energies for **I**-**V**. In each case, the resulting interaction energy is found to agree to within 0.1 kcal/mol of the corresponding MP2/aug-cc-pVTZ result.

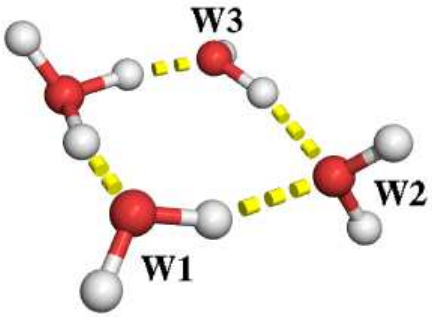

Figure 7: $H_3O^+(H_2O)_3$ MP2/aug-cc-pVDZ minimum **I'**

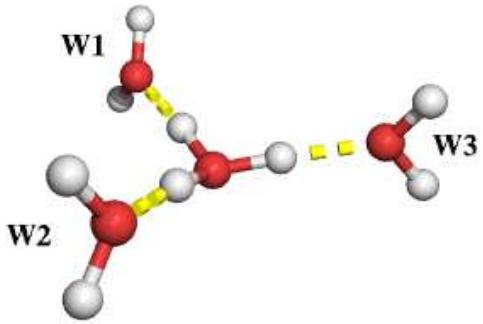

Figure 8: $H_3O^+(H_2O)_3$ MP2/aug-cc-pVDZ minimum **II'**

Table 3: MP2/aug-cc-pVTZ and MSEVB 2-body interaction energies (kcal/mol) for **I**, **II**, **IV** and **V**

2-body fragment[a]	**I**		**II**		**IV**		**V**	
	MP2[b]	MSEVB[c]	MP2[b]	MSEVB[c]	MP2[b]	MSEVB[c]	MP2[b]	MSEVB[c]
$H_3O^+, W1$	-31.34	-31.91	-30.64	-31.10	-7.46	-6.20	-37.00	-41.55
$H_3O^+, W2$	-30.53	-31.93	-34.76	-34.92	-36.66	-39.99	-9.08	-6.41
$H_3O^+, W3$	-10.12	-8.92	-30.63	-31.03	-35.88	-32.16	-7.61	-6.32
$H_3O^+, W4$	-30.42	-29.80	-7.24	-5.83	-7.80	-5.42	-32.78	-30.78
W1,W2	0.87	1.49	0.77	1.57	-3.92	-7.14	-3.73	-6.86
W1,W3	0.35	0.62	0.75	1.54	0.33	0.51	-0.36	-0.36
W1,W4	0.71	1.47	0.29	0.54	0.14	0.21	0.87	1.45
W2,W3	-4.24	-4.62	0.73	1.51	0.77	1.53	-4.23	-5.09
W2,W4	1.44	2.72	-4.08	-7.27	0.29	0.32	1.15	2.34
W3,W4	-4.28	-4.04	0.32	0.44	-4.00	-7.48	-4.62	-5.39
Sum of 2-body terms	-107.56	-104.92	-104.49	-104.55	-94.19	-95.82	-97.39	-98.97

[a] Numbering scheme for cluster fragments is depicted in Figures 1-5.
[b] MP2/aug-cc-pVTZ energies calculated at MP2/aug-cc-pVDZ geometries.
[c] MSEVB energies calculated at MSEVB geometries.

The trends discussed above for the $H_3O^+(H_2O)_4$ cluster are consistent with those reported previously by Pedulla *et al.*[101] for the neutral water clusters. In particular, in both cases, the $n \geq 3$ body interaction energies are relatively insensitive to the basis set, leading to the conclusion that the need for large basis sets to attain convergence in supermolecule calculations is due almost entirely to the 2-body (and 1-body) contributions to the interaction energies. This suggests that for protonated clusters (as for the neutral clusters) accurate formation energies can be obtained by combining MP2/aug-cc-pVTZ (or MP2/aug-cc-pVQZ) results for the 1- and 2-body interaction energies with MP2/aug-cc-pVDZ results for the higher-body interaction energies.

The net three-body interaction energies are calculated to range from 11.7 kcal/mol in **I** to -3.0 kcal/mol in **IV**. This is in contrast to the situation for the low energy structures of neutral water clusters, for which the net three-body terms are usually attractive.[101] The large variation in the three-body interaction energies in the $H_3O^+(H_2O)_4$ clusters is due to the fact that the H_3O^+ ion orientates the nearby H_2O monomers so that their dipoles are unfavorably aligned (with respect to the $H_2O \cdots H_2O$ interactions). When these water monomers are polarized by the H_3O^+ entity, their interactions with the other nearby water monomers become even less favorable. This is examined in more detail in Table 4 which lists the individual 3-body interaction energies of **I**, **II**, **IV**, and **V** calculated at the MP2/aug-cc-pVTZ level of theory. The table also lists results obtained using the MSEVB method, which will be considered later in the paper. The individual 3-body contributions range from -6.5 to 7.2 kcal/mol. The most favorable 3-body interactions occur for **W1**-**W2**-H_3O^+ and **W3**-**W4**-H_3O^+ in **IV** for which the H-bonding topology is ideally arranged. In contrast, in the **W2**-**W4**-H_3O^+ portion of **I**, the single-donor OH groups of **W2** and **W4** are unfavorably aligned, leading to a positive three-body interaction energy.

Table 4: MP2/aug-cc-pVTZ and MSEVB 3-body interaction energies (kcal/mol) for **I**, **II**, **IV** and **V**

3-body fragment[a]	**I**		**II**		**IV**		**V**	
	MP2[b]	MSEVB[c]	MP2[b]	MSEVB[c]	MP2[b]	MSEVB[c]	MP2[b]	MSEVB[c]
$H_3O^+, W1, W2$	4.26	3.52	4.96	3.57	-6.50	-4.62	-4.83	-5.52
$H_3O^+, W1, W3$	0.91	0.17	3.94	2.52	0.83	0.14	0.28	-0.04
$H_3O^+, W1, W4$	4.37	2.76	0.57	0.12	0.10	0.00	6.88	6.03
$H_3O^+, W2, W3$	-1.94	-1.88	4.90	3.55	7.15	5.36	-0.06	0.00
$H_3O^+, W2, W4$	5.21	3.62	-5.89	-2.88	0.79	0.28	1.36	0.34
$H_3O^+, W3, W4$	-1.96	-1.16	0.60	0.12	-5.94	-1.90	-3.80	-1.42
W1,W2,W3	0.10	0.00	-0.07	0.00	0.24	0.00	-0.94	0.00
W1,W2,W4	-0.09	0.00	0.15	0.00	0.11	0.00	0.22	0.00
W1,W3,W4	0.04	0.00	-0.02	0.00	0.07	0.00	0.19	0.00
W2,W3,W4	0.79	0.00	0.22	0.00	0.15	0.00	0.82	0.00
Sum of 3-body terms	11.69	7.03	9.36	7.00	-3.00	-0.74	0.12	-0.61

[a] Numbering scheme for cluster fragments is depicted in Figure 1-5.
[b] MP2/aug-cc-pVTZ energies calculated at MP2/aug-cc-pVDZ geometries.
[c] MSEVB energies calculated at MSEVB geometries.

The net 4-body interaction energies calculated using the MP2 method range from 0.08 kcal/mol in **II** to 1.19 kcal/mol in **V**, whereas the net 5-body interaction energies are predicted to be 0.1 kcal/mol or less. Thus, in order to obtain "chemical accuracy" of 1 kcal/mol in describing small protonated water clusters, it is essential to include interactions through fourth order.

We now examine the n-body contributions calculated at the Becke3LYP level of theory. The Becke3LYP calculations give net 2-body interaction energies smaller in magnitude by 0.3-2.1 kcal/mol and net 3-body interaction energies 0.1-1.2 kcal/mol less favorable than the MP2 values. The discrepancies between Becke3LYP and MP2 values for the 4- and 5-body interaction energies are less than 0.24 kcal/mol.

The net n-body interaction energies calculated using the MSEVB procedure differ appreciably from the MP2 values. The differences are as large as 2.6, 4.7, and 1.9 kcal/mol for the net 2-, 3-, and 4-body interactions, respectively. Particularly striking is the finding that the relaxation energies calculated in the MSEVB procedure are 2.8 - 5.5 kcal/mol greater than those calculated at the MP2 level. This is due primarily to the H_3O^+ entity rather than the H_2O monomers.

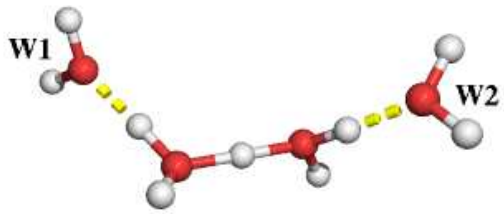

Figure 9: $H_3O^+(H_2O)_3$ MP2/aug-cc-pVDZ minimum **IV'**

Examination of the individual dimer fragment energies, tabulated in Table 3, reveals that individual $H_3O^+ \cdots H_2O$ interaction energies calculated with the MSEVB method differ by 1.2 to -4.6 kcal/mol from the corresponding MP2 values. Moreover, the MSEVB values of the water-water interaction energies differ from the MP2 values by 1.3 to -3.5 kcal/mol. Apparently the non-rigid TIP3P potential employed in the MSEVB procedure overestimates the attractive interaction between favorably aligned water monomers and is too repulsive for

some of the structures with unfavorably aligned dimers.

The trimer fragment interaction energies calculated using the MSEVB procedure differ by 4.0 to -1.8 kcal/mol from the corresponding MP2 values. Again, these differences can be traced in part to deficencies in the TIP3P model.

2.4.3 Infrared Spectra

The IR spectra of **I**, **II**, **IV** and **V** calculated in the harmonic approximation and using the Becke3LYP method are summarized in Figures 10-13. The IR spectrum of **III** is nearly identical to that of **II**, and, thus, is not reported. In discussing the IR spectra we focus on the OH stretch vibrations which are a particularly sensitive probe of the H-bonding environment.

The IR spectrum of **I** is characterized by an intense triplet of lines between 2747, 2854, and 3008 cm^{-1} due to the three OH stretch modes of the H_3O^+ entity and two less intense lines at 3604 and 3630 cm^{-1} associated with the two single-donor OH groups in the four-membered ring. In **II**, one of the intense transitions associated with the OH stretch modes of the H_3O^+ entity is located at 2358 cm^{-1} and the other two are located at 3032 cm^{-1} and 3081 cm^{-1}. The eigenvector associated with the 2358 cm^{-1} vibration is largely localized on the OH group which is H-bonded to the inner-shell **W2** water monomer bound to the second-shell **W4** monomer. The spectrum of **II** also shows an intense transition near 3347 cm^{-1} assocated with the single-donor OH stretch mode of the OH group of the **W2** molecule which is H-bonded to the outer-shell **W4** molecule.

The IR spectrum of **IV** is dominated by two intense lines 2017 and 2278 cm^{-1} associated with OH stretch modes of the H_3O^+ entity and another intense doublet at 3296 and 3313 cm^{-1} due to the single-donor OH groups involved in the H-bonds at the ends of the chain (i.e., **W3** to **W4** and **W2** to **W1**). The vibrations giving rise to the spectral peaks at 2017 and 2278 cm^{-1} are associated with the OH groups of H_3O^+ involved in H-bonds to adjacent H_2O monomers. These are strongly red shifted due to the cooperative effects along the H_3O^+-**W3**-**W4** and H_3O^+-**W2**-**W1** subunits. The OH stretch vibration associated with the free OH group of the H_3O^+ entity is very weak and is located at 3813 cm^{-1}.

For **V**, the two intense OH transitions at 1797 and 2651 cm^{-1} are due to vibrations asso-

ciated with the OH groups of H_3O^+ involved in the H-bonding network (the lower frequency mode is due to the OH group of H_3O^+ hydrogen bonded to **W1** and the higher frequency mode to the OH group hydrogen bonded to **W4**. The free OH group of the H_3O^+ entity has a frequency at 3797 cm^{-1}, but carries very little intensity. There are also fairly intense lines due to H_2O single-donor OH modes at 3210, 3545 and 3664 cm^{-1}. The intense peak at 1379 cm^{-1} arises from an asymmetric bend of H_3O^+ and **W1** and an incipient proton transfer occuring between the two molecules.

As noted in the previous section, inclusion of harmonic vibrational zero-point energies destabilizes the various $H_3O^+(H_2O)_4$ isomers by 7.0-9.0 kcal mol^{-1}, with isomer **I** being destabilized the most by this correction (see Table 6). When the vibrational zero-point corrections are added to the MP2-level formation energies, **I**, **II**, and **III** are predicted to be nearly isoenergetic. Clearly, vibrational anharmonicity could be important in determining the relative energies of the various $H_3O^+(H_2O)_4$ isomers.

Table 5: n-body contributions to the formation energies (kcal/mol) for minima **I**, **II**, **IV** and **V** calculated at the MP2, B3LYP and MSEVB levels of theory.

interaction	**I**			**II**		
	MP2[a]	B3LYP[b]	MSEVB[c]	MP2	B3LYP	MSEVB
1-body	2.89	2.37	8.35	3.36	2.63	6.19
2-body	-107.56	-106.66	-104.92	-104.49	-104.20	-104.55
3-body	11.69	12.78	7.03	9.36	10.59	7.00
4-body	0.43	0.38	-1.44	0.08	-0.11	-0.42
5-body	-0.05	-0.21	-0.l0	-0.03	-0.21	-0.29

interaction	**IV**			**V**		
	MP2	B3LYP	MSEVB	MP2	B3LYP	MSEVB
1-body	7.60	6.55	10.40	7.45	6.55	12.57
2-body	-94.19	-92.95	-95.82	-97.39	-95.26	-98.97
3-body	-3.00	-2.95	-0.74	0.12	0.27	-0.61
4-body	1.09	0.95	2.10	1.19	0.96	1.76
5-body	0.03	-0.14	0.10	0.03	0.16	-0.12

[a] MP2/aug-cc-pVTZ energies calculated using MP2/aug-cc-pVDZ geometries.
[b] B3LYP/aug-cc-pVDZ energies calculated using MP2/aug-cc-pVDZ geometries.
[c] MSEVB energies calculated using MSEVB geometries.

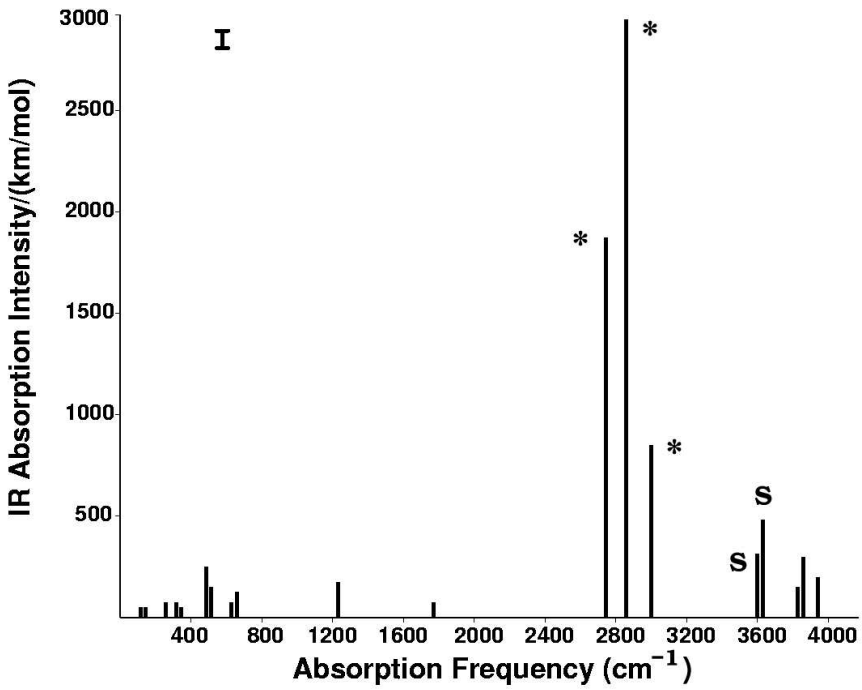

Figure 10: Calculated IR spectra of $H_3O^+(H_2O)_4$ minimum **I**

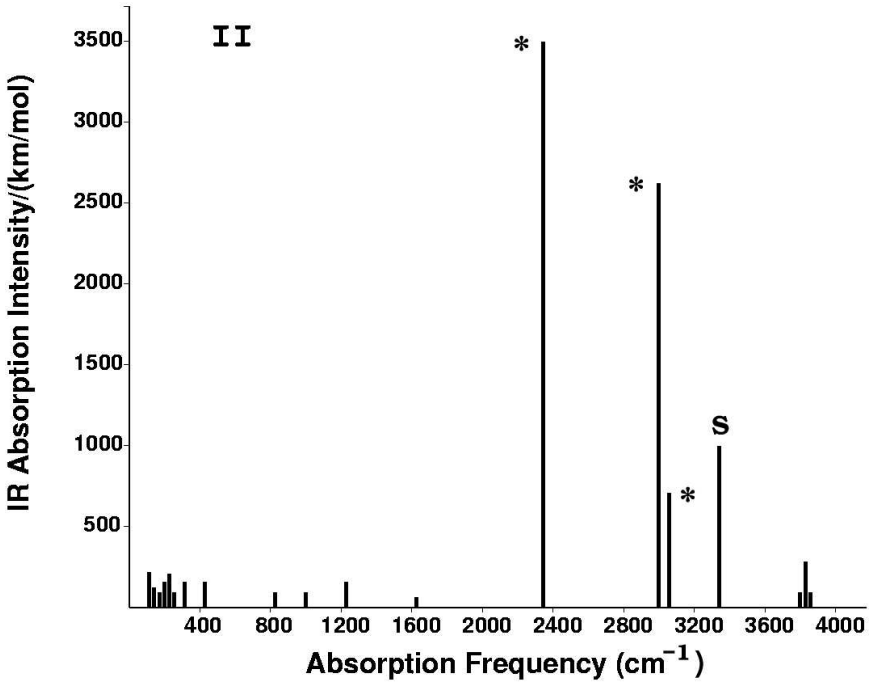

Figure 11: Calculated IR spectra of $H_3O^+(H_2O)_4$ minimum **II**

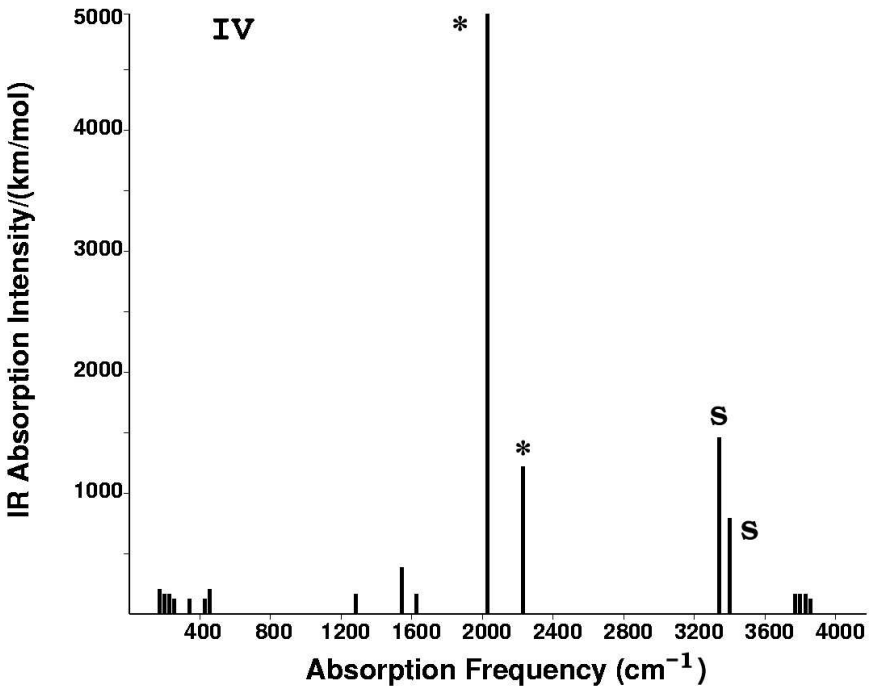

Figure 12: Calculated IR spectra of $H_3O^+(H_2O)_4$ minimum **IV**

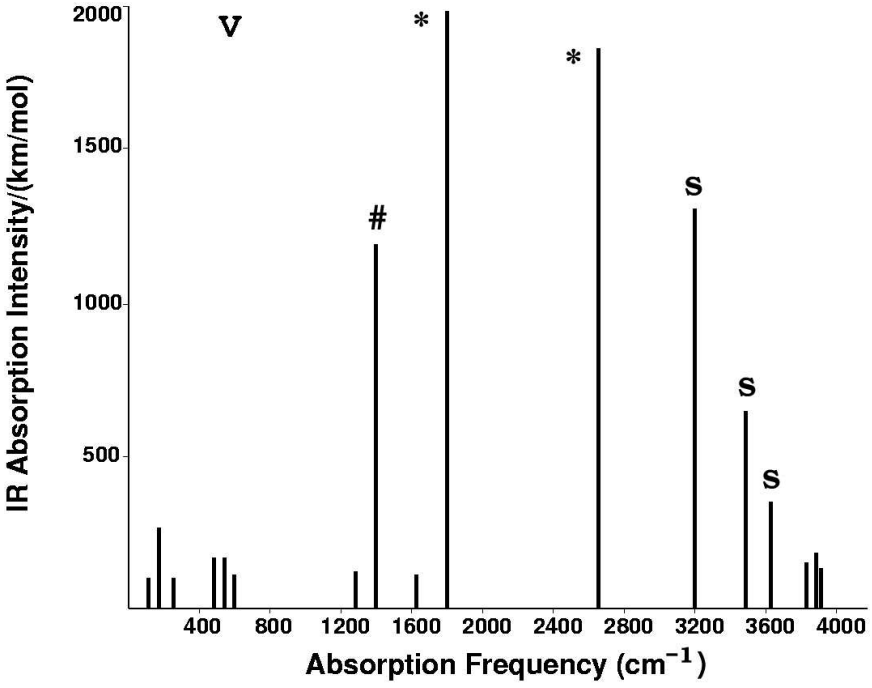

Figure 13: Calculated IR spectra of $H_3O^+(H_2O)_4$ minimum **V**

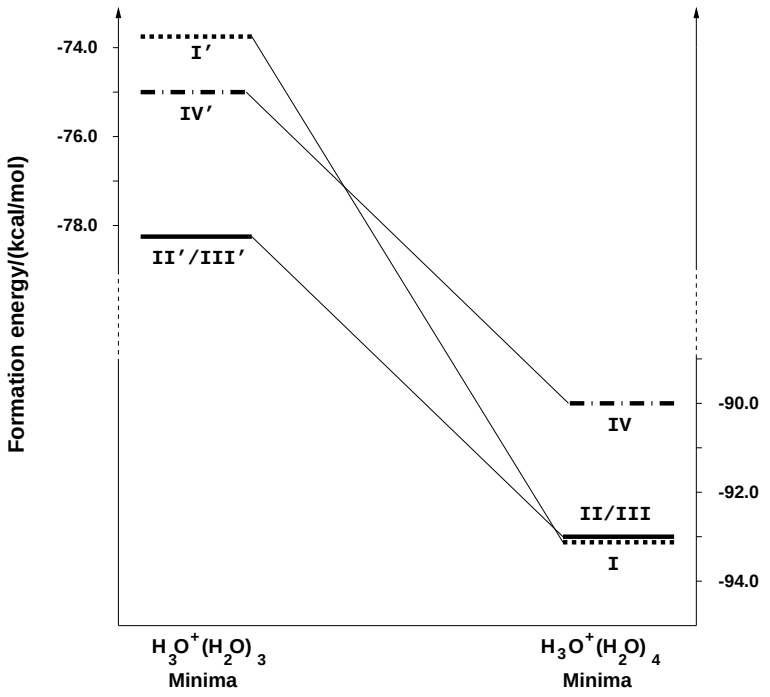

Figure 14: Comparison of the relative energies of the $H_3O^+(H_2O)_4$ and related $H_3O^+(H_2O)_3$ clusters calculated at the MP2/aug-cc-pVDZ level of theory

Table 6: Effect of ZPE upon MP2/aug-cc-pVDZ formation energies (kcal/mol) of $H_3O^+(H_2O)_4$ isomers.

Isomer	Formation energy	
	without ZPE[a]	with ZPE[b]
I	-92.60	-83.62
II	-91.72	-84.16
III	-91.74	-83.97
IV	-88.47	-81.50
V	-88.60	-80.32

[a] From MP2 calculations using the aug-cc-pVTZ basis set.

[b] The vibrational zero-point-energy (ZPE) corrected formation energies were obtained by combining the MP2/aug-cc-pVTZ results with vibrational corrections calculated at the Becke3LYP/aug-cc-pVDZ level of theory and employing the harmonic approximation.

Figure 16-17 reports the IR spectra of **I'**, **II'**, and **IV'** calculated in the harmonic approximation and using the Becke3LYP method. Comparison of the calculated spectra of **I** and **I'** and of **II** and **II'**, show that the expected trends upon adding an extra solvent molecule in going from $H_3O^+(H_2O)_3$ to $H_3O^+(H_2O)_4$. However, the degree of disimiliarity between the spectra of **IV** and **IV'** suggests a fundamental difference between the hydrogen bonding topologies in the two structures. Indeed, examination of the geometrical structures reveals that the proton bearing entity in **IV'** is $H_5O_2^+$ rather than H_3O^+ as in **IV** (see Figure 9). In the spectra of **IV'**, the two intense peaks at 3008 and 3061 cm^{-1} are due to OH stretch vibrations associated with the OH groups of the $H_5O_2^+$ entity H-bonded to the two H_2O molecules. The peak at 1729 cm^{-1} arises from an asymmetric bending of the H_2O molecules in $H_5O_2^+$, and the two peaks at 837 cm^{-1} and 1013 cm^{-1} correspond to wagging motion of the two hydrogen atoms in $H_5O_2^+$ H-bonded to the **W1** and **W2** molecules. All three of these vibrations involve significant motion of the central proton in the $H_5O_2^+$ entity.

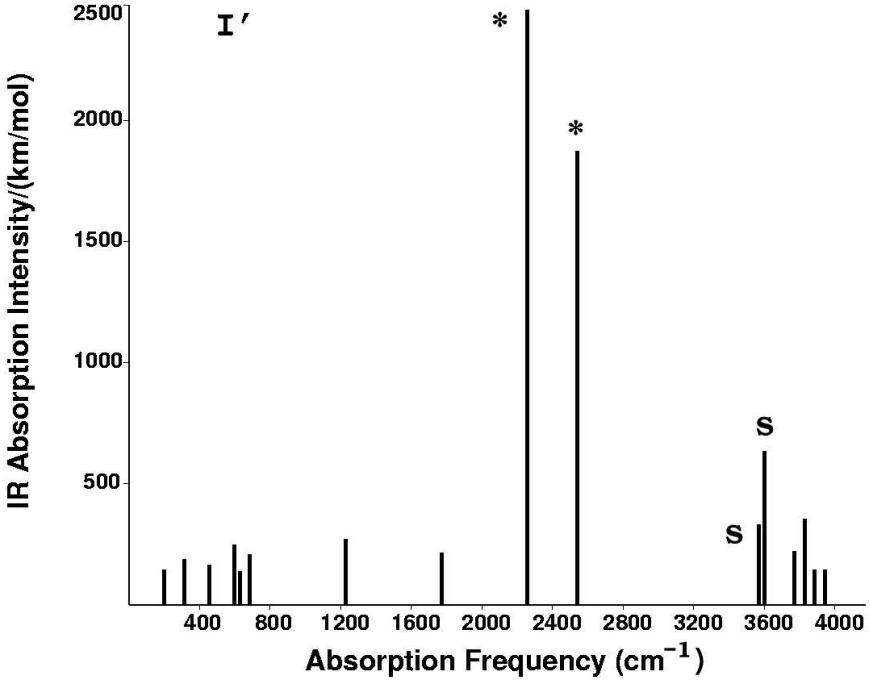

Figure 15: Calculated IR spectra for $H_3O^+(H_2O)_3$ minimum **I'**

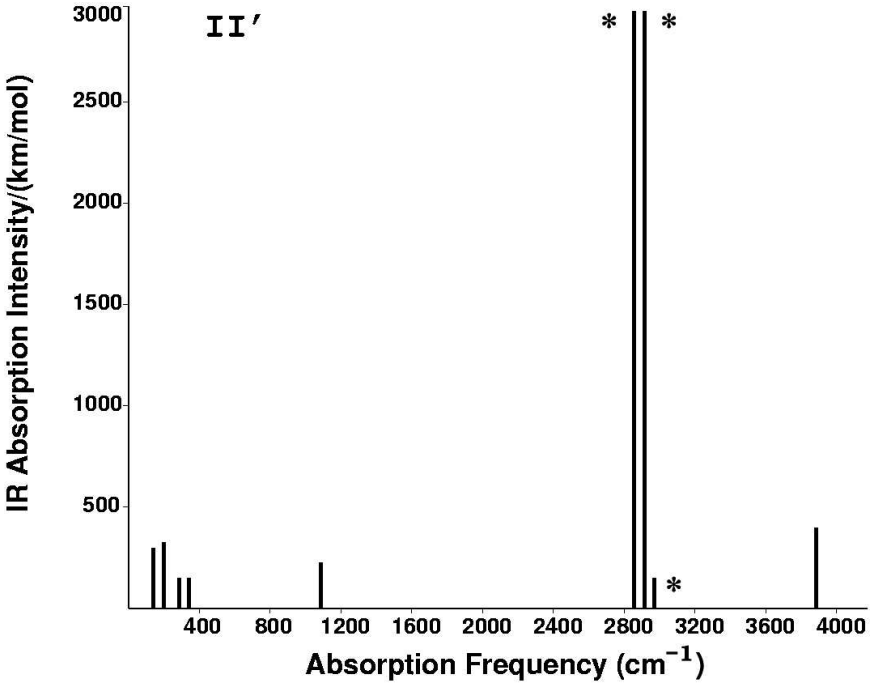

Figure 16: Calculated IR spectra for $H_3O^+(H_2O)_3$ minimum **II'**

2.5 CONCLUSIONS

MP2 level calculations, without inclusion of vibrational zero-point corrections, predict species **I** to be the most stable form of $H_3O^+(H_2O)_4$, with the next most stable isomer lying about 1.2 kcal/mol higher in energy. With the inclusion of vibrational zero-point corrections, the three lowest energy forms of the cation, **I**, **II** and **III**, are predicted to be almost isoenergetic. Density functional calculations using the Becke3LYP and BP functionals introduce a bias of about 1.1 kcal/mol in favor of structures that lack double-acceptor water monomers compared to those that contain such species. The model potential of Hodges and Stone[78] reproduces the relative energies of the various $H_3O^+(H_2O)_4$ isomers as predicted by the MP2 calculations with a reasonable degree of accuracy. On the other hand, the relative energies calculated using the MSEVB procedure differ by up to 4.5 kcal/mol from the MP2 results. Analysis of the individual 2- and 3-body contributions to the interaction energies reveal that a significant part of the errors in the MSEVB energies can be traced to the use of the

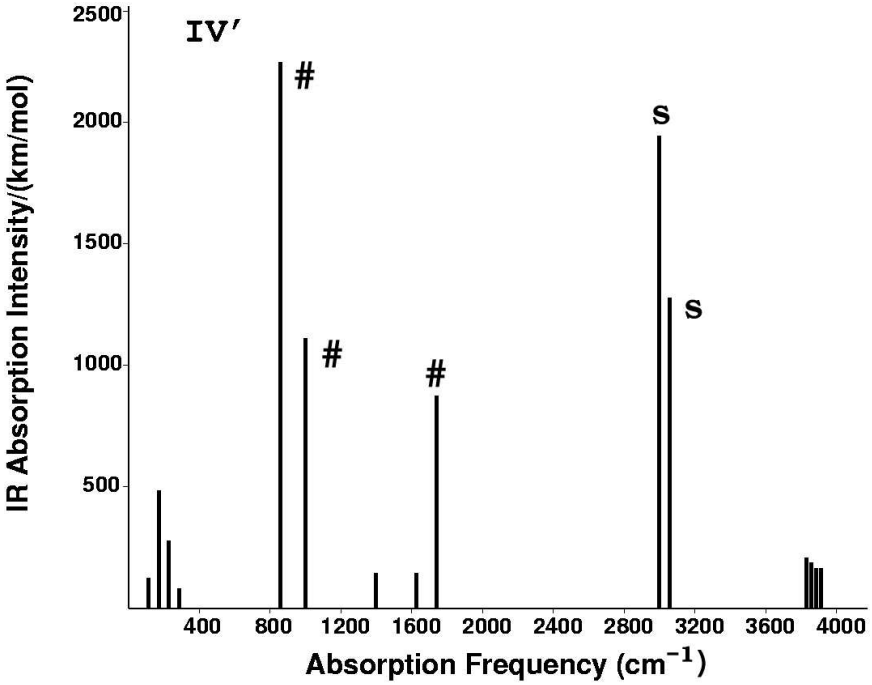

Figure 17: Calculated IR spectra for $H_3O^+(H_2O)_3$ minimum **V'**

TIP3P model to describe the water-water interactions. This suggests that the reliability of this approach could be greatly improved by the adoption of more realistic water-water potentials.

The calculated IR spectra differ appreciably from isomer to isomer, with the OH stretch vibrations of the H_3O^+ species proving to be especially sensitive to the environment of the ion. Comparison of the IR spectra of the $H_3O^+(H_2O)_3$ and $H_3O^+(H_2O)_4$ clusters reveals that for two of the isomers (**I'** $\rightarrow$ **I** and **II'** $\rightarrow$ **II**) the introduction of a water monomer in the second solvation shell leads to a large red shift and intensity increase of the OH stretch vibration associated with the OH group of H_3O^+ directly involved in the "extended" H-bonding network. On the other hand, the chain-like forms of $H_3O^+(H_2O)_3$ and $H_3O^+(H_2O)_4$ are found to be fundamentally different, with the proton being associated with a $H_5O_2^+$ entity in the former and with a H_3O^+ entity in the latter.

2.6 ACKNOWLEDGMENTS

We thank Udo Schmitt for helpful discussions about the MSEVB method. The calculations were carried out on the IBM 43P 260 computers in the University of Pittsburgh's Center for Molecular and Materials Simulations. These computers were funded by grants from NSF and IBM.

3.0 FINITE TEMPERATURE BEHAVIOR OF $H^+(H_2O)_6$ AND $H^+(H_2O)_8$

This work was published as

Christie, R. A.; Jordan, K. D. *J. Phys. Chem. B* **2002**, *106*, 8376

3.1 ABSTRACT

The finite temperature behavior of $H^+(H_2O)_6$ and $H^+(H_2O)_8$ is investigated by means of parallel tempering Monte Carlo simulations in conjunction with the multistate empirical valence-bond method for describing the interactions. The temperature dependence of the constant volume configurational heat capacity, $C_V(T)$, of $H^+(H_2O)_8$ reveals two sharp transitions, whereas that of $H^+(H_2O)_6$ is devoid of sharp structure.

3.2 INTRODUCTION

In recent years considerable progress has been made in the characterization of neutral and charged water clusters. Recent experimental studies have revealed that "hot" clusters can have markedly different properties than "cold" clusters due to the much wider range of configurations explored in the former.[103,104,105,106] However, to date, there have been very few experiments on water cluster systems providing information on the properties as a function of temperature. Computer simulations are especially valuable for filling this void. Most noteworthy are simulations showing that some of the neutral clusters, e.g., $(H_2O)_8$, undergo

relatively sharp melting transitions.[101,107,108,109,110,111,112,113] Far less is known about the finite temperature properties of $(H_2O)_n^+$, $H^+(H_2O)_n$, and $(H_2O)_n^-$ clusters.

In this study the parallel tempering canonical Monte Carlo simulation method[114] is used to characterize the $H^+(H_2O)_6$ and $H^+(H_2O)_8$ clusters as a function of temperature. These two clusters are chosen for investigation due to the contrasting thermal behavior of the corresponding neutral clusters, $(H_2O)_6$ and $(H_2O)_8$. Whereas numerous research groups have concluded that $(H_2O)_8$ undergoes a pronounced solid-like to liquid-like transition,[101,107,109,110,111,112,113,115] there are conflicting reports concerning $(H_2O)_6$, with the most recent studies indicating that the small peak in the calculated heat capacity of this system should not be viewed as indicative of "melting".[101,113] Since the introduction of the proton drastically alters the potential energy surface of small water clusters, large changes are expected in the thermodynamic properties as well in going from the neutral to the protonated clusters.

The nature of the solvated proton, both in small water clusters and in bulk liquid water has long been the subject of considerable speculation. Both the Eigen[28] $H_9O_4^+$ and Zundel[31] $H_5O_2^+$ species have been proposed as the fundamental "carrier" of the proton, and $H_5O_2^+$ is a key species in the Grotthuss mechanism[26] of proton mobility in bulk water. Ab initio simulations[84] with classical nuclear dynamics predict that a proton in bulk water at 300 K spends about 60% of the time as $H_9O_4^+$ and 40% as $H_5O_2^+$. Simulations with quantum mechanical treatment of the nuclear motion (through a path integral method) yield a qualitatively similar picture, with both $H_5O_2^+$ and $H_9O_4^+$ proton-bearing entities found to be important.[116]

Recently, Jiang *et al.*[48] have determined OH stretch spectra for $H^+(H_2O)_n$, n=5-8, at a temperature of 170 $\pm$20 K. Comparison of the measured and calculated IR spectra enabled these researchers to assign the structures responsible for the observed spectra. This study provided direct experimental evidence of the Zundel-type $H_5O_2^+$ species.

In recent years, several simulations have been carried out with the aim of understanding the structural and thermal properties of protonated water clusters. These include canonical Monte Carlo simulations of $H^+(H_2O)_n$ (n=9, 21, 40) by Svanberg and Pettersson[117] and grand canonical Monte Carlo simulations of various sized protonated water clusters by

Shevkunov and Vegiri[80] and by Kusaka and Oxtoby.[118] Singer et al.[66] studied the thermal and structural properties of $H^+(H_2O)_8$ and $H^+(H_2O)_{16}$ by means of J-walking[119] canonical Monte Carlo simulations. However, none of these studies can be viewed as definitive, either because the model potentials employed restricted the proton to a specific H_3O^+ entity, or because the simulations were not run long enough to ensure equilibrium.

The calculations reported in the present study are timely in that they will provide, for $H^+(H_2O)_6$ and $H^+(H_2O)_8$, information on the relative importance of $H_9O_4{}^+$ and $H_5O_2{}^+$ proton bearing entities as a function of temperature and will examine whether these clusters undergo melting-type behavior.

3.3 METHODOLOGY

Simulations of the $(H_2O)_n$, $n \geq 8$ clusters have been found to be prone to quasi-ergodic behavior due to the existence of large potential energy barriers separating low energy local minima.[115,120] Quasi-ergodic behavior is also expected to be a problem in simulations of $H^+(H_2O)_n$ clusters. To overcome this problem, the parallel tempering Monte Carlo simulation method[114] is employed. In this approach, Monte Carlo simulations are carried out in parallel for a grid of temperatures, with the highest temperature (T_1) being chosen so that the barriers in the potential energy surface are readily overcome. Most of the attempted moves are carried out using the Metropolis algorithm,[121] with the remainder involving jumps between configurations generated at different temperatures. The acceptance probability of the jump moves is given by

$$\mathrm{acc}(\vec{r}_n \rightarrow \vec{r}_{n'}) = \min\{1, \exp[-(\beta_n - \beta_{n'})(U(\vec{r}_{n'}) - U(\vec{r}_n))]\}, \tag{3.1}$$

where $\vec{r}_n$ and $\vec{r}_{n'}$ denote the two configurations from the simulations at temperatures T_n and $T_{n'}$, respectively, and β_n and $\beta_{n'}$ represent the inverse temperatures. The energies of the configurations $U(\vec{r}_n)$ are calculated using the multi-state empirical valence-bond (MSEVB) method of Schmitt and Voth.[74] The MSEVB potential is based upon a flexible, reparameterized TIP3P[122] model to represent the $H_2O \cdots H_2O$ interactions, and an effective valence-bond

treatment of the $H_3O^+ \cdots H_2O$ interactions. The diagonal elements in the MSEVB Hamiltonian give the energies of the various valence-bond configurations with the excess proton associated with specific water molecules, and the off-diagonal matrix elements give the couplings between the valence-bond configurations. With the MSEVB model the excess proton can be localized in either Eigen or Zundel structures and proton transfer can occur between water molecules during the course of the simulation.

In this work, the parallel tempering simulations employed 32 temperatures ranging from 5 to 240 K for $H^+(H_2O)_6$ and from 10 to 395 K for $H^+(H_2O)_8$. The simulation temperatures were determined "trial by error", with the highest temperature being chosen so that the barriers are readily surmounted, and the intermediate temperatures being chosen so that there is significant overlap between the potential energy distributions generated at adjacent temperatures. For $H^+(H_2O)_6$ this led to 2-3 K temperature intervals for the simulations carried out at low temperatures (T$\leq$20 K), 5 K intervals for T=20-70 K, 10 K intervals for T=70-220 K, and a final temperature of 240 K. For $H^+(H_2O)_8$, a 5 K temperature interval was used for T=20-70 K, a 10 K temperature interval for T=70-170 K, a 20 K interval for T=170-270 K, and a 25 K interval for T=270-370 K. In this case, simulation temperatures of 10, 20 and 395 K were also included. Exchanges were attempted only between configurations sampled at adjacent temperatures, with one attempted exchange being made every 10th Monte Carlo cycle. A constraining sphere of 12 Å was used to prevent evaporative events.

Each Monte Carlo cycle consisted of an attempted rotation and translation of each molecule (both H_3O^+ and the solvating water molecules). Every fifth Monte Carlo cycle, translations of every atom in the cluster were attempted in addition to the rigid molecule moves. The step sizes were adjusted to keep the acceptance rates near 45%. The identification of the H_3O^+ entity was accomplished by analysis of the MSEVB wavefunction. Of course, Zundel-like structures have two valence-bond configurations of nearly equal weight, and this approach singles out the one with the slightly larger weight in the wavefunction for rotation and translation of a H_3O^+ entity. In principle, both dominant valence-bond structures should be used in generating the moves in such cases. However, the approach used should not introduce a bias into the simulations as the atom moves should compensate for the deficiencies of this partitioning scheme.

For each sized cluster the parallel tempering simulations were carried out starting from two different initial configurations selected at random from configurations sampled in preliminary Metropolis Monte Carlo simulations carried out at elevated temperatures. The thermodynamic properties are found to be independent of the choice of initial configuration, thereby establishing that convergence has been achieved.

The simulations of $H^+(H_2O)_6$ employed 1×10^7 cycles for equilibriation, followed by 2×10^7 cycles to collect ensemble averages, whereas those of $H^+(H_2O)_8$ employed 4×10^7 cycles for equilibriation, followed by 4×10^7 production cycles. As noted above, each cycle consists of multiple attempted moves. These simulations employ far more Monte Carlo steps than previous simulations of protonated water clusters. At each temperature in the parallel tempering simulations, 10^4 configurations (one every 2000 cycles for $H^+(H_2O)_6$ and one every 4000 cycles for $H^+(H_2O)_8$) were saved for subsequent analysis. The saved configurations were optimized to their inherent structures using the steepest descent method. The various local minima were distinguished and characterized according to their hydrogen bonding topologies.

To help elucidate possible "melting" behavior of the $H^+(H_2O)_6$ and $H^+(H_2O)_8$ clusters, the dimensionless configurational constant volume heat capacity, C_V/k_B

$$\frac{C_V}{k_B} = \frac{1}{(k_BT)^2}(\langle U(\vec{r})^2\rangle - \langle U(\vec{r})\rangle^2), \tag{3.2}$$

was calculated.

3.4 RESULTS AND DISCUSSION

3.4.1 $H^+(H_2O)_6$: Low-energy minima

Figure 18 depicts the structures and reports the energies of the low-energy isomers of $H^+(H_2O)_6$ determined by optimizing configurations sampled in the parallel tempering Monte Carlo simulations. The various isomers are labeled as Zundel, Eigen, or Zundel-Eigen depending on the nature of the MSEVB wavefunction. In those cases that the MSEVB

wavefunction is dominated by two valence-bond configurations of nearly equal weight (*i.e.*, to within 4%) and which together account for over 85% of the total contributions to ψ^2_{MSEVB}, the structure is designated as Zundel. In those cases that a single valence-bond configuration contributes over 60% to ψ^2_{MSEVB}, the structure is labeled as Eigen. All other structures are listed as Zundel-Eigen, indicating that there is both significant Zundel and Eigen-like character.

The lowest energy structure located by the optimizations (minimum **I**) can be viewed as an $H_5O_2^+$ entity hydrogen bonded to four water molecules, one to each of the "free" H atoms of $H_5O_2^+$. Evidence for such a species was provided by the recent IR measurements of Jiang *et al.*[48] The calculations also give two minima, designated **II** and **IV**, which differ from **I** only in the orientation of the "solvent" H_2O molecules. These are calculated to lie only 0.21 (**II**) and 0.44 kcal/mol (**IV**) above **I** in energy. There is also a fourth low-lying Zundel-like structure, labeled **III**, which lies only 0.26 kcal/mol above **I**, and which has a four-remembered ring (where the ring size is established by the number of oxygen atoms). The optimizations also located several other energetically higher-lying species with ring-based or branched Eigen-like structures.

Jiang *et al.*[48] carried out MP2/6-31+G* calculations on a select group of $H^+(H_2O)_6$ isomers and reported a structure similar to **I** as the lowest energy minimum. The lowest energy minimum predicted in various DFT studies include a branched-type[85] structure, a structure which appears similar to **I**,[48] and a fused-ring[78] structure. The lack of agreement between the various DFT studies is likely due to differences in the basis sets and in the functionals employed. $H^+(H_2O)_6$ has also been studied[78,80,123] using the ASP,[124] Kozack-Jordan,[69] and Shevkunov-Vegiri[79] model potentials. However, each of these potentials constrains the proton to be associated with a specific H_3O^+ entity and thus does not permit proton mobility or the formation of $H_5O_2^+$ type species.

3.4.2 $H^+(H_2O)_6$: Thermal behavior

The calculated constant volume configurational heat capacity curve for $H^+(H_2O)_6$, shown in Figure 19, is relatively structureless over the 10-240 K temperature range exam-

ined, displaying only very weak maxima near T=20 and 100 K. The populations of various inherent structures sampled over the range of simulation temperatures are shown in Figure 20. In this plot the populations of the closely related structures, **I**, **II** and **IV** are plotted individually and grouped together. The population of the the various chain structures, of which **VI**, **IX** are the most stable, are reported as a group. The ring-based structures (**III**, **V**, **VII** and **VIII**) do not attain a significant population over the range of temperatures explored, and their populations are not reported.

At low temperatures, only minima **I**, **II** and **IV** are significantly populated. The net population of these species stays near 100% up to a temperature of about 30 K, after which it falls off gradually with increasing temperature, still being around 38% at T=200 K. As the net population of **I**, **II** and **IV** falls off, that of the branched minima gradually increases. From Figure 20, it is also seen that the slow fall off in the population of the (**I**, **II**, **IV**) group with increasing temperature, is in part a consequence of the fact that **II** and **IV** grow in importance up to temperatures of about 70 K and 80 K, respectively, largely compensating for the fall off in population of **I**. Near T=30 K, where the branched structures first acquire significant population, **VI**, which is the most energetically stable branched species, is far more important that **IX**. However, at high temperatures (e.g. T $\approx$ 210 K), these two species are about equally populated.

Neither the heat capacity curve, nor the variation in the populations of the inherent structures with temperature, provide evidence for a "solid" to liquid like transition for $H^+(H_2O)_6$.

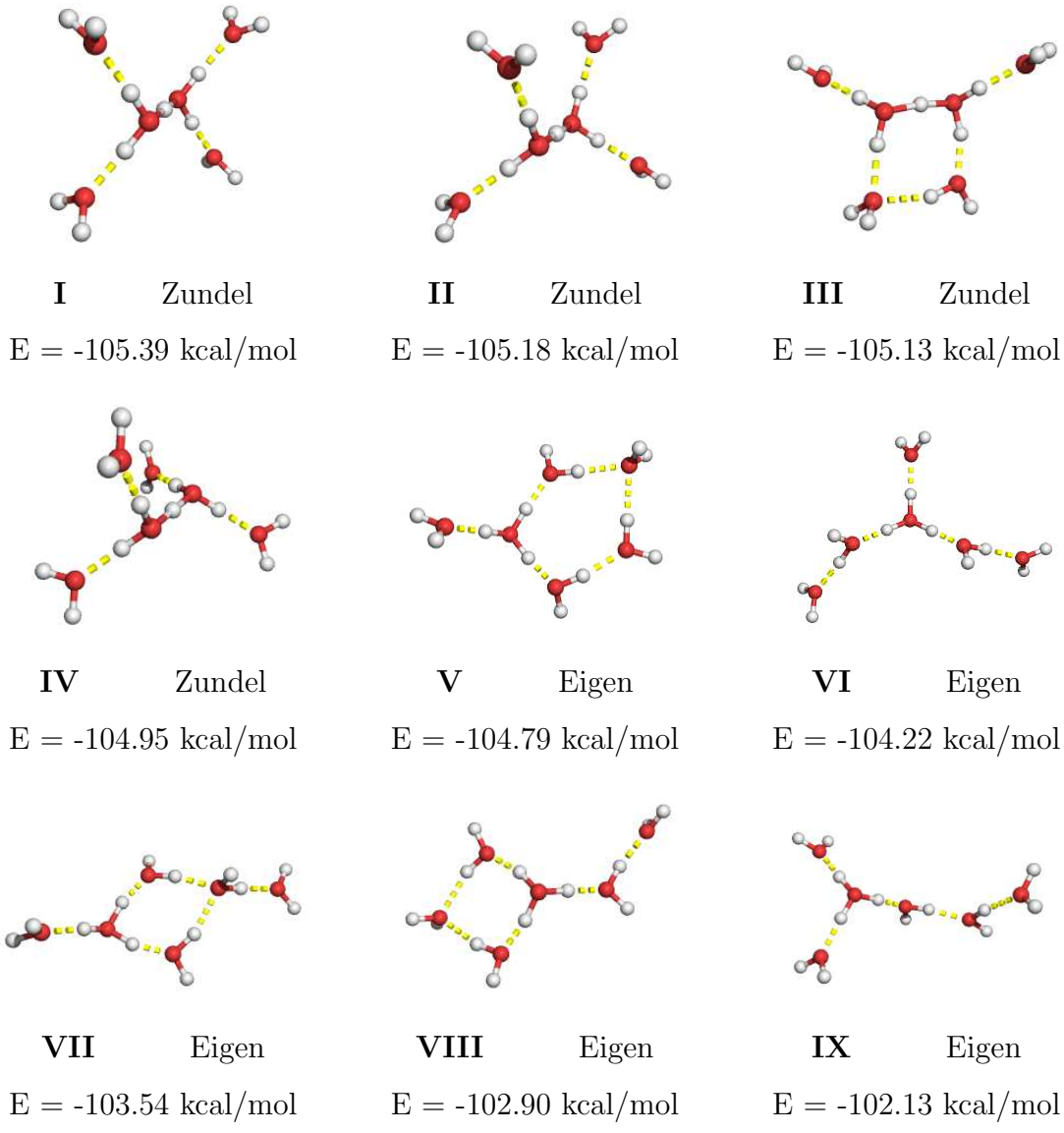

Figure 18: The nine most populated potential energy minima of $H^+(H_2O)_6$, together with their binding energies, recovered from parallel tempering Monte Carlo simulation trajectories. These are obtained by optimizing structures sampled at each of the 32 simulation temperatures. The structures are classified as Zundel-type $H_5O_2^+$, Eigen-type H_3O^+ or intermediate Zundel-Eigen depending on the weights of the various valence-bond configurations in the MSEVB wavefunction.

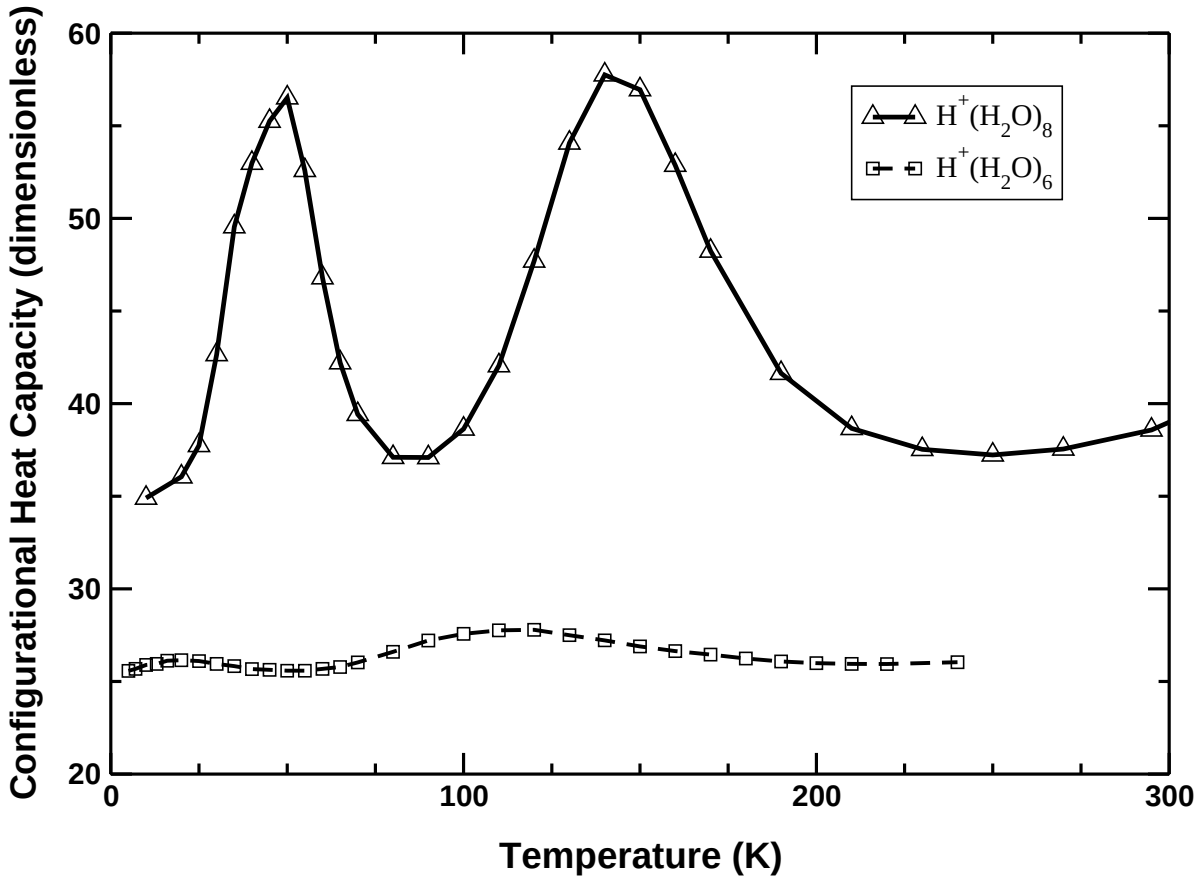

Figure 19: Temperature dependence of the constant volume configurational heat capacity, $C_V(T)$, for $H^+(H_2O)_6$ and $H^+(H_2O)_8$ from parallel tempering Monte Carlo simulations.

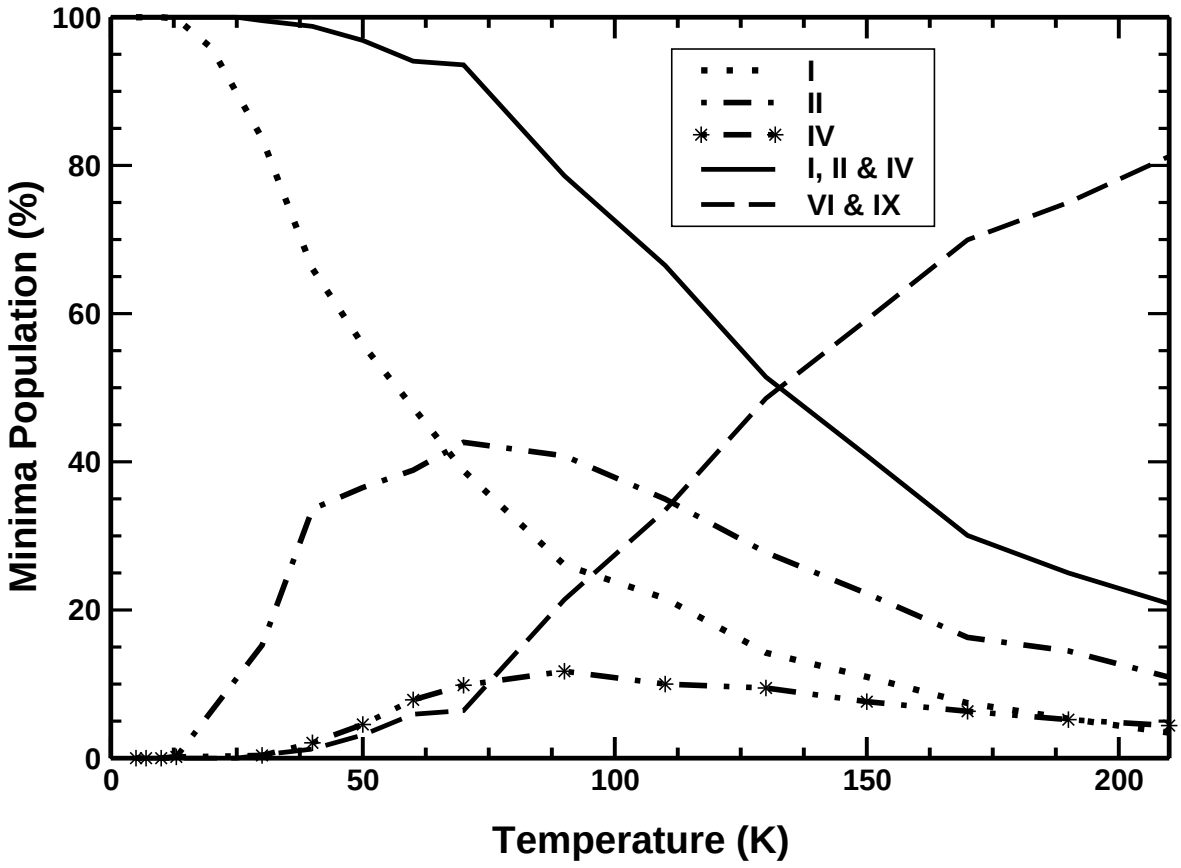

Figure 20: Temperature dependence of the population of various inherent structures of $H^+(H_2O)_6$ obtained by optimizing sampled configurations. Two distinct classes of hydrogen bonding topology are considered, the Zundel-based minima **I**, **II** and **IV**, and the Eigen-based branched minima, **VI** and **IX**.

3.4.3 $H^+(H_2O)_8$: Low-energy minima

Figures 21-24 depict low energy isomers of $H^+(H_2O)_8$ determined by optimizing configurations sampled in the parallel tempering Monte Carlo simulations. The figure also reports the energies and classifies the minima using the same scheme as for $H^+(H_2O)_6$.

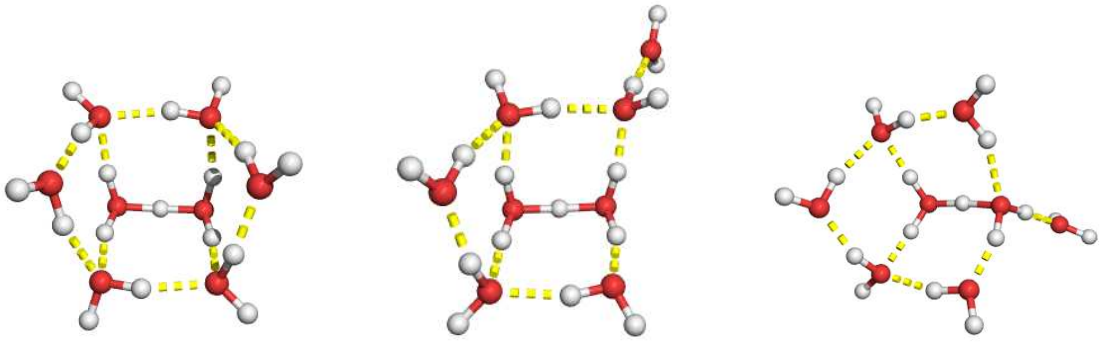

A Zundel E = -132.34 kcal/mol

B Zundel E = -131.21 kcal/mol

C Zundel-Eigen E = -130.94 kcal/mol

Figure 21: "Cubic"-like, low-energy minima of $H^+(H_2O)_8$ together with their MSEVB binding energies. (These are obtained by optimizing structures sampled at each of the 32 simulation temperatures.)

The three lowest energy structures of $H^+(H_2O)_8$ found in the optimizations can be viewed as being derived from "cubic"-type clusters. The most stable of these, structure **A**, has the proton localized in a $H_5O_2^+$ entity, and differs from an "ideal" cubic topology in that the hydrogen bond diagonally opposite the $H_5O_2^+$ is broken. The other two "cubic"-derived structures, **B** and **C**, lie about 1 kcal/mol higher in energy and have a second "broken" hydrogen bond (compared to the ideal cubic structure), reducing the number of fused rings to three. **B** has a Zundel-like structure, while **C** is classified as Zundel-Eigen.

At higher energies there are numerous other local minima, including species with two fused rings (**D**-**H**), a single ring (**J**-**M**), as well as branched structures (**N**-**R**). The two-fused ring isomers have Zundel or Zundel-Eigen structures, and most of the branched species are Eigen-like in nature.

MP2 calculations carried out by Ciobanu *et al.*[65] also give "cubic"-like structures as the lowest energy forms of $H^+(H_2O)_8$. However, the global minimum reported by these authors,

unlike our species **A**, retains the hydrogen bond diagonally opposite the $H_5O_2^+$ entity. The different DFT studies do not agree on the nature of the global minimum:[48,78,125] while Hodges and Stone[78] found a "cubic"-like structure similar to that reported by Ciobanu *et al.*[65] as the lowest-lying minimum, Wei and Salahub[85] predicted a branched form to be the lowest lying structure, and Jiang et al.[48] found a structure similar to **J** to be lowest in energy. $H^+(H_2O)_8$ has also been studied by Hodges and Stone[78] using the ASP[124] model potential, Hodges and Wales[123] using the Kozack-Jordan[69] potential, Shevkunov and Vegiri[80] using a potential developed by one of the authors (Shevkunov[79]), and by both Ciobanu *et al.*[65] and McDonald *et al.*[126] using the flexible OSS2[64] model potential, which allows the proton to be involved in both Zundel and Eigen-type structures. The different model potentials differ in terms of the global minimum structure identified.

3.4.4 $H^+(H_2O)_8$: Thermal behavior

The calculated configurational heat capacity of $H^+(H_2O)_8$ displays pronounced peaks near 50 K and 145 K, with the low-temperature peak being appreciably narrower than the high temperature peak (see Figure 19). In the vicinity of each of these two peaks, the heat capacity undergoes a change of about 22.5 C_V/k_B.

Jump-walking[119] Monte Carlo simulations carried out by Singer *et al.*[66] with the OSS2 model potential,[64] produced a heat capacity plot with a single peak at T=165 K, with a maximum of about 18 C_V/k_B. However, these simulations were carried out for far fewer moves than those presented here, and, as a result, did not achieve equilibrium (as is clear from the discussion in Singer[66]). Inconsistencies between the the heat capacity plots presented in Singer[66] and in this study may also be due to the different model potentials employed in the respective studies.

The populations of various isomers produced in the optimizations as a function of the temperature of the simulation are reported in Figure 25. In this plot, structures have been grouped together into four classes: the "cubic"-like structures **A**-**C,** the fused-ring structures **D**-**H**, the single-ring structures **I**-**M**, and the branched-chain structures **N**-**R**. The energies of the various isomers, to a good approximation, correlate with the number of rings, going up as

the number of rings decreases. As seen from Figure 25, for T≤25 K, only the cubic structures (**A**-**C**) have sizable population. As T is increased above about 25 K, the population of the cubic structures falls rapidly, being negligible for T>70 K. The two-fused ring species (**D**-**H**) first become important near T=25 K, with the population having a maximum near T=42 K and then falling off rapidly at still higher temperatures.

The third class of structures, those with a single ring (**I**-**M**), start to acquire sizable population near T=35 K and are the most important species between 58-175 K. They still have a sizable population (≈4%) at the highest temperature (395 K) considered. Branched isomers do not acquire significant population until T=110 K; for temperatures above T≈160 K, they are the most populated structures sampled in the simulations.

Comparison of these results with the structure in the heat capacity plot indicates that the peak near 50 K is due primarily to a transition between the "cubic"-like structures (**A**-**C**), and both the two-ring (**D**-**H**) and single-ring (**I**-**M**) structures. The higher temperature (T≈145 K) peak arises from transitions between single-ring (**I**-**M**) and branched-chain structures (**N**-**R**).

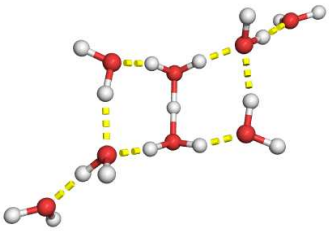

D Zundel

E = -130.69 kcal/mol

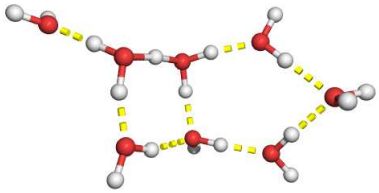

E Zundel

E = -130.64 kcal/mol

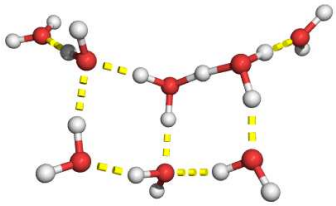

F Zundel

E = -130.63 kcal/mol

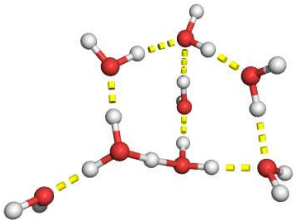

G Zundel-Eigen

E = -130.20 kcal/mol

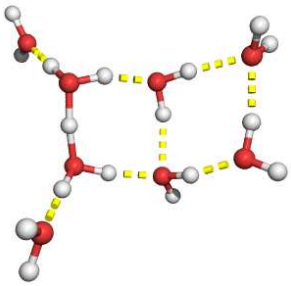

H Zundel

E = -129.95 kcal/mol

Figure 22: Five fused-ring minima of $H^+(H_2O)_8$, together with their binding energies, recovered from parallel tempering Monte Carlo simulation trajectories. (These are obtained by optimizing structures sampled at each of the 32 simulation temperatures.)

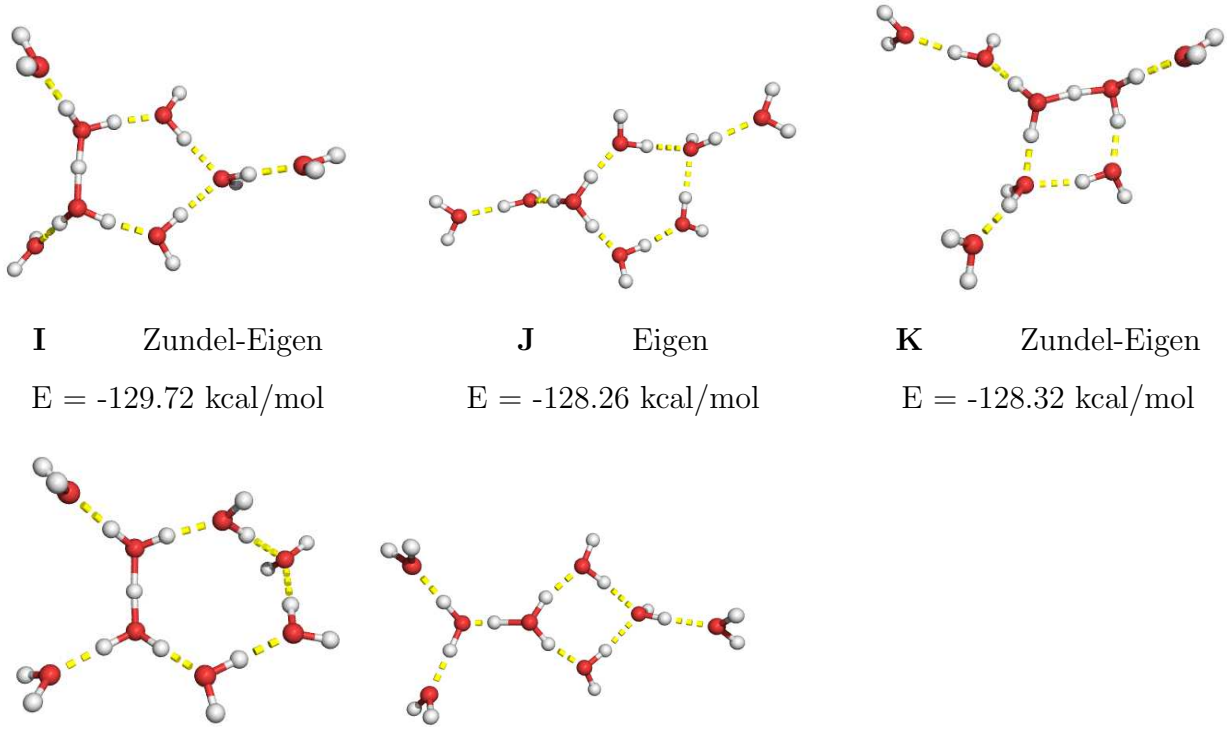

I Zundel-Eigen
E = -129.72 kcal/mol

J Eigen
E = -128.26 kcal/mol

K Zundel-Eigen
E = -128.32 kcal/mol

L Zundel-Eigen
E = -127.63 kcal/mol

M Zundel-Eigen
E = -126.80 kcal/mol

Figure 23: Five single-ring minima of $H^+(H_2O)_8$ together with their binding energies, recovered from parallel tempering Monte Carlo simulation trajectories. (These are obtained by optimizing structures sampled at each of the 32 simulation temperatures.)

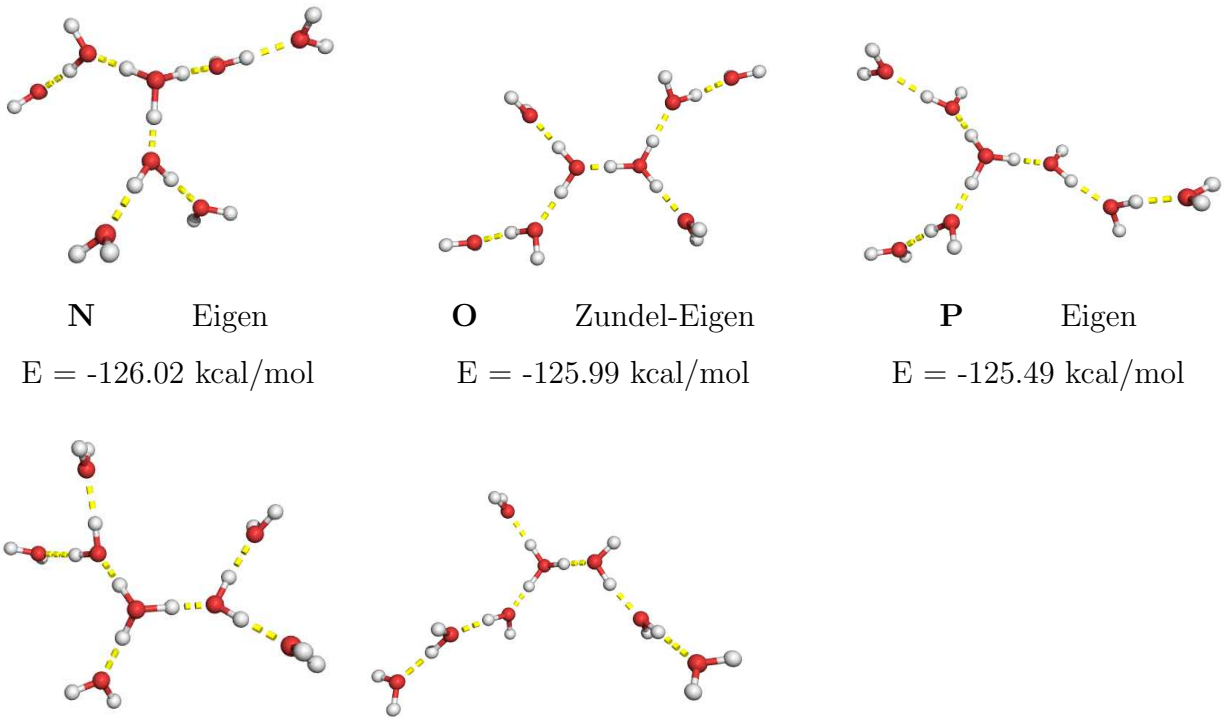

Figure 24: Five branched-type minima of $H^+(H_2O)_8$, together with their binding energies, recovered from parallel tempering Monte Carlo simulation trajectories. (These are obtained by optimizing structures sampled at each of the 32 simulation temperatures.)

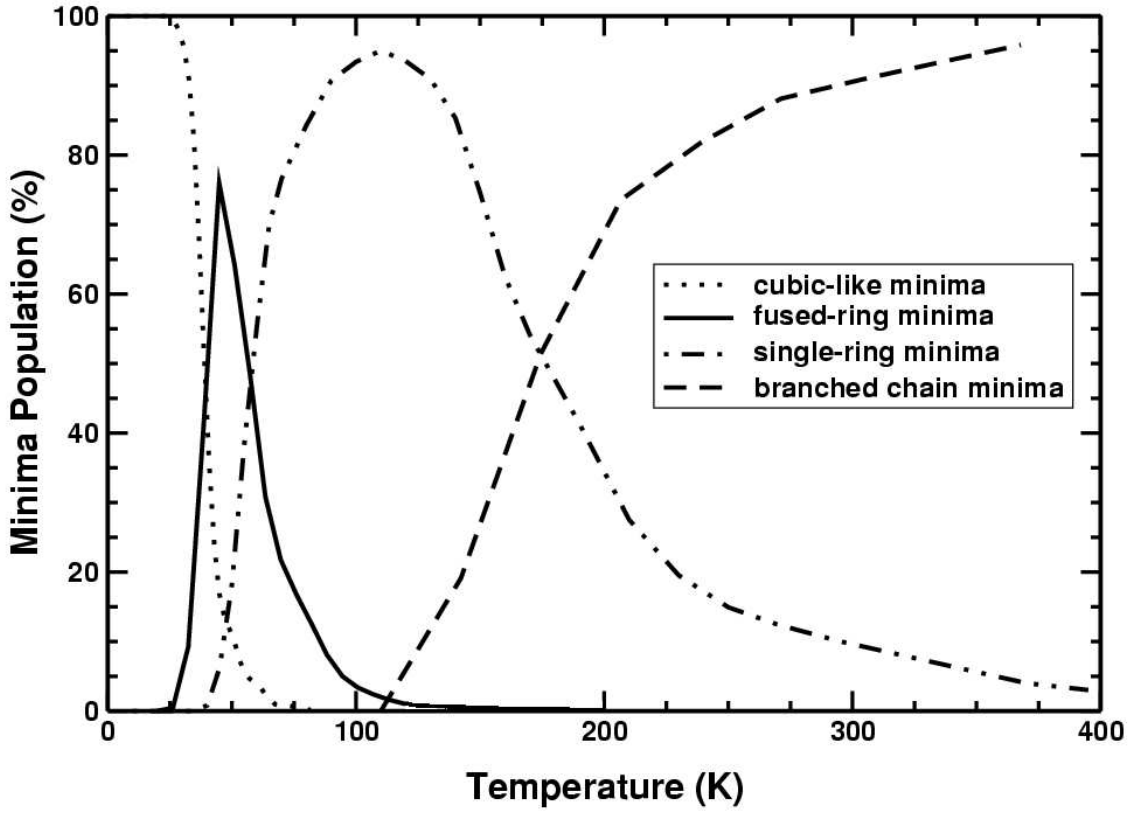

Figure 25: Variation in population of various inherent structures of $H^+(H_2O)_8$ with temperature. The "cubic"-like, fused-ring, single-ring and branched minima correspond to the structures presented in Figures 21-24, respectively.

Figure 26 presents the distributions of inherent structures sampled during the simulations carried out at T=50 K and 150 K, which fall near the maxima in the heat capacity curve. Both distributions have three peaks, corresponding to three distinct sets of minima. In the 50 K simulation, the lowest energy peak corresponds to the "cubic"-like minima, the intermediate peak to fused two-ring minima, and the highest energy peak to single-ring type minima (especially **I**). The lowest energy peak in the distribution generated at 150 K corresponds to the single-ring minima (especially **I**); the intermediate peak to higher energy single-ring minima (e.g., **J**-**M**), and the highest energy peak to the branched minima. It should be noted that there are actually far fewer distinct inherent structures than conveyed by this figure. The apparent larger number of distinct minima in Figure 26 is a reflection of the difficulty in fully optimizing these structures due to the existence of rather flat regions on the potential energy surface and the use of the steepest descents algorithm.

Jiang *et al.*[48] interpreted their IR spectra in terms of minima **I**, with a five-membered ring and the proton localized in a $H_5O_2^+$ type entity. The present simulations indicate that **I** and various branched structures have large populations at T=170 K, the estimated temperature of the clusters observed experimentally.

Although the heat capacity curve of $H^+(H_2O)_8$ displays two pronounced peaks, it is not clear that either of these should be attributed to cluster melting. Although our optimizations are not exhaustive, it does appear as though the density of local minima is relatively low over the -132.3 to -124.0 kcal/mol range. This fact, combined with the fact that the histograms of unquenched potential energies (not shown) of the configurations sampled near the two maxima (at T=50 and 150 K) are not bimodal, leads us to conclude that the transitions should probably not be viewed as melting transitions.

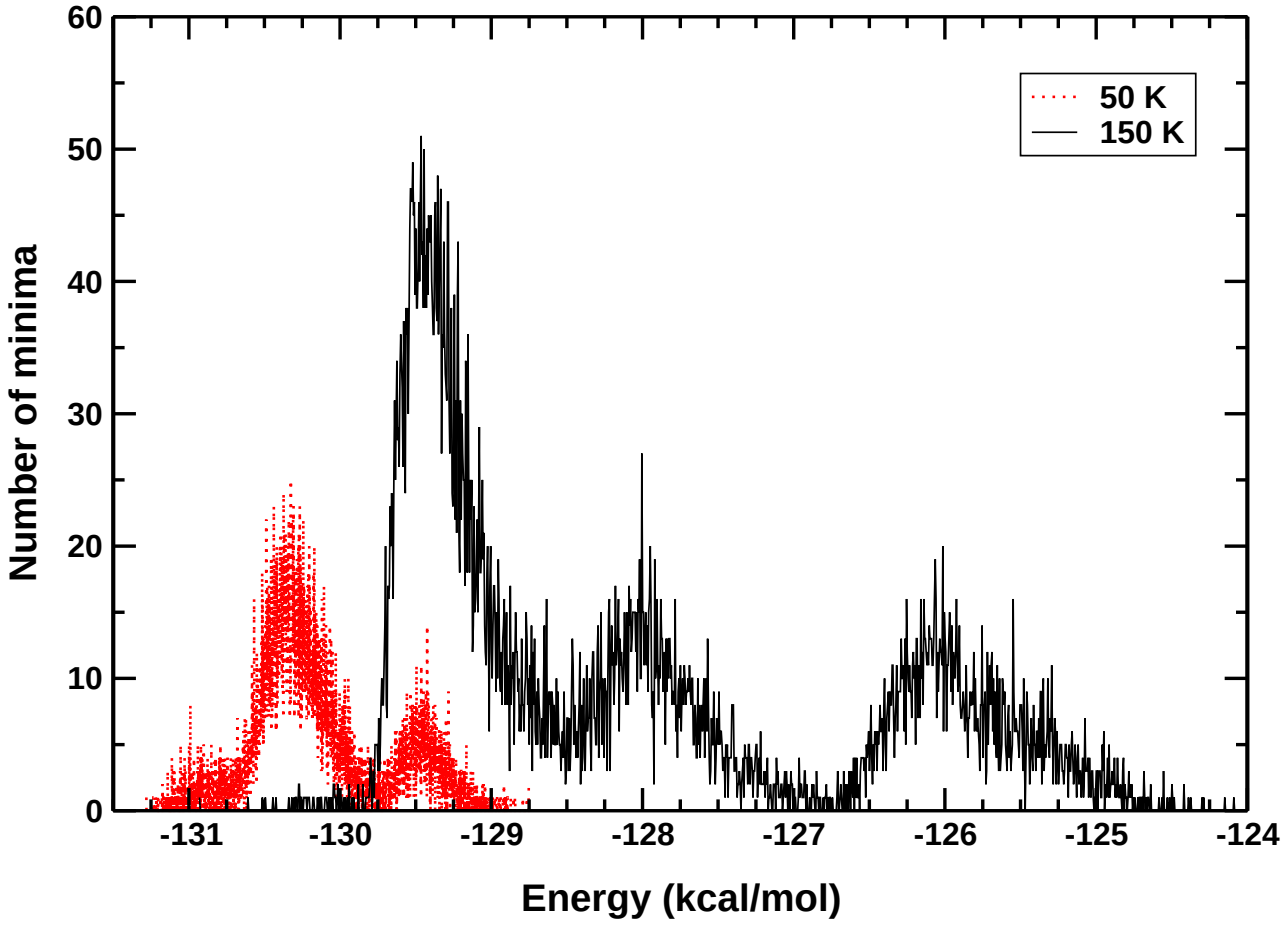

Figure 26: Histogram of $H^+(H_2O)_8$ minima energies obtained from the optimized structures recovered from trajectories of parallel tempering Monte Carlo simulations carried out at 50 K and 150 K. As discussed in the text, the optimizations are not fully converged, making it appear as though there are more local minima than actually possessed by the cluster as described by the MSEVB model.

3.5 CONCLUSIONS

In this study the parallel tempering Monte Carlo method was used to investigate the thermal behavior of $H^+(H_2O)_6$ and $H^+(H_2O)_8$. There is no pronounced structure in the $C_V(T)$ plot of $H^+(H_2O)_6$, whereas the corresponding plot for $H^+(H_2O)_8$ shows two pronounced peaks, with the low temperature peak arising from transitions between "cubic"-like and fused-ring structures, and the high temperature peak from transitions between single-ring and branched-type minima. The local minima recovered by optimizing sampled configurations to their inherent structures reveal that the proton is found to be solvated in Zundel, Eigen and intermediate Zundel-Eigen structures. In both $H^+(H_2O)_6$ and $H^+(H_2O)_8$, the Zundel form is preferred at low temperatures, whereas Eigen-like structures are more populated at higher temperatures.

4.0 MONTE CARLO SIMULATIONS OF THE FINITE TEMPERATURE PROPERTIES OF $(H_2O)_6$

The following sections 4.1 through 4.6 were submitted for publication to *Theoretical Accounts of Computational Chemistry (TACC)*

4.1 ABSTRACT

The thermodynamic behavior of the $(H_2O)_6$ cluster has been the subject of several theoretical studies employing model potentials. This article reviews the earlier work and presents new results on the finite temperature properties of the $(H_2O)_6$ cluster calculated using a 2+3-body MP2-level intermolecular potential in a canonical Monte Carlo simulation at T = 220 K. Book and ring configurations are found to dominate the sampled configurations. The finite histogram method of Ferrenberg and Swendsen [Phys. Rev. Lett. 61 (1988), 2635] is used to calculate the energy and energy fluctuations over a range of temperatures. The resulting heat capacity curve displays a broad peak near T = 135 K.

4.2 INTRODUCTION

Water clusters have been studied extensively both experimentally and theoretically over the past two decades. Among the issues that have been addressed are the geometrical structures of the low-energy isomers,[93,102,108,110,127,128,129,130,131,132,133,134,135,136,137,138,139,140,141] the role of cooperative effects in the bonding,[142,143,144,145,146,147,148] the sensitivity of the vibra-

tional and rotational spectra on the H-bonding arrangements,[149,150,151,152,153,154,155,156,157,158] the dynamics of isomer interconversion,[109,159,160] and the finite temperature behavior of the clusters.[101,107,109,112,113,115,120,161,162]

The water hexamer is one of the most thoroughly studied water clusters. Nevertheless, while it is well established that the smaller $(H_2O)_{3-5}$ clusters have cyclic global minimum structures, and that $(H_2O)_7$ and larger clusters have 3-dimensional fused-ring global minima,[16,127,153,155,156,163] the situation regarding $(H_2O)_6$ has taken much longer to sort out.

During the late 1980s and early 1990s several groups investigated theoretically the low-lying isomers of $(H_2O)_6$ as characterized by model potentials. In particular, Kim *et al.*[130] used the MCY potential[164] both by itself as well as augmented with three- and four-body interactions,[165,166] Belford and Campbell[167] used the Campbell-Mezei water model,[168] Schröder[169] employed the QPEN/B2[170] potential, Dykstra and coworkers[171,172] carried out calculations with the MCY, MMC[173,174] and TIP4p[122] models, and Vegiri and Farantos[162] investigated $(H_2O)_6$ using the CKL potential.[175] One of the most thorough studies of the energy landscape of the water hexamer was carried out by Tsai and Jordan[108] using an eigenmode-following algorithm with the TIP4p model potential. The energy disconnectivity diagram of $(H_2O)_6$ was first plotted by Wales *et al.*[176] for the rigid TIP4P and ASP-W4[134,147] potentials, and by Burnham *et al.*[177] for the flexible TTM2-F potential.[178] The topology of the H-bonding network of the low-lying isomers of $(H_2O)_6$ was studied by Tissandier *et al.*[179]

The energy ordering of the low-energy isomers of $(H_2O)_6$ varies from one model potential to another, clearly indicating the limitations of the water models available at the time these studies were carried out. Depending on the model potential employed the cage (**A**, Fig. 27), prism (**C**, Fig. 27), open-book (**D**, Fig. 27) and ring isomers (**B**, Fig. 27) have all been predicted to be the global minimum. Pedulla *et al.*[148] have compared the relative energies of the various isomers calculated with several model potentials and MP2-level electronic structure calculations.

Kim *et al.*[130] were apparently the first to apply *ab initio* methods to $(H_2O)_6$, carrying out SCF optimizations of the hexamer as early as 1988. However, as it became possible to carry out MP2 calculations with suitably flexible basis sets on water clusters, it became clear that including electron correlation effects are crucial for describing the bonding

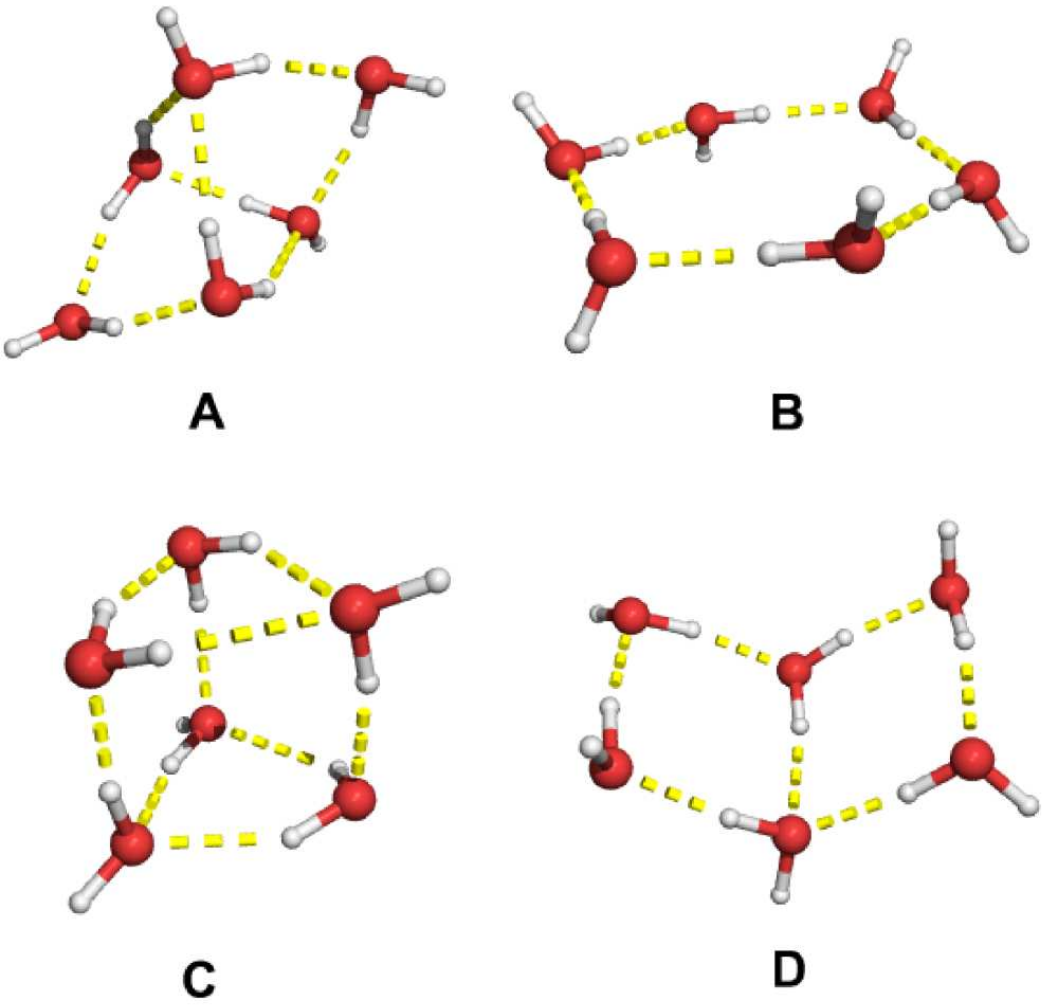

Figure 27: Four low-lying isomer types of $(H_2O)_6$; the cage (**A**), ring (**B**), prism (**C**) and book (**D**) isomers

in these species.[108,128,133,142,145,180,181] The first MP2 level calculations on $(H_2O)_6$ were by Tsai and Jordan.[108] Subsequently, Kim and coworkers,[182,183] Xantheas *et al.*,[184] Pedulla *et al.*,[148] Kryachko,[185] and Losada and Leutwyler[186] have characterized the low-energy isomers of $(H_2O)_6$ at the MP2 level and employing large, flexible basis sets. There have also been several other *ab initio* studies of the hexamer.[187,188] In addition, the role of vibrational zero-point energy has been investigated in both the harmonic[108,127,186] and anharmonic approximations.[16,144,189,190] These calculations reveal that the cage, book and ring isomers are of comparable energy, with the most stable prism-like isomer being a few tenths of a kcal/mol less stable. Over the past few years the cage,[16,191] book[192,193] and ring[194,195] structures have all been observed experimentally.

The thermodynamic properties of $(H_2O)_6$ have also long been of interest, with Monte Carlo and molecular dynamics simulations having been carried out using several different model potentials.[101,111,113,162] Although some of these studies concluded that $(H_2O)_6$ undergoes a melting transition (*e.g.*, Ref.[162]), others (*e.g.*, Ref.[113]) concluded that this system does not display a clear-cut melting transition. Obviously the sensitivity of the relative energies of the various isomeric forms of $(H_2O)_6$ on the model potential employed implies that none of the finite temperature simulations can be considered as definitive. While the simulations on $(H_2O)_6$ are unclear as to whether this species undergoes a melting transition, the consensus is that the slightly larger $(H_2O)_8$ cluster does undergo relatively sharp transformations between "solid-like" and "liquid-like" phases.[101,107,109,112,113,115,120,161,162] Although more sophisticated water models have been introduced recently,[177,196] these have yet to be applied to finite temperature simulations of water clusters.

To date, theoretical studies of the thermodynamic behavior of water clusters have been limited to model potentials,[101,107,111,113,115,120,162] although there have been studies that examined the temperature dependence of selected isomers[180,186] and others that have used DFT-based MD simulations to optimize structures and to calculate vibrational spectra.[93] In the absence of either experimental or *ab initio* data on the thermodynamic properties of small water clusters, it is difficult to assess the reliability of the simulations carried out with various model potentials. Although simulations of the thermodynamic properties of small water clusters are feasible with DFT methods, it has been found that DFT calculations with

commonly employed functionals such as Becke3LYP[94,95] incorrectly order various isomers of small water clusters.[197] This appears to be due to the inability of current density functionals to describe long-range dispersion interactions.[198,199] For this reason, it is preferable that finite temperature simulations of water clusters be carried out using an appropriate wavefunction-based electronic structure method.

The MP2 method has been found to accurately describe the energetics of water clusters, providing that sufficiently flexible atomic basis sets are employed.[128,133,142,180,181] However, while MP2 calculations are feasible for clusters containing up to 30 or so water molecules, the steep ($O(N^5)$) computational scaling of conventional MP2 calculations with system size precludes their use in carrying out Monte Carlo or molecular dynamics simulations of water clusters containing six or more monomers.

It is known from studies using model potentials that even for a cluster as small as $(H_2O)_6$, Monte Carlo simulations at temperatures between 50 and 200 K (the range typically considered to examine the issue of cluster melting) need to be carried out for on the order of 10^6 moves to achieve convergence. Such simulations at the MP2 level would take on the order of one year of CPU time (although this could be reduced to a few weeks or even days of wall clock time with an efficient parallel MP2 code and enough CPUs). For larger clusters, even longer simulation runs would be required and it would also be necessary to employ an algorithm such as parallel tempering[114] to achieve convergence, particularly at low temperatures. The parallel tempering algorithm requires the use of a grid of temperatures, further increasing the costs of the calculations. For these reasons, simulations of the thermodynamic properties of water clusters the size of the hexamer or larger using traditional MP2 methods would be a computationally daunting task even on parallel computers. A significant reduction in the CPU time could be achieved by use of localized 2nd-order Møller-Plesset perturbation theory (LMP2[200,201,202,203]) or resolvent of the identity 2nd-order Møller-Plesset perturbation theory (RIMP2[204,205]) methods, but there would still be the bottleneck introduced by the Hartree-Fock (HF) portion of the calculations. Although there are linear scaling HF codes,[206] they have not been combined with fast MP2 methods such as LMP2 or RIMP2.

These considerations have led us to consider an alternative approach based on a n-body decomposition procedure for carrying out Monte Carlo simulations on small water clusters

with MP2-level energies. The n-body decomposition procedure is described in the following section. This is followed by application to a Monte Carlo simulation of the study of the $(H_2O)_6$ cluster. As noted above, previous model potential simulations have predicted the $(H_2O)_6$ cluster to exist in a wide range of hydrogen bonding topologies, making this a good model to test the n-body decomposition procedure.

4.3 METHODOLOGY

In the n-body decomposition procedure, the total binding energy is written as

$$E = E^{(1)} + E^{(2)} + E^{(3)} + \ldots + E^{(n)}, \tag{4.1}$$

where $E^{(i)}$ denotes the "ith" body contribution to the interaction energy and the various energy terms depend on the appropriate nuclear coordinates. $E^{(1)}$ is simply the relaxation energy, which reflects the change in the energies of the monomers due to the geometrical distortions that occur when they are incorporated in the cluster. $E^{(2)}$ is the two-body interaction energy which can be obtained by performing calculations on all dimer pairs and $E^{(3)}$ is the three-body energy obtained by performing calculations on all possible trimers in the cluster, *etc.*

A significant body of work has shown that, for water clusters, the many-body effects are dominated by the three-body terms, *i.e.*, that

$$E \approx E^{(1)} + E^{(2)} + E^{(3)}, \tag{4.2}$$

provides a good approximation to the total binding energy of a water cluster as well as to the relative energies of different isomers of a given cluster.[143,145] This suggests a strategy of basing an MP2-level Monte Carlo simulation procedure on Eq. 4.2. Truncated n-body approaches have been used in water model potentials (most notably, the NCC[207,208] and SAPT[209,210,211] potentials), however we are unaware of this approach having been employed in conjunction with *ab initio* Monte Carlo simulations. For simplicity, in the remainder of this work we will assume that the monomers are kept rigid (*i.e.*, $E^{(1)} = 0$ in Eq. 4.2).

For a cluster containing N molecules, the evaluation of the $E^{(2)}$ contributions require $N(N-1)/2$ separate dimer calculations and $E^{(3)}$ requires $N(N-1)(N-2)/3$ separate trimer calculations. In the absence of other computational savings, the n-body decomposition procedure truncated at the $E^{(3)}$ term, would not offer an advantage over supermolecule LMP2 calculations with a code such as Jaguar[212] where both the HF and LMP2 steps are carried out using pseudospectral algorithms.

Thus far, we have focused on the cost of performing a single total energy calculation. In Monte Carlo simulations in which each step in the simulation involves a displacement (translation or rotation) of a single molecule, one needs only to compute the contributions to $E^{(2)}$ and $E^{(3)}$ involving the monomer that was moved. In this case, the number of terms that need to be evaluated is of the order $(N-1)$ and $(N-1)(N-2)/2$, for $E^{(2)}$ and $E^{(3)}$, respectively. As a result, the truncated 2+3-body approach provides a significant computational savings compared to that required with the more conventional supermolecule approach for carrying out MP2-level Monte Carlo simulations of cluster systems.

There are several additional opportunities for computational savings in the 2+3-body Monte Carlo simulation procedure. These include: (i) use of the LMP2 or RIMP2 methods for calculating the correlated energies, (ii) use of different levels of theory for the 2- and 3-body interaction energies, and (iii) use of different approaches for treating short-range and long-range interactions. In the present study, the first two of these cost-saving features were adopted. Namely, the two-body energies were calculated using Saebø and Pulay's[200,201,202,203] implementation of the LMP2 method, and the Hartree-Fock method was used to calculate the 3-body interactions. Compared with the standard MP2 approach, LMP2 has the advantages of lower computational cost and reduced basis set superposition error (BSSE[100]) in the correlation energy. The adoption of the HF method for calculating the 3-body interaction energies was motivated by the observation that electron correlations play only a small role in describing such interactions in H-bonded clusters.[102,148,211] No attempt was made in this study to exploit the use of a less computationally demanding method for the long-range two- or three-body energies. The various 2- and 3-body interactions were farmed out to multiple CPUs on a Beowulf cluster. Care was taken in dividing up the various interaction terms to ensure that the CPUs were efficiently used.

The simulations were carried out with the 6-31+G(d) basis set[213,214,215] as well as with a more flexible mixed cc-pVDZ[98]/aug-cc-pVDZ[99] (for H/O atoms, respectively) basis set, hereafter referred to as apVDZ. The electronic structure calculations were carried out using the MOLPRO program package (version 2002.3).[216]

The Monte Carlo simulations were carried out in the canonical ensemble and at temperatures of T = 100 and 220 K with the 6-31+G(d) basis set and at T = 220 K for the larger apVDZ basis set. A constraining sphere with a radius of r=5.5 Å was employed to prevent evaporative events during the simulation. Each simulation was carried out for 1.1×10^5 Monte Carlo moves, with the first 1×10^4 moves being for equilibration and the last 10^5 moves being employed in the averaging. Based upon earlier work with model potentials, it is known that the $(H_2O)_6$ system is relatively easy to equilibriate, especially at a temperature as high as T = 220 K. Nonetheless, it would be desirable to carry out longer simulations (*e.g.*, for 10^6 Monte Carlo moves) to ensure better convergence. This was not done because of the limitations of the Beowulf cluster available for the calculations (1 GHz Pentium III CPUs), and because the primary purpose of this study is to demonstrate the feasibility of 2+3-body MP2-level simulations on $(H_2O)_n$ clusters rather than to do definitive calculations.

The average interaction energies $\langle E\rangle$, $\langle E^{(2)}\rangle$ and $\langle E^{(3)}\rangle$ and their fluctuations (in the form of dimensionless heat capacities), were calculated. The constant volume, configurational heat capacity was calculated from the standard expression

$$\bar{C}_V = C_V/k_B = \frac{\sigma^2(E)}{(k_BT)^2} = \frac{\langle E^2\rangle - \langle E\rangle^2}{(k_BT)^2}. \tag{4.3}$$

In a similiar manner, the 2- and 3-body components to the total heat capacity, were calculated as

$$\begin{aligned}\bar{C}_V^{(2)} &= C_V^{(2)}/k_B \\ &= \frac{\langle E^{(2)}(E^{(2)}+E^{(3)})\rangle - \langle E^{(2)}\rangle\langle E^{(2)}+E^{(3)}\rangle}{(k_BT)^2},\end{aligned} \tag{4.4}$$

and

$$\begin{aligned}\bar{C}_V^{(3)} &= C_V^{(3)}/k_B \\ &= \frac{\langle E^{(3)}(E^{(2)}+E^{(3)})\rangle - \langle E^{(3)}\rangle\langle E^{(2)}+E^{(3)}\rangle}{(k_BT)^2},\end{aligned} \tag{4.5}$$

where these equations were obtained by differentiating $\langle E^{(2)} \rangle$ and $\langle E^{(3)} \rangle$ with respect to T. To provide insight into the interdependence of $E^{(2)}$ and $E^{(3)}$, the covariance

$$c^{(2),(3)} = \frac{\langle \delta E^{(2)} \delta E^{(3)} \rangle}{\sigma(E^{(2)}) \sigma(E^{(3)})}, \tag{4.6}$$

where $\delta E^{(2)} = E^{(2)} - \langle E^{(2)} \rangle$, $\delta E^{(3)} = E^{(3)} - \langle E^{(3)} \rangle$, $\sigma(E^{(2)}) = \sqrt{\langle (E^{(2)})^2 \rangle - \langle E^{(2)} \rangle^2}$, and $\sigma(E^{(3)}) = \sqrt{\langle (E^{(3)})^2 \rangle - \langle E^{(3)} \rangle^2}$, was calculated. In a similar fashion, the covariance between the HF 2-body and LMP2 2-body energy components was calculated from

$$c^{\mathrm{HF,LMP2}} = \frac{\langle \delta E^{(2)}_{\mathrm{HF}} \delta E^{(2)} \rangle}{\sigma(E^{(2)}_{\mathrm{HF}}) \sigma(E^{(2)})}. \tag{4.7}$$

The single histogram method of Ferrenberg and Swendsen[217] was used to estimate the average energies over a range of temperatures. In this approach, configurations saved from a simulation at a temperature T, were used to calculate the energy at other temperatures T$'$, using

$$\langle E(\beta') \rangle = \frac{\sum_v E_v(\beta) \, \exp\{-(\beta' - \beta) E_v\}}{\sum_v \exp\{-(\beta' - \beta) E_v\}}, \tag{4.8}$$

where the sums are over all configurations sampled in the simulation at T, and $\beta = 1/kT$ and $\beta' = 1/kT'$.

4.4 RESULTS

4.4.1 Energetics of $(H_2O)_6$; Basis set and Thermal Effects

Table 7 presents the energies from the 2+3-body LMP2 simulation of $(H_2O)_6$ carried out at 220 K. The average binding energy from the simulation is -31.39 kcal/mol. Of this, the average 2-body binding energy is -26.98 kcal/mol, -22.25 kcal/mol of which is recovered at the HF level. The average 3-body energy is -4.41 kcal/mol, which accounts for about 14.0% of the total average binding energy and which is close to the percentage contribution of three-body interactions to the binding in bulk liquid water at 298 K, where the 3-body contribution has been estimated to be 14.5% of the net cohesive energy.[211]

Table 7: Energy and energy fluctuations of $(H_2O)_6$ from mixed cc-pVDZ/aug-cc-pVDZ LMP2 Monte Carlo simulation at T = 220 K.

Property	HF	LMP2
$\langle E^{(2)} \rangle$ (kcal/mol)	-22.25	-26.98
$\langle E^{(3)} \rangle$ (kcal/mol)	-4.41	-4.41[a]
$\langle E \rangle$ (kcal/mol)	-26.66	-31.39
$\sigma^2(E^{(2)})$ (kcal/mol)^2	2.86	2.70
$\sigma^2(E^{(3)})$ (kcal/mol)^2	1.28	–
$\sigma^2(E)$ (kcal/mol)^2	3.52	3.98

[a] the 3-body contributions were calculated only at the HF level of theory

The 3-body terms are even more important for the energy fluctuations than for the total interaction energy, accounting for over 32% of the total energy fluctuations in the T = 220 K MP2/apVDZ simulation. $|c^{(2),(3)}| = 0.08$, which indicates that there is little statistical correlation between the 2- and 3-body energies of $(H_2O)_6$ at T = 220 K. $\sigma^2(E^{(2)})$ is nearly the same for the Hartree-Fock and LMP2 energies. Also, $|c^{\mathrm{LMP2,HF}}| = 0.89$, which implies that (not suprisingly) there is a strong correlation between the HF and LMP2 2-body energies.

4.4.2 Error analysis of the truncated n-body approximation for E

In order to evaluate the accuracy of the truncated 2+3-body approach employed in this study, supermolecule LMP2 calculations with the mixed cc-pVDZ/aug-cc-pVDZ basis set were carried out on 200 structures selected from the apVDZ simulation trajectory. A comparison of the energies from the two methods is presented in Figure 28, from which it is seen that the errors in the total energies due to the use of the 2+3-body approach are relatively small. The average absolute error is calculated to be 0.22 kcal/mol, which is less than 0.7% of the total interaction energy. The largest error in the 2+3-body energy for an individual

structure is 0.64 kcal/mol. As indicated by Figure 28, in the vast majority (97%) of structures, the truncated n-body approach slightly underestimates, in magnitude, the full 6-body binding energy.

4.4.3 Inherent Structures

To gain further insight into the nature of the $(H_2O)_6$ cluster at T = 220 K, every 100th configuration from the simulation using the apVDZ basis set was saved and subsequently optimized to its inherent structure using the flexible water model potential of Ren and Ponder.[196] Ring-based isomers (**B** from Figure 27, 65.5%) are found to be the dominant inherent structure. Book-based isomers (**D** from Figure 27, 24.7%), prism-based (**C** from Figure 27, 4.5%), and cage-based (**A** from Figure 27, 3.3%) isomers also have significant population. The remaining inherent structures ($< 2.0\%$) consist of isomers with one or more ring system (but distinct from the isomers **A**-**D**). This distribution of inherent structures is similar to that found from Monte Carlo simulations[113] at T = 220 K and using the TIP4p water models.

4.4.4 Radial Distribution Function

Figure 29 reports the oxygen-oxygen partial radial distribution function, $g_{OO}(r)$, determined from the three 2+3-body MP2 simulations of $(H_2O)_6$. The maximum in the first peak in $g_{OO}(r)$ obtained from the T=220 K simulation with the apVDZ basis set occurs at r=2.82 Å, which is close to that (2.8 Å) observed experimentally for liquid water[218] under ambient conditions.

The value of $g_{OO}(r)$ for the first peak in Figure 29, 6.4, is appreciably higher than that ($\approx$ 2.8) determined experimentally[218] or calculated for bulk water.[211] This difference is a consequence of the normalization of $g_{OO}(r)$ for an ideal gas of the same density. The $g_{OO}(r)$ curve for $(H_2O)_6$ also displays a second peak centered near 4.40 Å in the T = 220 K simulation and near 3.95 Å in the T = 100 K simulation.

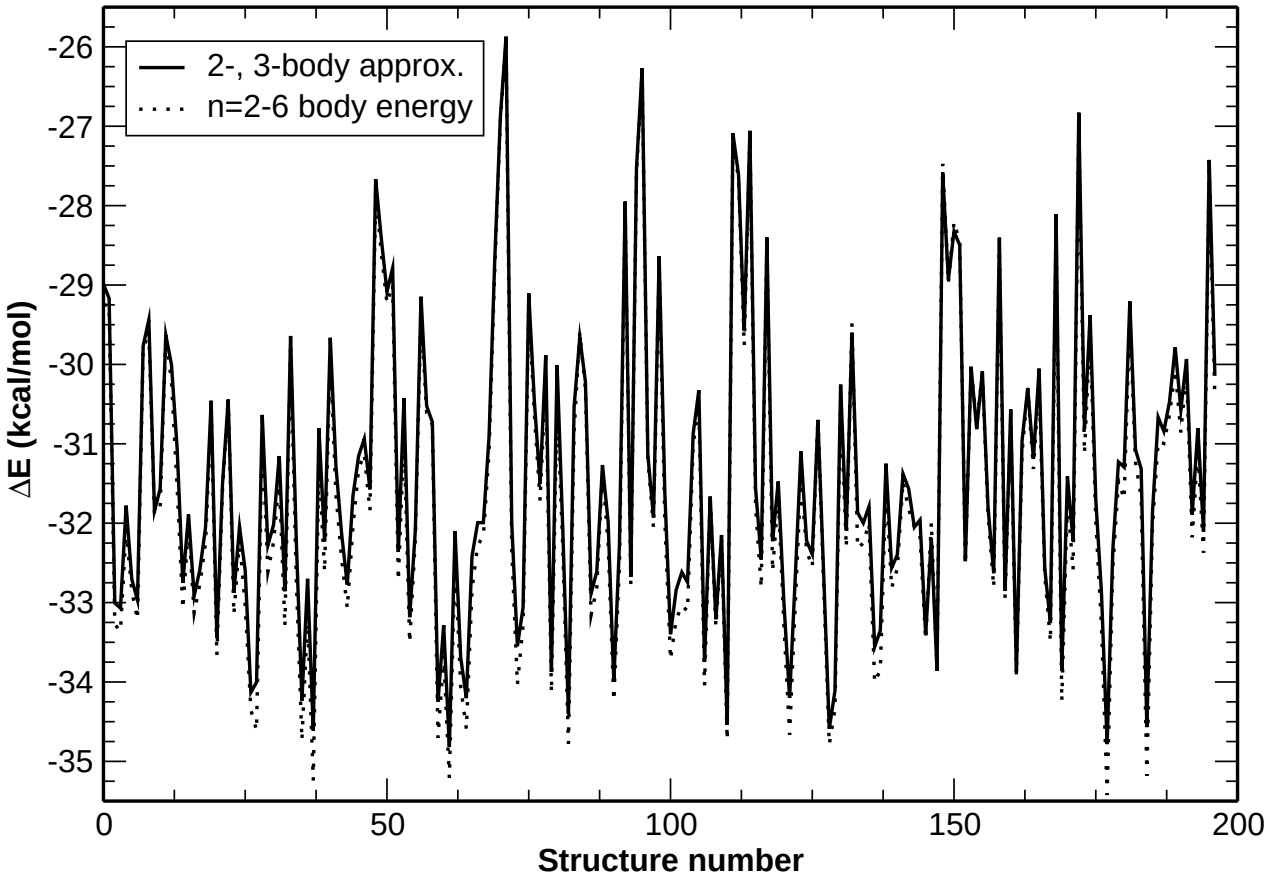

Figure 28: Error analysis of the 2+3-body approximation to E. The binding energies of 200 structures selected from the LMP2/apVDZ Monte Carlo simulation trajectory at T = 220 K were calculated using supermolecule LMP2 calculations (which also recover the $n = 4 - 6$ body interactions)

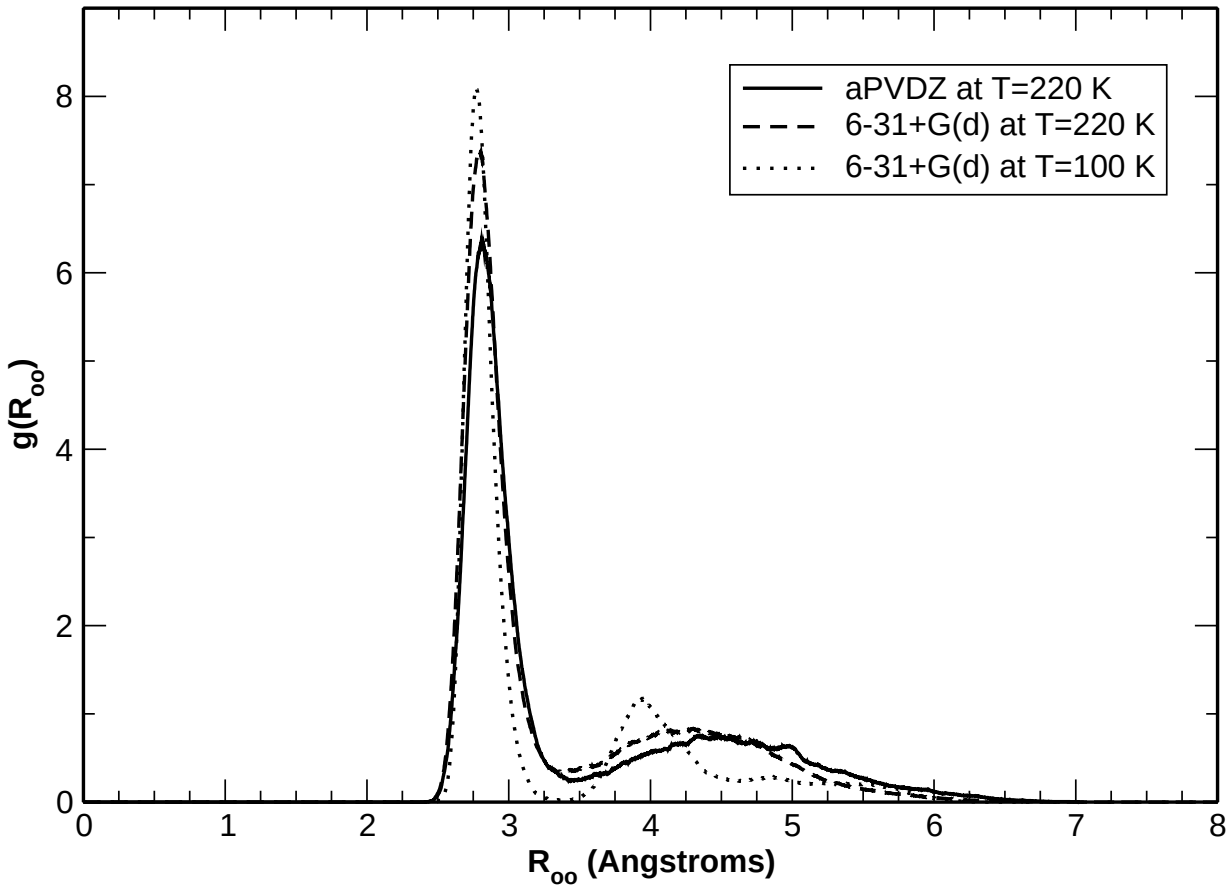

Figure 29: The oxygen-oxygen partial radial distribution functions, $g_{\mathrm{OO}}(r)$, from the Monte Carlo simulation using the apVDZ (at T = 220 K) and 6-31+G(d) (at T = 100 and 220 K) basis sets.

4.4.5 Temperature dependence of the energy and heat capacity of $(H_2O)_6$

Plots of the temperature dependence of the total binding energy and of the 2- and 3-body contributions obtained from the histogram procedure are presented in Figure 30. The total binding energy varies from -37.69 kcal/mol at T = 25 K to -29.41 kcal/mol at T = 270 K, with there being an inflection point near 130 K. Both $E^{(2)}$ and $E^{(3)}$ decrease in magnitude with increasing temperature, with the result being that their sum decreases more rapidly than does $E^{(2)}$ alone. The shape of the $E^{(2)}$ curve calculated at the MP2 level is nearly identical to that calculated at the Hartree-Fock level, with the former being lower by about 5 kcal/mol. This is suprising given the contribution of dispersion interactions to the MP2 energies. The 3-body contribution ranges from 19.8% of the total interaction energy at T = 25 K, to 12.9% at T = 270 K.

The calculated (dimensionless) heat capacity curve is presented in Figure 31. The total heat capacity, $\bar{C}_V$ increases from 0.22 at T = 25 K to a maximum of 24.35 near T = 135 K, and then decreases slowly between T = 135 and 270 K. In addition, $\bar{C}_V$ also has a shoulder near T = 65 K. The temperature dependence of $\bar{C}_V$ for $(H_2O)_6$, calculated by using the histogram procedure and the 2+3-body LMP2 simulations, is close to that obtained from J-walk Monte Carlo simulations[101] of $(H_2O)_6$ using the TIP4p[122] and NCC[207,208] model potentials.

The 2-body component to the heat capacity, $\bar{C}_V^{(2)}$, has a minimum at T = 65 K, close to the temperature of the shoulder in the $\bar{C}_V$ curve. The shoulder, in fact, arises from the 3-body contribution to $\bar{C}_V$ which is calculated to have maxima near T = 60 and 120 K. For temperatures between 30 and 110 K, the three-body contribution to the energy fluctuations actually exceeds the two-body contributions.

The temperature dependencies of $c^{\mathrm{HF,LMP2}}$ and $c^{(2),(3)}$ deduced from the histogram analysis are reported in Figure 32. $c^{\mathrm{HF,LMP2}}$ shows little variation in temperature, ranging from 0.88 to 0.98. On the other hand, $c^{(2),(3)}$ is relatively flat between T=25 and 70 K and grows rapidly from about -0.90 to 0.22, as T increases from 70 to 270 K.

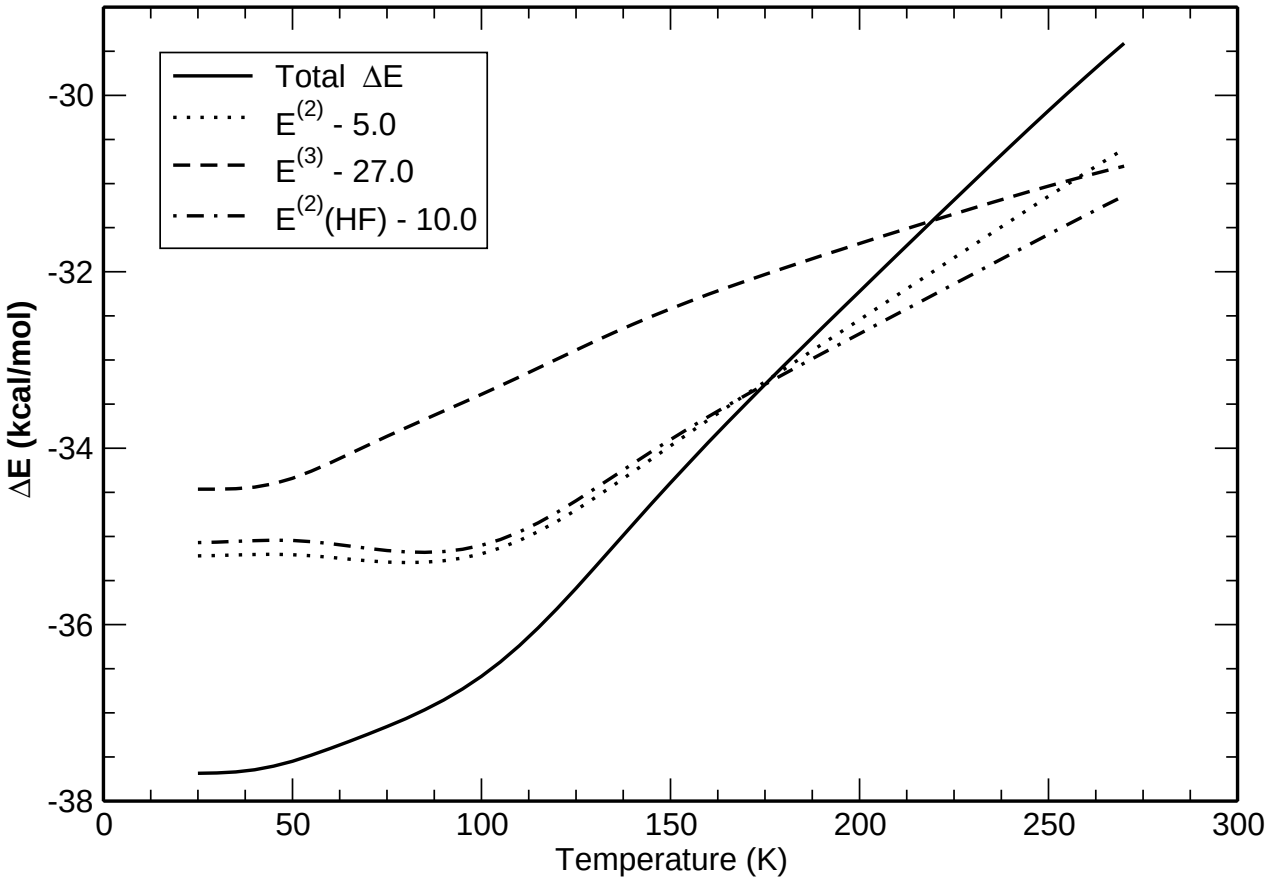

Figure 30: Finite temperature behavior of the binding energy components of the LMP2/apVDZ Monte Carlo simulation at T = 220 K. To facilitate comparison with the total energy, the 2-body, 3-body and HF 2-body energy components were shifted by constant values of 5.0 kcal/mol, 27.0 kcal/mol and 10.0 kcal/mol, respectively.

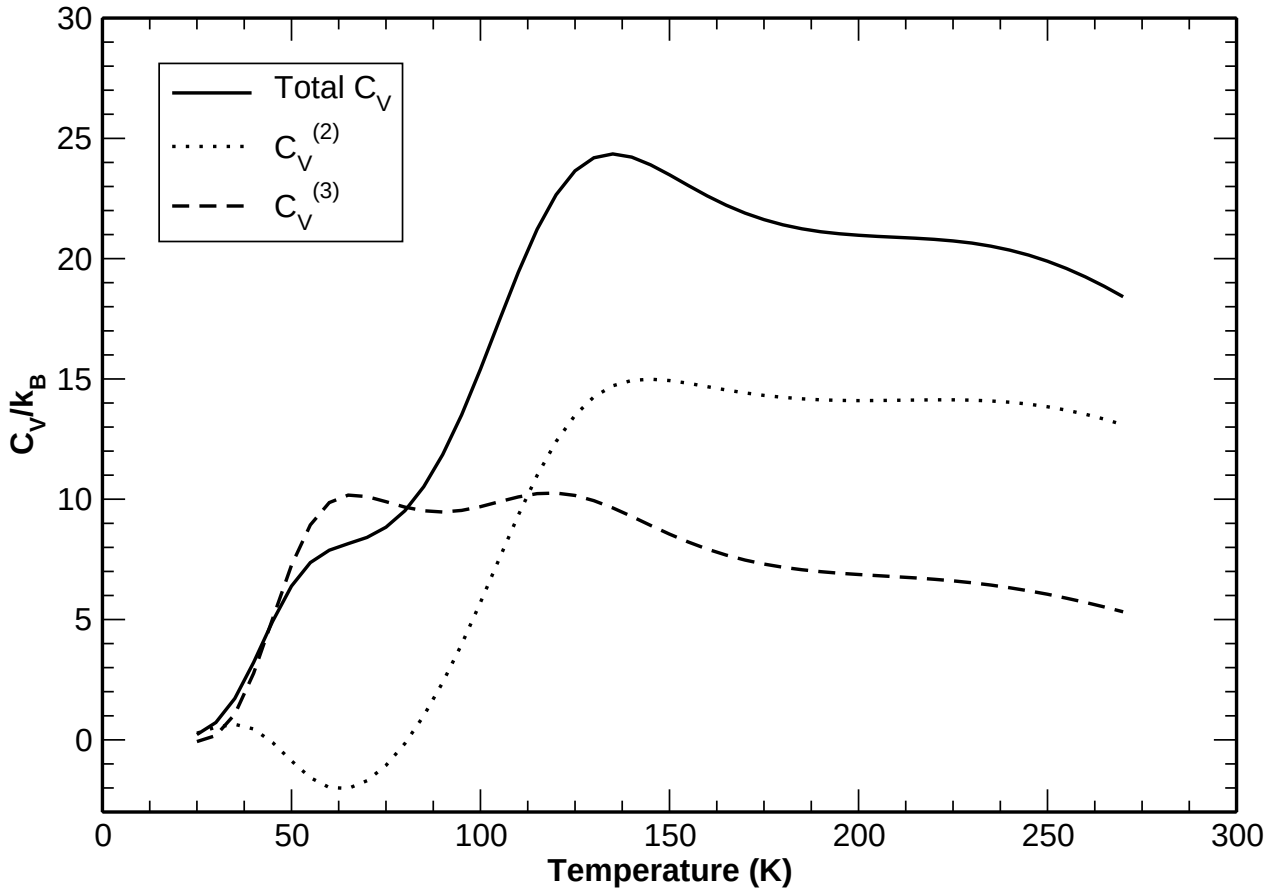

Figure 31: Finite temperature behavior of the components of the dimensionless, configurational constant volume heat capacity (from Equations 4.3, 4.4 and 4.5 from the LMP2/apVDZ simulation at T = 220 K.

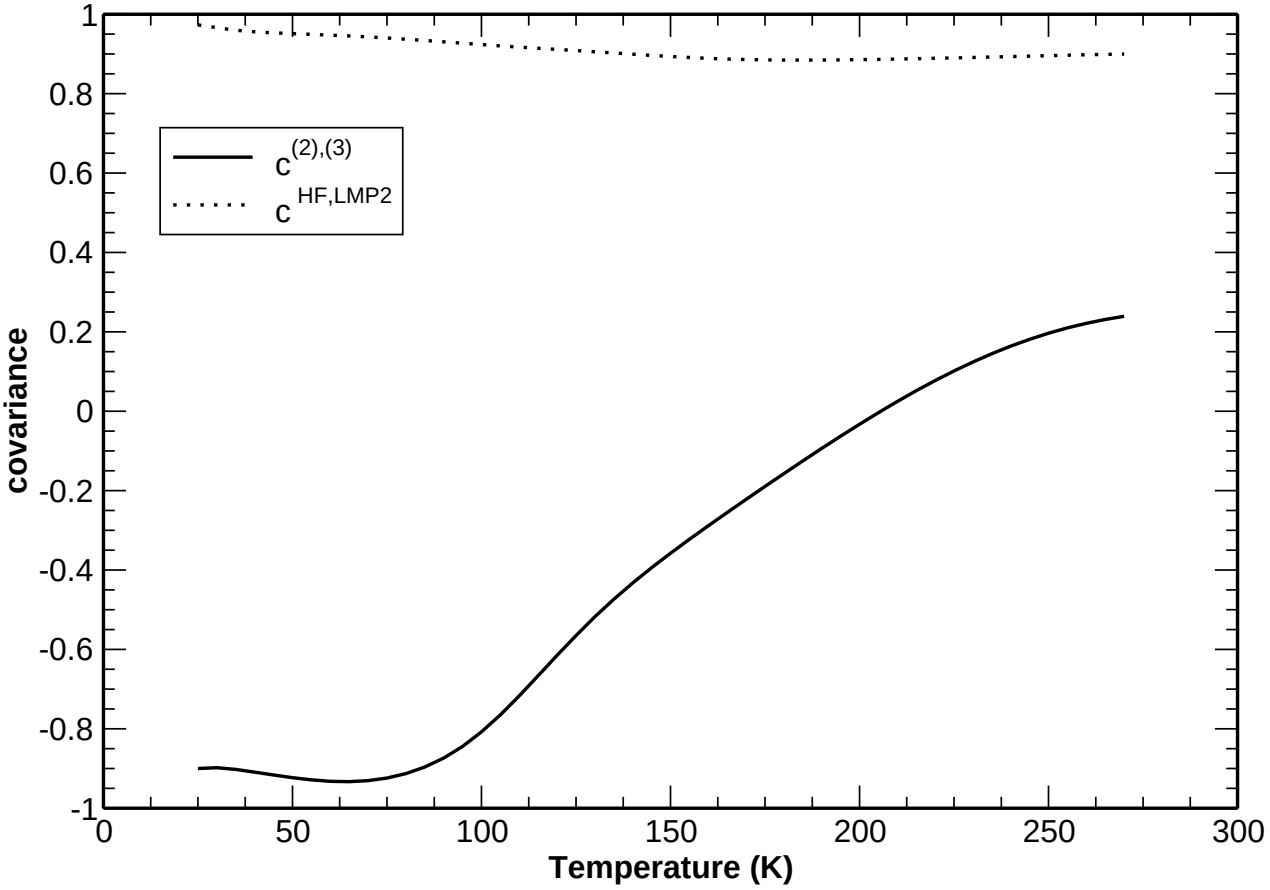

Figure 32: Covariance function $c^{(2),(3)}$ for the 2- and 3-body energies, and $c^{\mathrm{LMP2,HF}}$ for the HF and LMP2 2-body energies.

4.5 CONCLUSIONS

The water hexamer has been studied extensively experimentally and theoretically. Although there have been several calculations on the dependence of various properties of $(H_2O)_6$ as a function of temperature, the results have proven to be quite sensitive to the model potential employed. In this study, a new approach was adopted in which the finite temperature properties of the hexamer were studied using an *ab initio* potential.

A 2+3-body MP2-level procedure was used to characterize the $(H_2O)_6$ cluster at T = 220 K. These results were used in a histogram procedure to predict the potential energy and heat capacity of the cluster over a range of temperatures. At T = 220 K, the 3-body contributions are found to account for 14% of the total interaction energy, whereas the 3-body contribution to the total fluctuations is 32%. Comparison of the 2+3-body energies with full supermolecule LMP2 energies for a subset of sampled structures reveals that the average discrepancy between the two sets of energies is only 0.22 kcal/mol.

At T = 220 K, book and ring structures are predicted to account for over 90% of the configurations sampled in the simulation. This preponderance of ring and book isomers at T = 220 K is consistent with the results of previous model potential simulations.[113] The 2-body component of the interaction energy varies by over 8 kcal/mol from T = 25 to 270 K, while the 3-body component varies by about 3 kcal/mol over the same temperature range.

The percentage contribution of the 3-body component to the total potential energy varies from 20% at T = 25 K to 13% at T = 270 K. There is a weak maximum in the $\bar{C}_V$ *vs* T curve at T = 135 K. The functional behavior of $\bar{C}_V$ is of a similar form to that obtained from previous simulations employing the the NCC and TIP4P water potentials.[101] Based on earlier model potential studies,[113] this maximum is due to the transformation from cage and prism structures to the ring and open-book structures.

The 2+3-body LMP2/apVDZ simulations reported in this study required about three weeks on eight 1.0 GHz CPUs of a Beowulf computer cluster. By use of current, high-end CPUs and by running over 16 to 32 CPUs, 2+3-body MP2-level simulations for as many as 10^6 Metropolis moves would be feasible for clusters as large as $(H_2O)_{10}$. To extend the simulations to appreciably larger clusters requires the introduction of additional approxima-

tions, *e.g.*, using a cutoff for calculation of three-body interactions. The simplest approach for reducing the computational cost of the calculation of the 3-body interactions is to skip the evaluation of structures in which the distance of one of the monomers from the other two in a trimer exceeds a threshold distance. It is also possible to implement a scheme in which the three-body interactions are divided into three classes: (1) the short-range interactions, treated via *ab initio* electronic structure theory, (2) intermediate range interactions, treated using a classical polarization model, and (3) long-range interactions, which are neglected. With these strategies the 2+3-body LMP2 procedure could be used to carry out Monte Carlo simulations on clusters as large as $(H_2O)_{20}$, at least if the temperature is high enough that quasi-ergodicity is not a serious problem. Extension to still larger clusters would be possible by adoption of approximate procedures for estimating the two-body interactions between distant monomers.

4.6 ACKNOWLEDGEMENTS

This research was supported by a grant (CHE-0078528) from the National Science Foundation.

5.0 THE INFRARED SIGNATURE OF STRUCTURES ASSOCIATED WITH THE $H^+(H_2O)_N$ (N=6-27) CLUSTERS

This work was published as

J.-W. Shin, N. I. Hammer, E. G. Diken, M. A. Johnson, R. S. Walters, T. D. Jaeger, M. A. Duncan, R. A. Christie and K. D. Jordan, *Science* **2004**, *304*, 1137

5.1 ABSTRACT

We report the OH stretching vibrational spectra of size-selected $H^+(H_2O)_n$ clusters through the region of the pronounced "magic number" at $n = 21$ in the cluster distribution. Sharp features are observed in the spectra and assigned to excitation of the dangling OH groups throughout the size range $6 \leq n \leq 27$. A multiplet of such bands appears at small cluster sizes. This pattern simplifies to a doublet at $n = 11$, with the doublet persisting up to $n = 20$, but then collapsing to a single line in the $n = 21$ and $n = 22$ clusters and reemerging at $n = 23$. This spectral simplification provides direct evidence that, for the magic number cluster, all the dangling OH groups arise from water molecules in similar binding sites.

5.2 RESULTS AND DISCUSSION

The nature of the proton in water is one of the most fundamental aspects of aqueous chemistry, and one important aspect of the aqueous proton is its anomalously high mobility.[74,116] This phenomenon immediately introduces the crucial role of H_3O^+ and $H_5O_2^+$,

the so-called Eigen[18] and Zundel[219] forms of the cation, respectively. Fluctuations between these species[74,116] are thought to mediate the Grotthuss mechanism[220] for proton transport, and accurate simulations of this process require quantum treatment of the hydrogen motion in the complex network environment of bulk water.

A powerful way to test the validity of various theoretical methods is through the use of the cluster ions,[221] $H^+(H_2O)_n$, which can be prepared and isolated in the laboratory. Here we report size-selected vibrational spectra of the $H^+(H_2O)_n$ clusters in the intermediate size regime, $6 \leq n \leq 27$, chosen to explore the putative role[9,49,69,123,222,223] of dodecahedral clathrate structures in the region around $n = 21$. The resulting spectra are analyzed with the aid of calculated structures and vibrational frequencies of selected isomers for the $n = 20$ and $n = 21$ clusters.

Protonated water clusters have been studied for decades,[9,18,48,49,69,117,123,219,222,223,224,225,226,227] and in the small size regime ($n \leq 8$), vibrational spectra have been reported and interpreted with *ab initio* theory.[48] H_3O^+ itself is C_{3v} pyramidal,[224] but adding a second water molecule leads to a symmetrical sharing of the proton in the $H_2O\cdots H^+\cdots OH_2$ Zundel arrangement.[219,227] Larger protonated water clusters possess multiple low-energy isomers with both Eigen and Zundel forms of the cation, and the complexity of the observed spectra indicate that several isomers are present under experimental conditions.

One of the most curious aspects of the $H^+(H_2O)_n$ clusters is Searcy and Fenn's[49] report in 1974 of the discontinuity in the cluster ion intensity distribution or "magic number" at $n = 21$ (Fig. 33). There has been much speculation about the structure of the magic number cluster, especially because water clathrates are known to trap methane and other gases in water cages comprised of water dodecahedrons.[228] Indeed Searcy and Fenn[49] suggested that $H^+(H_2O)_{21}$ is also derived from the pentagonal dodecahedron motif, with one water molecule in the cage and the H_3O^+ ion on the surface.

In 1991, Castleman and co-workers reported a "titration" of dangling H atoms by attaching trimethylamine (TMA) molecules to the $H^+(H_2O)_{21}$ cluster.[9] They found a drop-off in the propensity to attach the 11th TMA molecule, which suggested that 10 H atoms are free (*i.e.*, not engaged in H-bonding) in the $H^+(H_2O)_{21}$ cluster. Because this is the same number as in the neutral $(H_2O)_{20}$ dodecahedron, these authors invoked a model with the

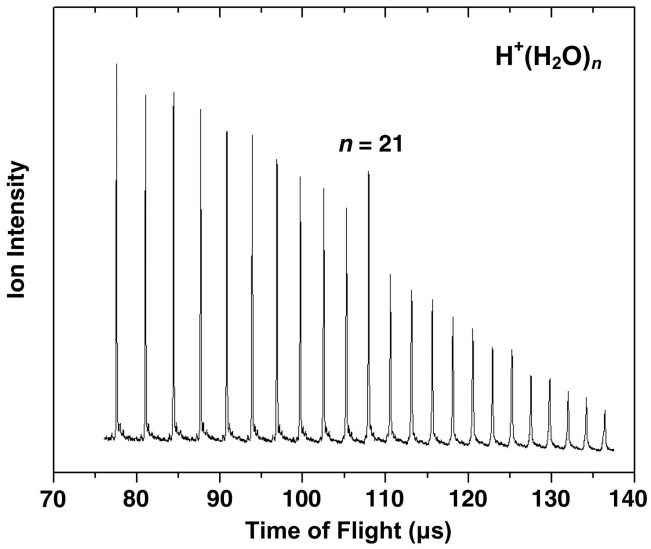

Figure 33: Mass spectrum of $H^+(H_2O)_n$, $11 \leq n \leq 33$, obtained with the use of an electron impact ion source.

H_3O^+ species located inside the pentagonal dodecahedron, as opposed to Fenn's surface ion structure,[49] which has only nine dangling H atoms.

Subsequent theoretical work indeed found dodecahedron-based structures to be stable. In the case of the $H^+(H_2O)_{21}$ cluster, the isomer with interior H_3O^+ was reported to be stable in Monte Carlo simulations,[69,117] using model potentials. However, other model potentials[123,226] and electronic structure calculations[223,225] have indicated that the isomer with hydronium located on the surface of the cage, with a neutral H_2O molecule in the center and nine free OH groups, lies appreciably lower in energy. This discrepancy with the TMA titration results raises the possibility that the act of ligation may have driven a morphological change in the delicate balance between isomeric forms of the $H^+(H_2O)_{21}$ species.

We therefore seek a diagnostic of structure less disruptive than ligand titration. Vibrational spectroscopy can monitor the character of the OH stretching vibrations of the larger clusters in isolation. Recent developments in size-selected infrared (IR) spectroscopy[229] now

enable this to be accomplished using laser photodissociation:[44,48]

$$H^+(H_2O)_n + h\nu \rightarrow H^+(H_2O)_{n-1} + H_2O, \tag{5.1}$$

and here we report the OH stretching spectra of the protonated water clusters in the critical size range. Clusters in this size range can now be characterized theoretically by means of all-electron electronic structure methods in conjunction with flexible basis sets to evaluate whether the putative structures are consistent with these new observations.

The spectra reported here are acquired in a size-selective fashion using tandem time-of-flight mass photofragmentation spectrometers.[230,231] In this method, the first mass-spectrometer isolates a particular cluster ion for laser excitation and the second one selectively detects the lighter fragments that form when absorption of a photon causes water molecules to evaporate. This method recovers the actual absorption spectrum only when the cluster of interest fragments upon absorption of a photon in the excitation energy range $2000 \leq h\nu \leq 4000$ cm^{-1}. In the large cluster regime, this requirement is often at odds with the need to keep the clusters as cold as possible so that they are quenched close to their lowest-energy structures. The reported spectra were taken under strong excitation conditions (5-15 mJ/pulse), which typically resulted in ejection of several water molecules via sequential multi-photon absorption. Another potential complication is that the observed species may be dependent on the method of preparation. We therefore measure spectra of $H^+(H_2O)_n$ using two different ion sources in different laboratories (Yale and Georgia).[232]

Figure 34(A) presents an overview of selected $H^+(H_2O)_n$ ($6 \leq n \leq 27$) spectra in the OH stretching region, for clusters from the Georgia ion source. As expected, the envelopes in the red-shifted range associated with H-bonding (3000 to 3600 cm^{-1}) are complex and display a broad feature that blue-shifts with increasing cluster size before stabilizing into a very broad envelope stretching from 3000 to 3650 cm^{-1}. The sharpest features appear near 3700 cm^{-1}, the characteristic region of the free OH stretching vibration. Four distinct free OH band locations, labeled **a** to **d** in Fig. 34(B), are observed for $H^+(H_2O)_n$. The frequencies of these bands do not vary appreciably with increasing cluster size, but rather the dominant effect is a variation of the intensity distribution among these bands.

The outer two bands (**a** and **d**) in the free OH region fall in the typical locations observed for the symmetric and asymmetric stretching vibrations of a water molecule in a single H-bond accepting configuration (*i.e.*, where the two hydrogen atoms on the water molecule are free). As such, their presence likely reflects open structures where water molecules terminate chain-like motifs, and the disappearance of these bands for $n \geq 11$ then establishes that interconnected H-bonding networks are dominant for the larger clusters. The remaining two bands (**b** and **c**) persist throughout the size range $11 \leq n \leq 20$, with the intensity of feature **c** gradually being overtaken by that of feature **b** at $n = 12$.

An expanded view of the bands near the magic number at $n = 21$ is presented in Fig. 34(C). At $n = 21$, feature **c** drops abruptly and is barely evident, with the $n = 22$ cluster also dominated by a single feature (**b**). The emergence of a single feature indicates that these sizes contain only a single class of dangling OH groups. Peak **c** then reappears at $n = 23$ and persists in the larger clusters studied here. The unexpected similarity of the observed vibrational spectra for the $n = 21$ and $n = 22$ clusters suggests that they share a common structural motif, an observation clearly warranting a more thorough investigation beyond the scope of the present work.

To characterize how the local binding environments affect the energies of free OH bands, we carried out electronic structure calculations[233,234] based on the low energy isomers of the $n = 20$ and $n = 21$ clusters identified in earlier theoretical studies that used model potentials.[123] For each arrangement of O atoms[126] we chose the isomer previously reported to be the lowest in energy.[123] Figure 35 depicts the structures of the lowest-energy (0 K) isomers (20A and 21A) recovered for the $n = 20$ and 21 clusters. Both 20A and 21A are derived from the neutral dodecahedral cluster and have an H_2O monomer inside the cage and the proton on the surface, with an Eigen-like structure (shown in blue). The structures with an interior H_3O^+ were found to lie higher in energy (≈9 kcal/mol in our calculations). The present data, however, do not rule out a contribution of Castleman's high symmetry morphology to the ion ensemble.[9] We did not recover any low-energy Zundel-based structures derived from the dodecahedron.

Isomer 20A of the $H^+(H_2O)_{20}$ cluster is calculated to have a doublet in the free OH region with a similar splitting to that found experimentally (Fig. 34(C)). This doublet is

traced to the two types of free OH groups in 20A, those associated with AAD (A indicates acceptor and D, donor) monomers (seven in number) and that associated with a single AD water monomer (highlighted in green in Fig. 35(A)). The calculated spectrum for 21A, the lowest-energy isomer characterized for the $n = 21$ magic number species, displays a single line in the free OH region of the spectrum as indicated in Fig. 35(D), again consistent with the experimental spectrum. Interestingly, all of the free OH groups of 21A are associated with AAD monomers. Thus, our calculations offer a preliminary assignment of the observed peaks b and c (Fig. 34(C)) to water molecules in AAD and AD environments, respectively.

The fact that the prompt quenching of the free OH stretch doublet at $n = 21$ can be recovered in the context of the minimum energy (0 K) structures is surprising because the cluster ensemble prepared experimentally retains substantial internal energy. In the statistical limit, for example, one can crudely estimate that the $n = 21$ cluster must contain $\approx$1.5 eV of internal energy in order to photodissociate (on our time scale) upon excitation of a 3000 cm^{-1} photon.[235] To qualitatively evaluate how increasing internal energy effects the spectral evolution, we obtained the spectra of the $n = 20$ and 21 clusters using the Yale ion source operated close to evaporative ensemble conditions,[236] which yield the maximum internal energy constrained by evaporation kinetics. The resulting OH stretching spectra are displayed in the bottom traces in Fig. 35(C) and 35(D) for $n = 20$ and $n = 21$, respectively. Although there is a larger contribution from peak c in the spectrum from this warmer $n = 21$ cluster (Fig. 35(D), bottom trace), the dramatic fall-off in intensity relative to the $n = 20$ spectrum (Fig. 35(C), bottom trace) is still readily apparent. Thus, the discontinuity in the OH stretching spectra in going from $n = 20$ to $n = 21$ survives even though the clusters contain substantial internal energy and therefore likely reflects the average behavior of many structurally similar isomers contributing to the ensemble. This is particularly interesting in light of the earlier observation that the "magic" intensity at $n = 21$ is an entropic phenomenon.[237]

In the above analysis, we concentrated on the free OH bands because they provide an unambiguous diagnostic of water molecules with dangling OH groups, while the congested H-bonding region between 3000 and 3600 cm^{-1} is difficult to analyze in the context of structure. However, the OH stretch vibrations associated with the Eigen and Zundel ions

are calculated to appear in distinct regions and should allow experimental determination of the proton environment. In particular, our calculations predict intense lines near 2500 cm^{-1} for the former, and a transition below 2000 cm^{-1} for the latter. For isolated H_3O^+, the intense OH stretch vibration falls near 3500 cm^{-1}.[224] This is red-shifted to about 2800 cm^{-1} in $H^+(H_2O)_4$ (with an Eigen cation) and the band further shifts down to about 2500 cm^{-1} in the more extended H-bonded networks considered here. The calculated spectrum for structure 21A is presented in Fig. 36(A), illustrating the well-isolated location of the three OH stretching transitions of the surface-embedded H_3O^+ ion. The experimental (Georgia) spectrum of the $n = 21$ cluster is displayed in Fig. 36(B) and is dominated by the free OH transition and the local AAD motif assigned to this band is indicated in the inset. A relatively sharp band at around 3600 cm^{-1} emerges from the broad structure in the H-bonding region in the size range $18 \leq n \leq 24$. We can also understand this feature in the context of structure 21A, for which the calculations predict a sharp doublet in this frequency region arising from embedded DDA water molecules bound to three single-donor (AAD) water molecules.

Most puzzling, however, is that even though the calculations indicate that the observed $n = 21$ magic number and its neighbors exhibit Eigen-like structures, no photodissociation was detected below 3000 cm^{-1} for any of the larger ($n > 7$) clusters, with the relevant region highlighted in Fig. 36(A) for $H^+(H_2O)_{21}$. Possible explanations for this include suppression of the action spectroscopy signal due to inefficient photofragmentation at the lower excitation energy of the H_3O^+ band, unexpectedly strong anharmonicity in the hydrated H_3O^+ vibrations, and finally the possibility that the proton is actually associated with a Zundel-like structure, which would "shift" the absorption due to the proton below 2000 cm^{-1}. On the basis on what is known about the smaller protonated water clusters, it seems unlikely that anharmonicity could be large enough to displace transitions associated with the H_3O^+ core below 2000 cm^{-1}. If the kinetics of photofragmentation are suppressing the lower-energy H_3O^+ band, we should be able to improve the fragmentation efficiency either by increasing the initial internal energy or by attaching a more weakly bound "messenger" atom that can be eliminated upon excitation near 2500 cm^{-1}. We therefore also scanned the low-energy region with the warmer evaporative ensemble ion source (Yale), but have again failed to detect photodissociation in the critical energy range under these conditions. At the other extreme

of low internal energy, a preliminary study (done at Yale, with the source tuned far from the evaporative ensemble limit discussed earlier) using an Ar messenger atom was also not successful in observing any transitions near 2500 cm^{-1} for $H^+(H_2O)_{18}$ or $H^+(H_2O)_{21}$. Thus, these IR experiments are not able to detect the predicted signature of the Eigen moiety in the larger clusters. The experiments do not rule out Zundel structures, but cannot probe the crucial energy range required to establish its presence. Theory clearly favors Eigen-based structures, and these are indeed consistent with the spectroscopy in the free-OH region.[238] The unambiguous characterization of the proton environment therefore remains a challenge in this benchmark system. One complicating factor that needs to be addressed in future work is that the experimentally studied clusters are produced at finite temperature, while the theoretical methods employed so far do not take this into account. It may well be that dynamics resulting from the excess internal energy blurs the Eigen-Zundel structural distinction and its spectroscopic manifestations.

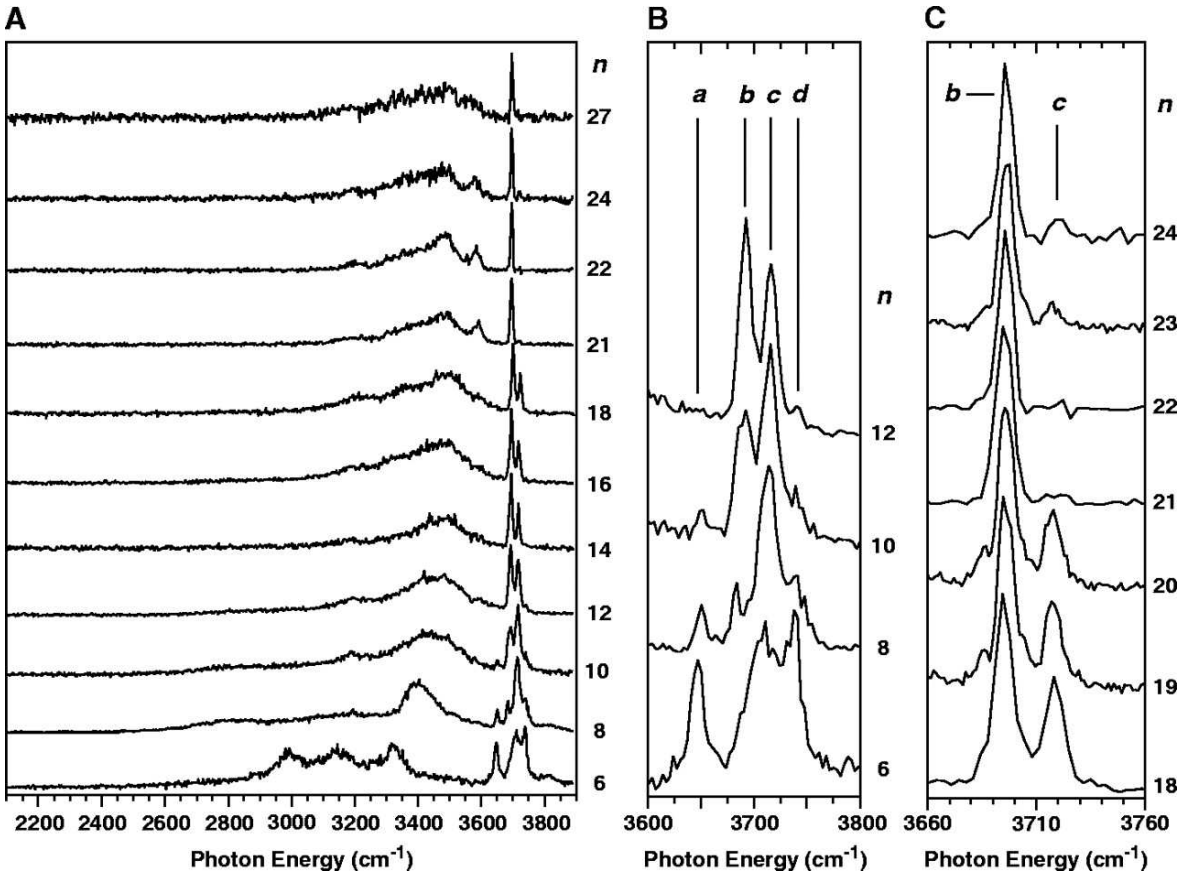

Figure 34: Overview of the vibrational predissociation spectra of $H^+(H_2O)_n$ ($6 \leq n \leq 27$) clusters prepared using the laser plasma source: (A) Survey of the 2100 - 3900 cm^{-1} energy range, (B) expanded view of free OH region for smaller clusters, and (C) expanded view of free OH region in the critical size range around $n = 21$.

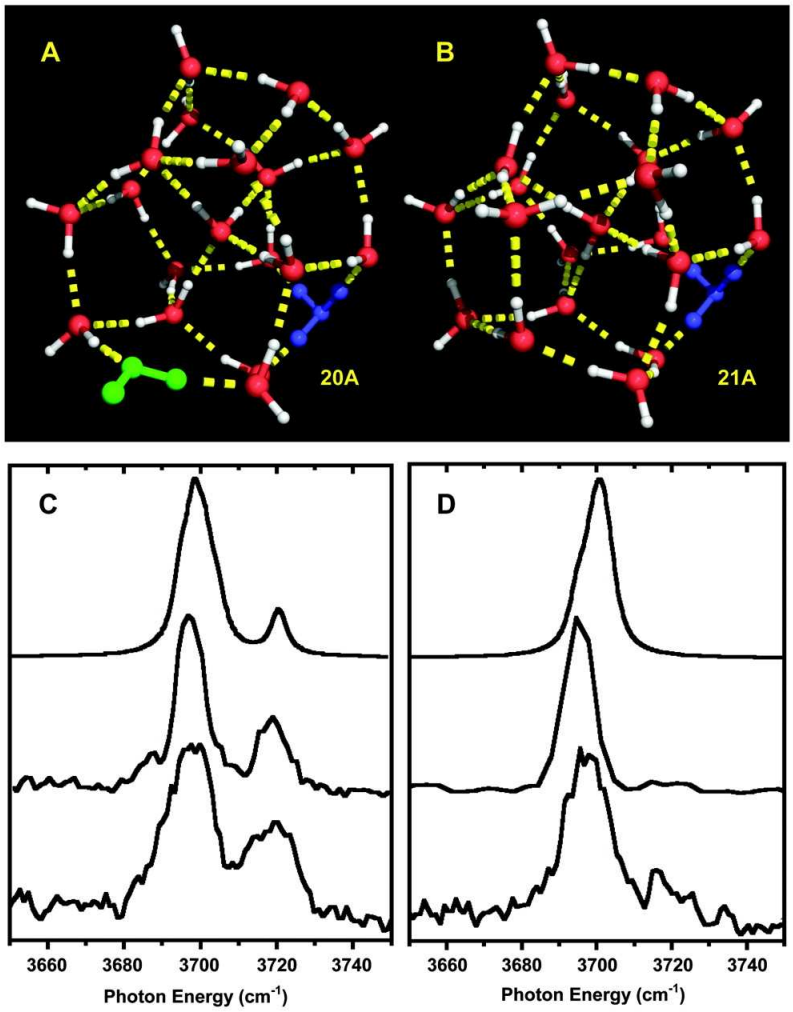

Figure 35: Calculated lowest-energy structures of $H^+(H_2O)_n$, $n = 20$ (A) and 21 (B). The hydronium cation is indicated in blue. For $H^+(H_2O)_{20}$ (A) the free OH responsible for the vibration absent in $H^+(H_2O)_{21}$ is indicated in green. Shown in (C) and (D) are calculated frequencies (top) and experimental spectra (middle - Georgia, bottom - Yale) of $H^+(H_2O)_n$, $n = 20$ (C) and 21 (D). The calculated spectra were obtained at the Becke3LYP/aug-cc-pVDZ† level of theory using the harmonic approximation and a scale factor of 0.962. Peaks were assigned Lorentzian shapes with widths of 5 cm^{-1}.

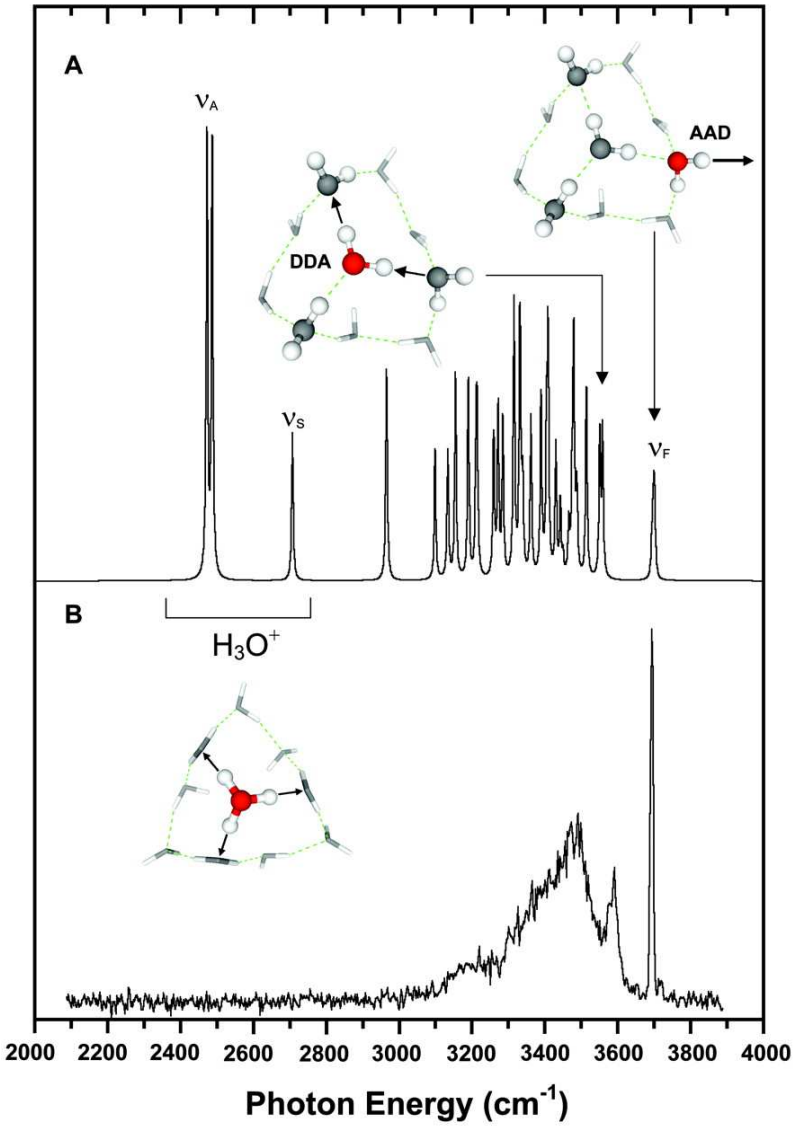

Figure 36: Calculated (A, 0.962 scaling) and experimental (B) vibrational spectra of $H^+(H_2O)_{21}$. The local environments and normal mode displacements of the vibrations (discussed in the text) are depicted (arrows). AAD and DDA denote H-bond acceptor-acceptor-donor and donor-donor-acceptor motifs and ν_A, ν_S, and ν_F refer to asymmetric, symmetric, and free OH stretches, respectively.

6.0 CONFORMATIONAL PREFERENCES OF JET-COOLED MELATONIN: PROBING *TRANS*- AND *CIS*-AMIDE REGIONS OF THE POTENTIAL ENERGY SURFACE

This work was published as

Florio; G. M.; Christie, R. A.; Jordan, K. D.; Zwier, T. S. *J. Am. Chem. Soc.*, **2002**, *124*, 10236

6.1 ABSTRACT

The hormone melatonin (N-acetyl-5-methoxytryptamine) is an indole derivative with a flexible peptide-like side chain attached at the C3 position. Using a combination of 2-color resonant two-photon ionization (2C-R2PI), laser-induced fluorescence excitation (LIF), resonant ion-dip infrared spectroscopy (RIDIRS), fluorescence-dip infrared spectroscopy (FDIRS), and UV-UV hole-burning spectroscopy, the conformational preferences of melatonin in a molecular beam have been determined. Three major *trans*-amide conformers and two minor *cis*-amide conformers have been identified in the R2PI spectrum and characterized with RIDIRS and FDIRS. Structural assignments are made using the infrared spectra in concert with density functional theory and localized MP2 calculations. Observation of *cis*-amide melatonin conformers in the molecular beam, despite the large energy gap (≈3 kcal/mol) between *trans*- and *cis*-amides, is striking because there are at least nine lower-energy *trans*-amide minima that are not detected. The implications of this observation for cooling and trapping conformational population in a supersonic expansion are discussed.

6.2 INTRODUCTION

Most molecules with biological relevance possess many flexible degrees of freedom, which produce a highly corrugated potential energy surface with a several conformational minima. Often, these molecules adopt only one or a small number of preferred conformations, even though many structural possibilities exist. Understanding why a molecule adopts a specific conformation involves understanding the balance of forces that exist within the molecule and between that molecule and its surroundings. This is particularly important in the case of small, biologically active molecules whose functions arise from their ability to dock in a receptor site and bind via noncovalent interactions such as hydrogen bonds. Ultimately, one would like to fully understand the conformational preferences and biological function of molecules in their native environments. Unfortunately, a molecular-scale understanding under physiological conditions is often hampered by the co-existence of several conformational isomers, the difficulty in assessing solvent effects, and the potential for rapid inter-conversion between conformational minima.

The study of such molecules in the gas phase removes solvent effects, thereby enabling the effects of intramolecular interactions to be assessed. The combination of double-resonance laser spectroscopy with supersonic expansion cooling provides a means of interrogating and structurally characterizing individual conformations of the flexible molecule, free from interference from other conformers and solvent effects.[239] One of the goals of experimental work on isolated, flexible biomolecules is to determine the preferred conformations and their relative conformer populations in order to benchmark calculations. In comparing experimental results with calculation, it is important to understand the relationship between the observed populations downstream in the expansion and the pre-nozzle Boltzmann distribution. In many cases, only conformations with relative energies within about 1 kcal/mol ($\approx kT_{nozzle}$) of the global minimum are observed in the expansion.[239,240,241,242,243,244,245] In cases involving only a single torsional degree of freedom, simple rules have been developed regarding the height of the barrier needed to trap population behind it during supersonic expansion ($\approx$400 cm^{-1}).[246] More recent studies on complex molecules with multiple degrees of conformational flexibility show that the barrier height needed to trap population in the expansion is closer

to 1000 cm^{-1}.[247,248] As the number of conformational degrees of freedom grows, the relative populations observed after supersonic expansion will depend on the characteristics of the potential energy surface (*i.e.*, the relative energies of minima, the important pathways for conformational isomerization, and the heights of barriers separating them) and on the dynamics of cooling on that surface.

Melatonin (N-acetyl-5-methoxytryptamine, shown in Figure 37) contains a single methyl-capped amide group. As in peptides, there is a strong energetic preference in melatonin for *trans*-amide over *cis*-amide conformations, with the former about 3 kcal/mol more stable than the latter. Despite this fact, we shall see that it is possible to trap a small amount of the pre-expansion population in the energetically unfavorable *cis*-amide branch, due to the large barrier to *trans*/*cis* isomerization (≈15-20 kcal/mol).[249,250,251]

In humans and other animal species, melatonin is a hormone that is primarily produced in the pineal glad, in small quantities in the retina, and in other tissues, with highest levels produced during the night.[252] Melatonin acts by specific binding to membrane receptors located in various regions of the brain and plays an important role as a transmitter of photoperiodic information, regulation of circadian rhythms and seasonal reproductive cycles, and mediation of other neuroendocrine and physiological processes.[253]

To date, the most sophisticated studies of the conformational preferences of melatonin have been experiments on the structure-affinity relationships (SARs) of melatonin and conformationally restricted melatonin analogues with natural membrance receptor tissues.[252] Several groups have used the SARs along with computational conformational searching to construct receptor[254,255] and pharmacophore models.[254,256] These studies indicate that both the methoxy and N-acetyl groups play an important role in the binding of melatonin with the native receptors, while the indole ring acts mainly as a spacer group, and the indole NH is not essential for activity.[252]

The work presented here addresses the conformational preferences of the isolated melatonin molecule, building on previous and on-going studies of jet-cooled conformationally flexible molecules such as neurotransmitters[242,257] amino acids[243,247] and amino acid derivatives – histamine,[248] tryptamine,[239,240,241] 3-indolepropionic acid[239,241] *N*-acetyl-tryptophan methyl amide,[258,259] *N*-acetyl-tryptophan ethyl ester[258,259,260] and *N*-acetyl-tryptophan

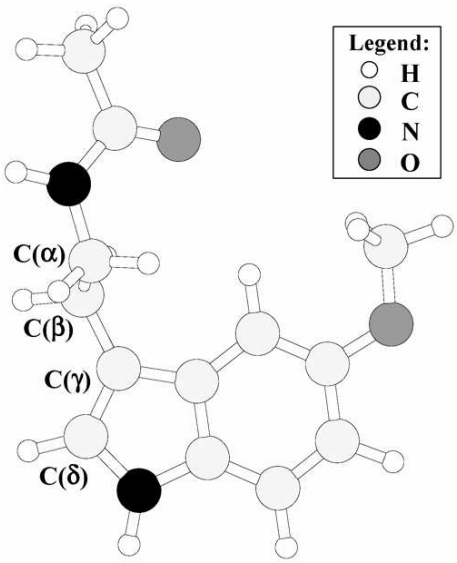

Figure 37: A picture of the melatonin molecule with the atom code and the important dihedral angles specified.

amide.[258,259,261]

6.3 METHODS

6.3.1 Experimental

The experimental methods used in this study have been recently reviewed.[239] Melatonin was obtained commercially (97% pure, Sigma) and used without further purification. Jet-cooled melatonin was prepared by flowing either pure helium or a 70% neon/30% helium mixture at a backing pressure of 2-3 bar over the solid sample, heated to 470 K. This mixture was pulsed into the vacuum chamber at 20 Hz, using a high-temperature pulsed valve (General, Series 9, 0.8 mm diam.). For interrogation by resonant two-photon ionization (R2PI), the expansion is skimmed ≈3 cm downstream from the nozzle orifice, and mass-analyzed by time-of-flight mass spectrometry. Alternatively, the molecule was studied by laser-induced

fluorescence following expansion in a free jet. In that case, the expansion is crossed with the UV excitation laser ≈4 mm downstream from the nozzle orifice, and the fluorescence is collected with an f:1 lens and imaged onto a UV-enhanced photomultiplier tube.

This work employs spectroscopic methods that are based on mass selected two-color R2PI spectroscopy and LIF excitation spectroscopy. To obtain the two-color R2PI (2C-R2PI) spectrum of jet-cooled MEL, the doubled output of a Nd:YAG-pumped dye laser operating at 20 Hz was used to probe the $S_1 \leftarrow S_0$ transition. Typical unfocused UV output is 200 μJ/pulse using Rhodamine 640 (oscillator) and Rhodamine 610 (amplifier), both in ethanol, Sulforhodamine 640 in methanol, or DCM in methanol. The third harmonic of a Nd:YAG laser (355 nm) was used for the ionization step, $D_0 \leftarrow S_1$. Typical 355 nm power was 1 mJ/pulse. The 355 nm laser was spatially and temporally overlapped with the UV laser. Cannington and Ham report the vertical ionization potential of melatonin as 7.7 eV, with an approximate value of 7.03 eV for the adiabatic ionization threshold.[262] Using the latter value (566972 cm^{-1}) as the ionization potential, 2C-R2PI through the melatonin $S_1 - S_0$ origin reaches 4000 cm^{-1} above the ionization threshold, compared to about 8500 cm^{-1} in the one-color R2PI scheme. 2C-R2PI was used instead of 1C-R2PI because unsaturated R2PI could be obtained with enhanced ionization efficiency and no detectable fragmentation.

In the case of flexible molecules, mass analysis cannot be used to separate the various conformational isomers present in the R2PI spectrum. The double-resonance technique of UV-UV hole-burning spectroscopy was used to obtain R2PI spectra of individual conformational isomers, free from interference from one another. The UV-UV holeburning spectra were obtained by fixing the hole-burning UV laser (10 Hz) on the origin transition of a particular conformer and tuning a time-delayed probe UV laser (20 Hz) through the R2PI spectrum, while monitoring the difference in ion current with and without the hole-burning laser present. All of the vibronic transitions that arise from the same ground state level as the hole-burned origin transition show up as depletions in the hole-burning spectrum.

Infrared spectra in the hydride-stretch region of individual melatonin conformers are obtained using a second double resonance technique, known as resonant ion-dip infrared spectroscopy (RIDIRS).[239] For such scans, the infrared output (2200-4000 cm^{-1}) of an injection seeded Nd:YAG-pumped optical parametric converter was spatially overlapped with the

two R2PI lasers, preceding them by 50-200 ns. 2C-R2PI, with λ_1 fixed to a given conformer $S_1 \leftarrow S_0$ origin, generates a constant ion signal in the melatonin monomer mass channel due to a single conformation of melatonin. The IR laser is operated at 10 Hz and tuned through the hydride-stretching region, depleting population out of the ground vibrational level whenever it is resonant with a vibration in the monomer of interest. Using active baseline subtraction, infrared transitions in the ground state monomer conformation are thus detected as depletions in the ion current.

For melatonin conformers with very small populations in the expansion, we utilized the fluorescence-based analog of RIDIRS (namely, fluorescence-dip infrared spectroscopy or FDIRS) to obtain infrared spectra. For FDIRS, a free-jet expansion of melatonin in helium was crossed 4 mm downstream by the counter-propagating IR and UV lasers. The laser-induced fluorescence of a specific conformer is monitored, while the IR source is tuned throughout the hydride-stretching region, just as in RIDIRS. While mass resolution is lost using the LIF-based method, the increase in signal-to-noise provided superior spectra of the smaller conformers using LIF detection.

6.3.2 Computational

In order to screen potential conformations adopted by flexible molecules such as melatonin, it is useful to run computationally inexpensive molecular mechanics conformational searches. Although the use of molecular mechanics methods such as AMBER, OPLS, MM3, and CHARMM to determine the relative conformational energies of gas phase molecules is not quantitatively accurate,[263] these methods are efficient for generating reasonable starting structures for quantum mechanical calculations. Conformational searching on melatonin was performed within MacroModel version 7.12[264] using the OPLS-AA force field[265] and the Monte Carlo search protocol. The OPLS-AA force field has been tested for accuracy in isolated molecule conformational energetics, and found to be among the best force fields for this purpose.[263] All dihedral angles of the melatonin flexible side chain and methoxy group were allowed to vary, with the exception of the methyl rotors, which were held in optimized geometries. An energy cutoff of 12 kcal/mol was used in the conformational searching.

The lowest energy structures (those within ≈5 kcal/mol of the lowest energy structure) generated by the OPLS-AA conformational search served as starting structures for full optimization via *ab initio* or density functional theory methods using the Gaussian 98 suite of programs.[96] The Hartree-Fock (HF) method was used for a second level screening, with the lowest 12 energy HF *trans*-amide minima, along with six *cis*-amide structures, being optimized using density functional theory calculations using the Becke3LYP functional.[94,266] Harmonic vibrational frequencies and infrared intensities were also computed for comparison with the experimental infrared spectra. All of these calculations employed the 6-31+G*(5d) basis set.[215]

Finally, localized MP2/aug-cc-pvtz(-f) single point energy calculations were performed on eight of the most relevant MEL structures (four *trans*/anti, three *trans*/syn and one *cis*/anti) in order to assess the accuracy of the relative energies obtained with the Becke3LYP method. The two main drawbacks of the B3LYP/6-31+G*(5d) procedure for predicting the relative energies of conformers of molecules such as melatonin are its failure to describe long-range dispersion interactions and its sizable basis set superposition errors (BSSE).[100] The adoption of the LMP2[203,267]/aug-cc-pVTZ(-f)[98,99,268] approach addresses both of these issues, properly describing dispersion interactions, while minimizing the effects of BSSE. The basis set employed is that of Dunning *et al.*[98,99,268] but with the f-functions and d-functions removed from the heavy elements and hydrogen, respectively. Both the adoption of the LMP2 procedure and the flexible aug-cc-pVTZ(-f) basis set are important for minimizing the BSSE. In the LMP2 method, the canonical HF orbitals are localized, and the exicitation space used to correlate the localized occupied orbitals is restricted to atomic functions centered upon these atoms. The LMP2 algorithm used in this study is the pseudospectral implementation of Murphy *et al.*[269] and included in the Jaguar[212] suite of programs. The Pipek-Mezey[270] procedure for orbital localization was used. LMP2 energies were calculated at the B3LYP/6-31+G*(5d) optimized geometries. Test calculations on the related tryptamine molecule show that the errors in the relative energies because of the use of the Becke3LYP geometries are quite small, and the same is expected to be true for melatonin.

6.4 RESULTS AND ANALYSIS

6.4.1 Calculated Structures, Energetics, and Vibrational Frequencies of the Conformers

While there have been previous computational studies focused on the conformational preferences of melatonin, these calculations were carried out using AM1,[271] MM2*,[254] and MM3[272] force fields or restricted HF calculations with minimal basis sets.[271,272] We therefore sought to carry out a more complete conformational search, and substantially improve the quantitative predictions of relative conformational energy using the procedure outlined in Section 6.3.2. By combining force field searching with higher-level quantum mechanical calculations, we have generated a more reliable set of structures with predictions for the infrared spectra that can aid our spectral assignments.

The OPLS-AA conformational searching yielded 204 unique minima within 12 kcal/mol of the global minimum. These conformers fall into one of four families: *trans*/anti, *trans*/syn, *cis*/anti, and *cis*/syn, where *trans* (*cis*) refers to the orientation of the amide group and anti (syn) refers to the orientation of the methoxy group with respect to the indole NH. Approximately 40 of the lowest energy OPLS-AA structures were further optimized using the HF/6-31+G*(5d) method. The energy ordering of the HF optimized structures differs significantly from the OPLS-AA calculations. Becke3LYP/6-31+G*(5d) geometry optimizations and harmonic frequency calculations were performed on the twelve lowest energy structures obtained from the HF calculations (all *trans*-amides), along with six higher energy *cis*-amide structures. The energy ordering of the DFT optimized MEL conformers, both zero-point energy uncorrected and corrected, agrees well with the HF calculations. Finally, single point LMP2/aug-cc-pVTZ(-f) calculations were performed on eight of the lowest-energy conformers, including four *trans*/anti, three *trans*/syn, and one *cis*/anti structures. Table 8 summarizes the relative energies obtained using both the DFT and LMP2 methods. While the LMP2 method predicts the same ordering of the four lowest energy minima as the DFT method, the relative energies of the various families changes significantly between DFT and LMP2. In the table, the zero-point energy corrections for the LMP2 results use the DFT

harmonic frequencies.

Table 8: Relative energies of a selection of MEL conformational minima[a]

MEL Conformer	ΔE (B3LYP)	ΔE (B3LYP+ZPE)	ΔE (LMP2)	ΔE (LMP2+ZPE)
Anti(*trans*-out)/anti	0.00[b]	0.00[c]	0.00[d]	0.00[c]
Gpy(*trans*-in)/anti	0.28	0.30	0.56	0.58
Gph(*trans*-in)/anti	0.68	0.69	0.71	0.72
Anti(*trans*-in)/anti	0.88	0.77	1.62	1.50
Gpy(*trans*-in)/syn	1.14	1.12	3.02	3.00
Gph(*trans*-in)/syn	1.54	1.54	3.07	3.08
Anti(*trans*-out)/syn	2.04	1.94	3.56	3.46
Gph(*cis*-in)/anti	2.70	2.92	2.36	2.58

[a] The energies are calculated via Becke3LYP/6-31+G*(5d) full geometry optimzations and single-point localized MP2/aug-cc-pVTZ(-f) calculations. Zero-point energy contributions are determined at the Becke3LYP/6-31+G*(5d) level of theory. [b] The absolute energy of anti(*trans*-out)/anti is -480106.3125 kcal/mol (DFT). [c] The zero-point energy of anti(*trans*-out)/anti is 172.2339 kcal/mol (DFT). [d] The absolute energy of anti(*trans*-out)/anti is -478956.1835 kcal/mol (LMP2).

Select DFT optimized structures, are shown pictorially in Figure 38. In all calculated structures, the oxygen and carbon atoms of the methoxy group lie in the plane of the indole ring. The lowest energy conformations of MEL have the methoxy group pointed anti with respect to the indole NH, regardless of the orientation of the amide group and the position of the backbone. Not surprisingly, the lowest energy DFT calculated conformations of MEL have the amide group in a *trans* configuration. Almost all of the low energy structures of MEL have the C(α)-C(β) bond nearly perpendicular to the ring. The *N*-acetyl group then takes up various positions relative to the indole ring: anti, gauche towards the pyrrole ring (Gpy) and gauche towards the phenyl ring (Gph) of indole. This is the same nomenclature used to denote the position of the ethylamine or propionic acid side chains in TRA

and IPA.[239,241] In addition, MEL has flexibility associated with the orientation of the *N*-acetyl and methoxy groups. Thus, the four lowest energy structures are denoted Anti(*trans*-out)/anti, Gpy(*trans*-in)/anti, Gph(*trans*-in)/anti, and Anti(*trans*-in)/anti, where the notation is defined as: backbone position(amide NH orientation)/methoxy position and "in" or "out" refers to whether the amide NH is pointed in towards or out away from the indole ring.

The structures in Figure 38 depict nine of the lowest energy *trans*-amide structures, and the lowest four *cis*-amide structures with their energies relative to the global minimum determined by the DFT method. The zero-point corrected LMP2 energies are also listed for select conformations in parentheses. According to the DFT calculations, the four most stable structures are all within 1 kcal/mol of one another. The Anti(*trans*-out)/anti structure is the global minimum, and the Gpy(*trans*-in)/anti and Gph(*trans*-in)/anti structures are slightly higher in energy at 0.30 and 0.69 kcal/mol, respectively. The next highest energy structure, at 0.77 kcal/mol, is a second Anti *N*-acetyl structure labeled Anti(*trans*-in)/anti, which differs from the global minimum primarily by rotation about the C(α)-N(H) bond. The LMP2/aug-cc-pVTZ(-f) single point energy calculations retain the Anti(*trans*-out)/anti structure as the global minimum, but raises the energy of the other *trans*/anti minima relative to it. The relative energy of the fourth minimum (Anti(*trans*-out)/anti is affected most noticeably by the level of theory, being pushed up from 0.77 to 1.50 kcal/mol, including zero-point energy correction). Thus, the LMP2 calculations predict that three structures, Anti(*trans*-out)/anti, Gpy(*trans*-in)/anti, and Gph(*trans*-in)/anti, are at least 0.8 kcal/mol more stable than all other structures.

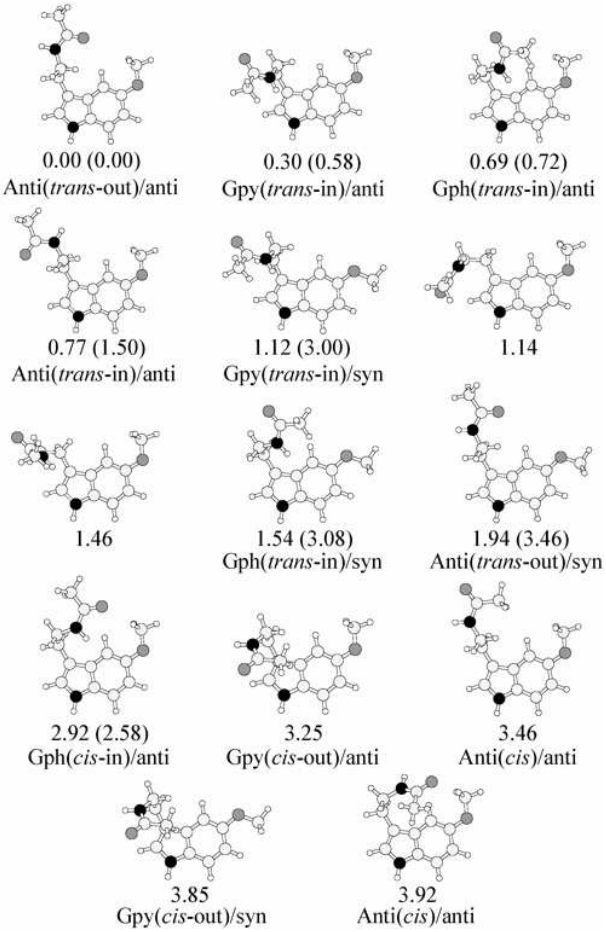

Figure 38: A summary of selected conformational minima of MEL obtained via Becke3LYP/6-31+G*(5d) calculations. The DFT zero-point corrected relative energies in kcal/mol are displayed beneath each structure, and where available, the localized MP2/aug-cc-pVTZ(-f) relative energies are shown in parentheses. Minima are observed for the four families of MEL with the energy ordering: *trans*-amide/anti-methoxy $<$ *trans*/syn $<$ *cis*/anti $<$ *cis*/syn.

The energetically-preferred position for the methoxy group is "anti" over "syn". In the DFT calculations, the Gpy(*trans*-in)/syn, Gph(*trans*-in)/syn, and Anti(*trans*-out)/syn minima are located 1.12, 1.54, and 2.04 kcal/mol, respectively, above the global minimum. This preference for anti over syn methoxy structures is predicted to be even greater by the LMP2 calculations. The energies of the Gpy(*trans*-in)/syn, Gph(*trans*-in)/syn, and Anti(*trans*-out)/syn minima are raised to 3.00, 3.08, and 3.46 kcal/mol, respectively, above the global minimum. This would seem to indicate that dispersion interactions are more significant in the MEL conformations with a syn-oriented methoxy group.

The lowest energy *cis*-amide MEL conformers are also approximately 3 kcal/mol higher in energy than the Anti(*trans*-out)/anti global minimum. The lowest energy *cis*-amide MEL conformer is the Gph(*cis*)/anti structure at 2.92 (2.58) kcal/mol above the global minimum using DFT (LMP2) (Figure 38). The calculated *cis*-amide MEL minima show a greater variability in the degree of rotation about the C(α)-C(β) bond than the corresponding *trans*-amide minima.

Hydride stretch harmonic vibrational frequencies and infrared intensities calculated at the DFT Becke3LYYP/6-31+G*(5d) level of theory are summarized for the relevant conformers in the Supporting Information (Section 6.8). A scale factor of 0.96 has been used to align the calculated frequency of the indole NH to its experimental value. Unfortunately, this same scale factor over-estimates the CH stretch frequencies by about 60 cm^{-1}.

The frequency of the amide NH stretch fundamental is most sensitive to the MEL conformation, suggesting that this band will play a key role in the comparison between experiment and theory in making conformational assignments. For *trans*-amide MEL conformers, the amide NH stretch appears either as a free NH stretch ($\approx$3485 cm^{-1}) or slightly shifted down in frequency due to a weak interaction of the NH group with the π cloud of indole. By comparison, all *cis*-amide MEL conformers have an amide NH stretch that is lowered in frequency by about 50 cm^{-1} relative to their *trans*-amide counterparts. This shift can serve as a marker to distinguish *cis*-amide from *trans*-amide structures. The hydride stretch vibrational frequencies also encompass a range of CH stretch vibrations due to aromatic (3000-3100 cm^{-1}), CH_2, and CH_3 groups. The strong methoxy symmetric stretch vibration ($\approx$2900 cm^{-1}) shows little dependence on the methoxy orientation (syn or anti), and thus is

not anticipated to be an effective means of discriminating between these structures.

6.4.2 LIF, R2PI, and UV-UV Hole-Burning Spectroscopy

A portion of the LIF excitation spectrum of MEL in a helium expansion is shown in Figure 39. The LIF spectrum is dominated by two transitions labeled A (32614 cm^{-1}) and B (32621 cm^{-1}). Several less intense transitions are observed both to the red and blue of these transitions. The transition labeled C occurs at 32795 cm^{-1} with an intensity 17% that of transition A. Two even weaker transitions labeled D (32483 cm^{-1}) and E (32432 cm^{-1}) have intensities only 5% and 0.8% of A. The transition just to the blue of E, which is marked with an asterik, is due to a MEL-(H_2O) complex, as determined by mass analysis and infrared spectroscopy, and will be discussed in a forthcoming paper.[273]

We anticipate that the LIF spectrum of Figure 39 contains overlapping spectra due to different conformational isomers of MEL. To determine the number of conformations present, and identify their ultraviolet spectra, UV-UV hole-burning spectroscopy is used, here based on 2C-R2PI detection. Figure 40(a) presents the 2C-R2PI spectrum (λ_{ion} = 355 nm) for comparison with the hole-burning spectra of Figure 40(b) and 40(c), all recorded in the MEL monomer mass channel (m/z=232). These spectra were taken with a 70% neon / 30% helium expansion mixture. The hole-burning laser was fixed on the transitions labeled A in recording Figure 40(b) and transition B to record Figure 40(c). The hole-burning spectra prove that A and B are two distinct MEL species, and therefore represent different conformational isomers. All of the transitions to the blue of A and B belong to one of these two conformers, with the exception of transition C which will be discussed separately below.

The hole-burning spectra of Figure 40(b) and 40(c) provide the ultraviolet spectra of the two dominant MEL conformers, free from interference from one another. These two conformers are hereafter denoted A and B, respectively, in keeping with their origin transition labels. It should be noted that the R2PI spectra for MEL A (Figure 40(b)) and MEL B (Figure 40(c)) bear a close resemblance to one other and are characteristic of the ultraviolet spectra of indole[274] and other indole derivatives.[240,274] Both MEL conformers undergo only small changes in geometry upon electronic excitation, with intense origin transitions and

relatively weak vibronic structure. For both MEL A and B, a progression in a low-frequency vibrational mode (33 cm^{-1} for A, 41 cm^{-1} in B) is observed, built off the origin transitions and off a vibronic band at +500 cm^{-1}. The nature of this low-frequency vibration is one that involves motion of the MEL sidechain with respect to the indole ring. A likely candidate is the butterfly motion at ≈30 cm^{-1} in the DFT calculations. The greater intensity of this low-frequency progression in A than B suggests a stronger interaction of the side-chain with the π cloud in the former over the latter.

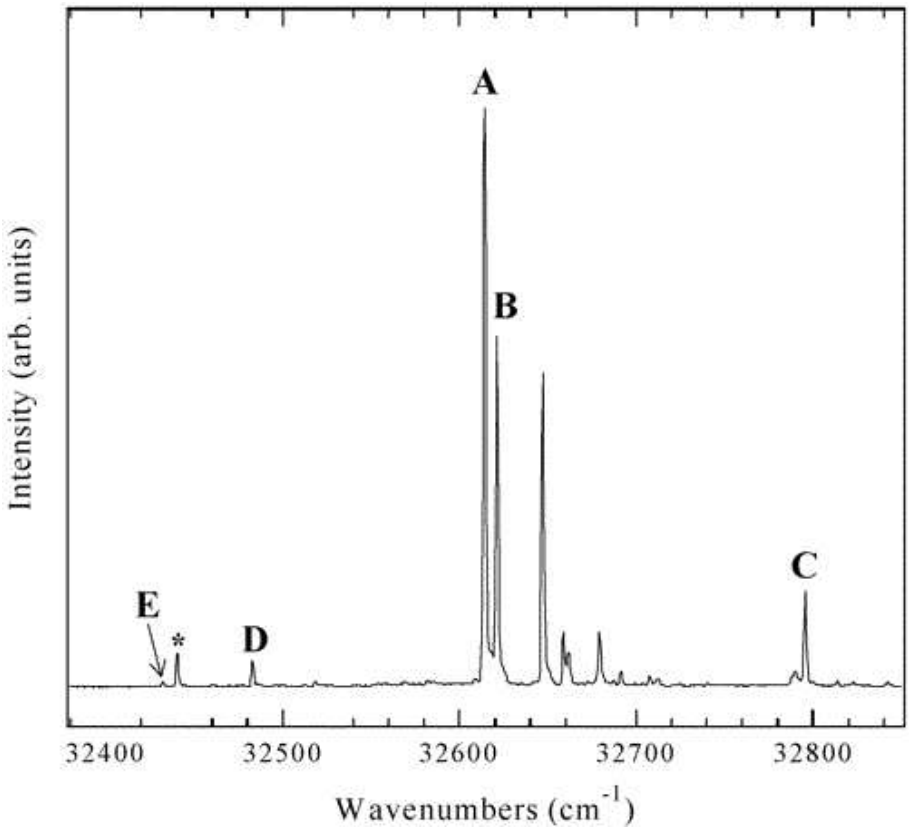

Figure 39: A portion of the LIF spectrum of MEL. The letters indicate the five distinct melatonin conformer $S_1 - S_0$ origin transitions. The asterisk designates a MEL-W_1 cluster observed in the LIF spectrum at 32441 cm^{-1}.

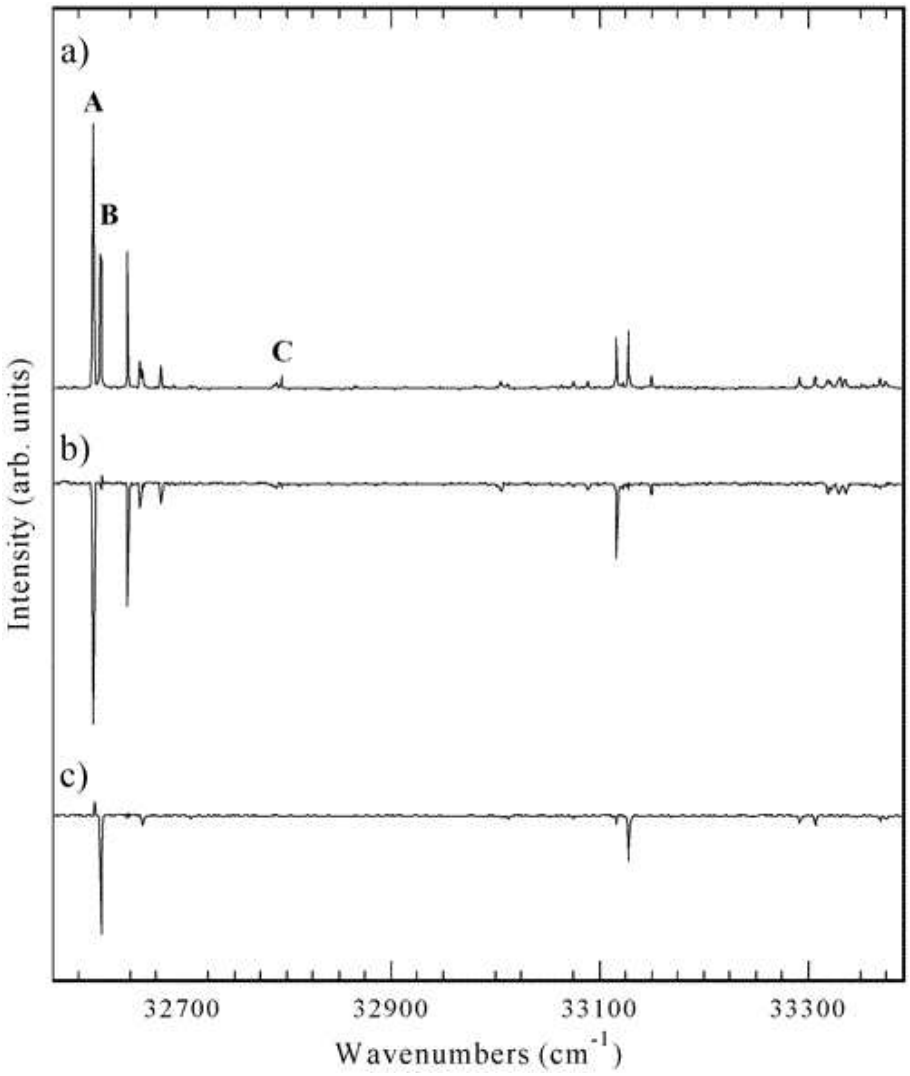

Figure 40: (a) 2C-R2PI spectrum taken in the MEL$^+$ mass channel ($m/z = 232$) and (b,c) UV-UV holeburning spectroscopy with the holeburning laser fixed on the $S_1 - S_0$ origin transition of (b) MEL A (32614 cm^{-1}) and (c) MEL B (32621 cm^{-1}). The hole-burning spectra indicate that MEL A and B are distinct origin transitions arising from different MEL conformations. All of the vibronic structure observed in the R2PI spectrum is cleanly divided between the A and B conformers, with the exception of the transition labeled C (32795 cm^{-1}). See text for further discussion.

On the basis on a comparison with the DFT calculations, the vibronic transitions at approximately 500 cm^{-1} above both A and B are assigned to a vibration involving a significant amount of C-C/C=C vibration involving expansion of the indole ring, consistent with the expected change in the ring induced by the $\pi \rightarrow \pi^*$ transition. Not surprisingly, this +500 cm^{-1} vibration is observed in the R2PI spectra of most other indole derivatives. The frequencies of the vibronic transitions for each conformer and their[240,274,275,276,277] relative intensities are summarized in Table 9.

As mentioned earlier, the only transition in the portion of the R2PI spectrum shown in Figure 40(a) that is not a vibronic band of MEL A or B is the transition labeled C at 32795 cm^{-1}. Because this transition does not burn out with either MEL A or B, we know that the carrier of this transition is a species distinct from A and B. The infrared spectrum recorded when monitoring transition C (Section 6.4.3) will provide further proof that this transition is due to a third MEL conformation. The intensity of the MEL C origin (relative to A and B) in the LIF spectrum taken in a helium expansion (Figure 39) is considerably greater than its intensity in the 2C-R2PI spectrum taken in a 70% neon/30% helium expansion (Figure 40(a)). An LIF spectrum using 70% neon/30% helium confirms that it is the difference in expansion conditions, rather than any difference in detection efficiency in LIF versus R2PI, that is responsible for the observed intensity change. The sensitivity of the population of conformer C to the presence of neon in the expansion indicates that the barrier to isomerization out of minimum C must be small enough that collisional cooling can effect this population.[247,248] On the basis of the relative intensities of A, B, and C under both expansion conditions, it appears that the population from conformer C is being funneled into conformer A in the neon expansion.

The UV-UV hole-burning spectra of MEL D and E (Figure 39) were not obtained because the transitions are weak enough that it was difficult to see the vibronic structure amongst the much more intense bands due to A and B. Coincidentally, the MEL D transition occurs at the same frequency as a vibronic transition of a MEL–$(water)_1$ cluster appearing in the MEL–$(water)_1^+$ mass channel.[273] To determine that the carrier of this band in the MEL^+ mass channel was a monomer species and not a water cluster, a 1C-R2PI spectrum was recorded in the absence of water flow in the expansion (not shown). The MEL D and E

transitions are retained in the absence of water flow at the same intensity relative to A and B, while the transition in the MEL–$(water)_1^+$ mass channel disappears. Most importantly, the FDIR spectra of the D and E transitions reveal that they are in fact additional monomer species, unique from each other and from the MEL A, B, and C conformers. The MEL D and E transitions are not affected by expansion conditions.

It is concluded that the transitions labeled A–E are the $S_1 \leftarrow S_0$ origin transitions of five distinct MEL conformers. R2PI spectra extending 600 cm^{-1} below the E transition reveal no further monomer structure. The MEL A, B, C, D, and E origin transitions at 32614, 32621, 32795, 32483, and 32432 cm^{-1} respectively, are $\pi \rightarrow \pi^*$ excitations of the indole moiety, and are shifted 2400-2800 cm^{-1} to the red of the indole origin at 35239 cm^{-1}.[274] For comparison, the $S_1 \leftarrow S_0$ origin transitions of 3-methylindole, tryptamine conformer A, and 5-methoxyindole are shifted to the red of the indole origin by 362 cm^{-1},[274] 320 cm^{-1},[240] and 2103 cm^{-1},[274] respectively. Thus, it is the presence of the methoxy group at the C5 position that is responsible for the dramatic stabilization of the excited electronic state of melatonin with respect to that of indole.

As Figure 39 shows clearly, the $S_1 \leftarrow S_0$ origin transitions of the five conformers naturally break up into the A/B pair near 32600 cm^{-1}, the D/E pair near 32400 cm^{-1}, and the lone transition C near 32800 cm^{-1}. This natural grouping of transition frequencies suggests a similar structural grouping in the five conformers. However, the electronic frequency shift is a measure of the separation between S_0 and S_1 states, and is difficult to correlate with distinct structural features of the individual conformations, which perturb the π cloud of indole via both through-space and through-bond interactions. Instead, we turn next to the infrared spectra, which bear a more direct correlation with conformation, and are (potentially) sensitive to other aspects of the conformations of MEL.

6.4.3 RIDIR and FDIR Spectroscopy

The RIDIR spectra of the MEL A and B conformers and the FDIR spectra of the MEL C-E conformers in the CH and NH stretching region (2800-3800 cm^{-1}) are shown in Figure 41(a)-(e), respectively. Due to the weaker intensity of transitions C-E, their FDIR spectra were

recorded with about a factor of two higher infrared intensity, and hence are somewhat more saturated than the RIDIR spectra of A and B. The infrared spectra of the MEL conformers exhibit two NH stretch fundamentals in the 3400-3600 cm^{-1} region, and a collection of aromatic, alkyl and methyl CH stretch fundamentals spread over the region from 2800-3100 cm^{-1}. In all five conformers, the indole NH stretch appears between 3522 and 3526 cm^{-1}, very close to its frequency in the indole monomer (3525 cm^{-1}).[276] Not surprisingly, this fundamental is not sensitive to the conformations of the side-chains.

On the other hand, the amide NH stretch fundamental is much more sensitive to conformational change, varying between 3420 and 3495 cm^{-1}. A first classification is obvious from Figure 41: while the amide NH stretch fundamentals of conformers A, B, and C appear at above 3480 cm^{-1} (3480, 3495, and 3482 cm^{-1}, respectively), those due to D and E are shifted below 3440 cm^{-1} (specifically, at 3420 and 3435 cm^{-1}, respectively). Furthermore, the set of three high-frequency conformers break up further into a set of two (A and C at 3480 and 3482 cm^{-1}) and conformer B, with its highest frequency amide NH stretch at 3495 cm^{-1}.

The CH stretch region of the spectra is complicated by the sheer number of fundamentals due to aromatic CH, alkyl CH_2, methyl groups, and the potential for Fermi resonance with overtones of lower-frequency vibrations. The CH stretch region of each conformer is unique, and can potentially serve as a confirming diagnostic of the molecular conformation. In particular, the CH stretches of the MEL A, B, and C share common features that are distinct from those of MEL D and E. This suggests that the MEL A, B, and C conformers have a structural similarity not shared by MEL D and E.

Table 9: Summary of UV transition assignments in the 2C-R2PI and LIF spectroscopy of MEL

species	frequency (cm^{-1})	relative frequency (cm^{-1})[a]	normalized intensity[b]
conformer A	32614	0	100.0
	32647	33	51.1
	32659	45	10.4
	32679	65	8.3
	32790	176	1.8
	32795	181	1.8
	33006	392	3.1
	33089	475	2.7
	33116	502	31.0
	33149	535	4.7
	33318	704	4.3
	33322	708	2.9
	33329	715	4.1
	33336	722	4.1
	33369	755	2.2
conformer B	32621	0	49.2
	32662	41	4.2
	32708	87	1.0
	33005	384	0.7
	33012	391	1.2
	33075	454	1.1
	33116	495	3.5
	33127	506	18.9
	33292	671	2.9
	33307	686	3.8
	33369	748	2.3
	33375	754	1.2
conformer C	32795	0	5.0
conformer D	32483	0	3.7
conformer E	32432	0	0.5

[a] Frequency shifts of vibronic bands of a given conformer are relative its origin transition.

[b] Peak intensities are relative to the conformer A origin, which is arbitrarily set to 100.

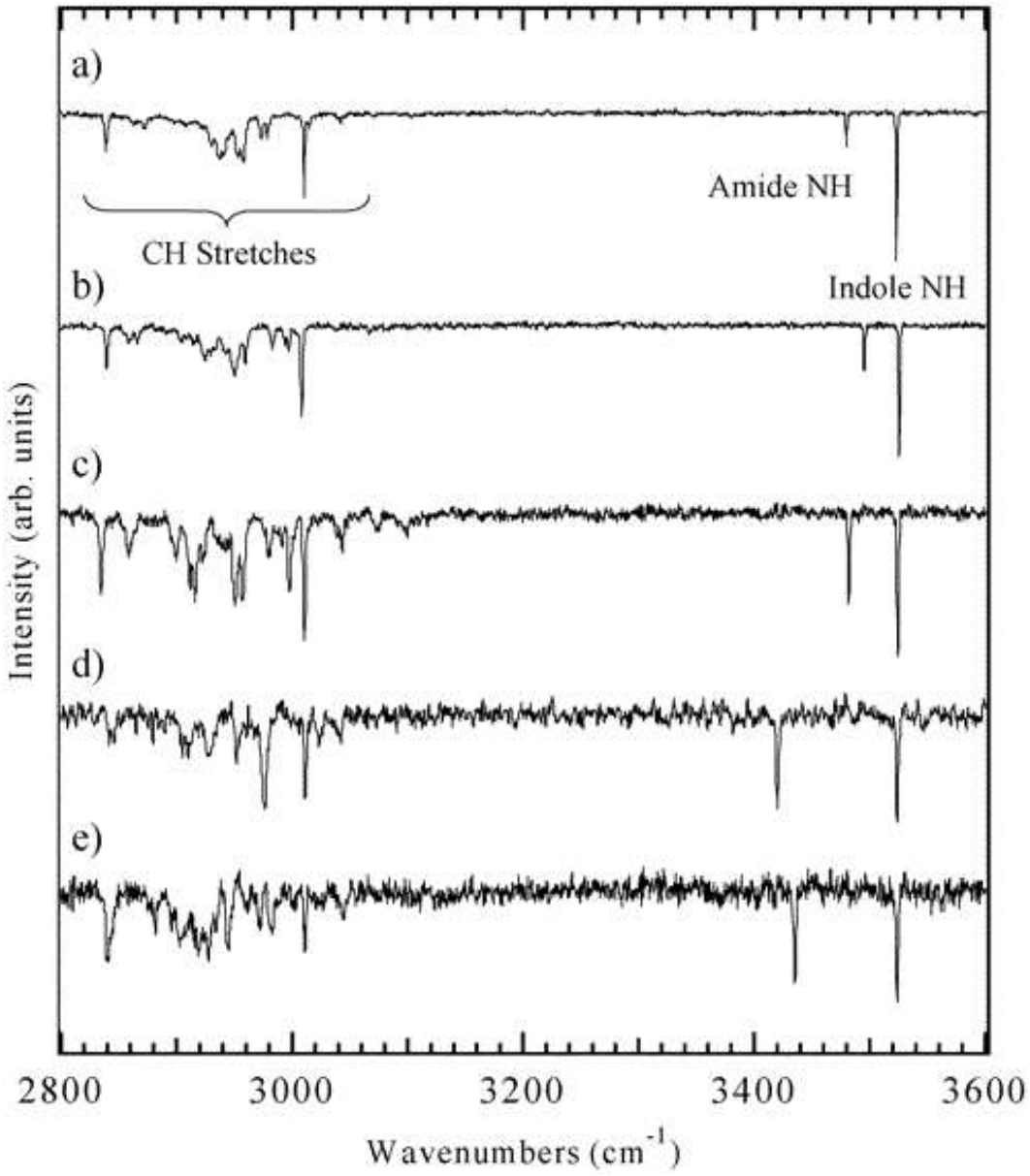

Figure 41: Overview of the RIDIR and FDIR spectra of the five MEL conformers taken with the UV laser fixed to the origin transitions of (a) MEL A, (b) MEL B, (c) MEL C, (d) MEL D, and (e) MEL E. The position of the indole NH stretch, the amide NH stretch, and the CH stretch region are specified.

In an attempt to understand the complex CH stretching region of the MEL conformers, we have obtained the FDIR spectrum of 5-methoxyindole (5-MOI), which removes the transitions due to the side-chain in the 3-position in MEL, thereby highlighting the CH stretch transitions due to the 5-methoxy methyl group and the indole ring. The FDIR spectrum of 5-methoxyindole is shown in Figure 42(b), and compared both with the Becke3LYP/6-31+G*(5d) calculated harmonic infrared spectrum of 5-MOI (Figure 42(c)) and the MEL conformer A RIDIR spectrum (Figure 42(a)). Based on a comparison of the FDIR (Figure 42(b)) and calculated (Figure 42(c)) spectra of 5-MOI, all of the experimental transitions can be assigned. The methoxy methyl group produces three CH stretch fundamentals spread over the 2800–3000 cm^{-1} region. The symmetric methyl stretch occurs at 2837 cm^{-1}, while the two "antisymmetric" methyl CH stretch bands appear as a Fermi dyad at 2912/2902 and at 2952 cm^{-1}. The experimental spectrum contains only two other CH stretch bands (3010 cm^{-1} and 3042 cm^{-1}), ascribable to the aromatic CH stretch fundamentals of the indole ring. The likely correspondence with the calculated aromatic fundamentals is made by the dashed lines in Figure 42. The weak bands above 3050 cm^{-1} are not clearly observed in the experimental spectra.

The FDIR spectrum of 5-MOI can then be used to identify the corresponding methoxy CH stretch bands in the MEL conformers, since the frequencies of the aromatic and methoxy CH stretches in the MEL A spectrum (Figure 42(a)) are essentially unaltered from their values in 5-MOI (Figure 42(b)). Analogous bands are apparent in MEL B-E as well. In particular, the dominant aromatic CH stretch band at 3010 cm^{-1} and the methoxy symmetric stretch at ≈2840 cm^{-1} are easily identifiable in all spectra. Only small changes are observed in this latter band (occurring at 2839 in MEL A, 2839 in MEL B, 2834 in MEL C, 2841 in MEL D, and 2839 cm^{-1} in MEL E), suggesting that all five conformers share the same methoxy group orientation as observed in 5-MOI. However, the calculations show almost no change in the methoxy methyl CH stretch frequencies with methoxy group orientation, making this vibration uninformative regarding a syn/anti assignment. By process of elimination, the remaining bands in the MEL A spectrum thus arise from the $CH_2(\alpha)$, $CH_2(\beta)$ and N-acetyl methyl CH stretching modes of the side chain.

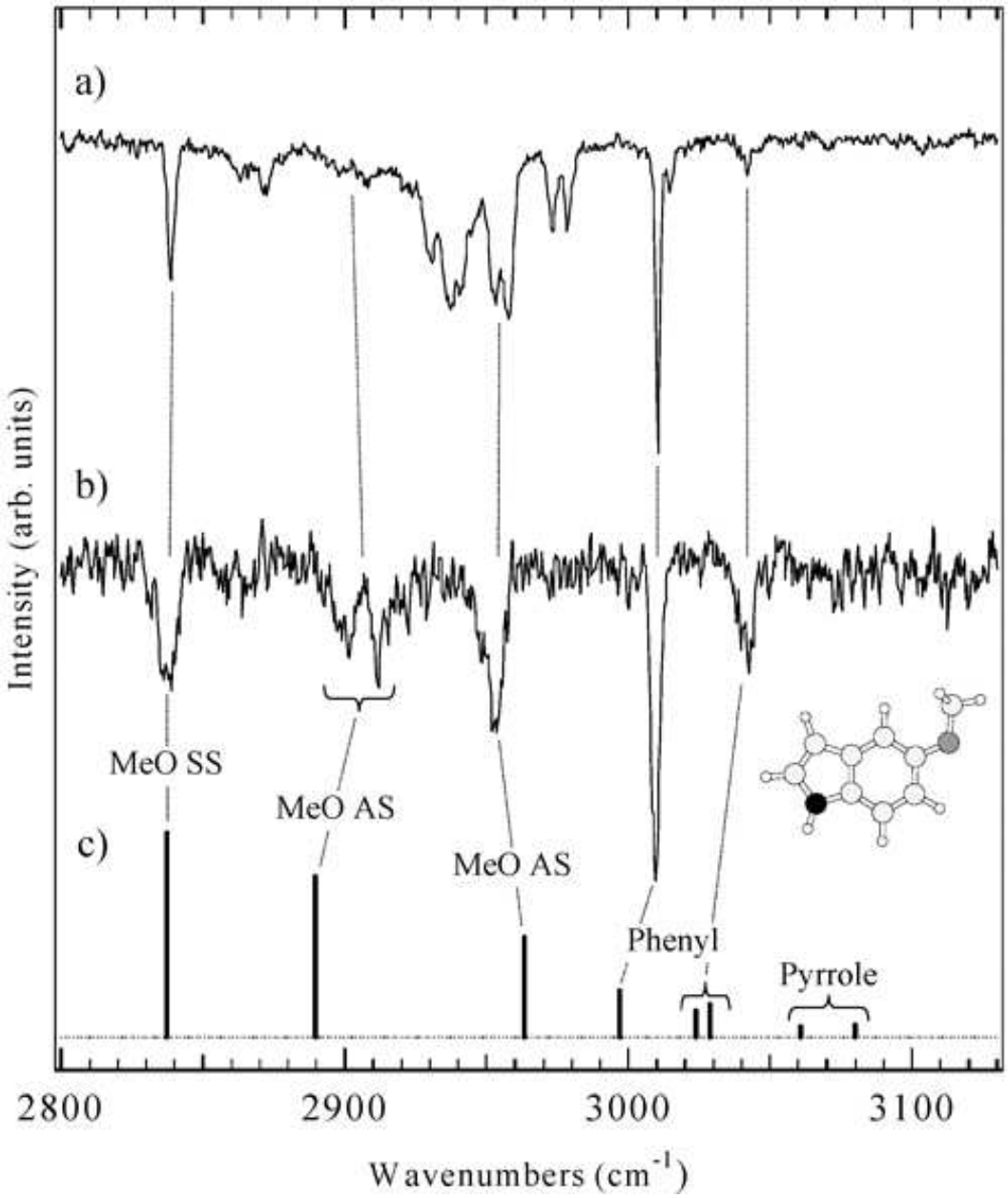

Figure 42: A comparison of the IR spectra of (a) MEL A, (b)5-methoxyindole, and (c) the Becke3LYP/6-31+G*(d) calculated harmonic IR spectrum of 5-methoxyindole in the CH stretching region. The frequencies in the calculated spectrum (c) have been scaled by 0.94, thereby aligning the calculated and experimental methoxy CH_3 symmetric stretching mode of 5-methoxyindole. Assignments of CH stretches between 5-methoxyindole and MEL A are shown by the dashed lines. See text for discussion.

A comparison of the MEL CH stretch spectra with the $CH_2(\alpha)$ and $CH_2(\beta)$ transitions in tryptamine suggests that much of the observed transitions unaccounted for by the methoxy and indole CH stretches is due to the $CH_2(\alpha,\beta)$ groups.

6.4.4 Conformational Assignments

As the results of Section 6.4.2 and 6.4.3 indicate, the frequency of the amide NH stretch fundamental is anticipated to provide the clearest basis of distinction between the various MEL conformations, guided by the calculations. Figure 43 presents the harmonic infrared frequencies and infrared intensities of the lowest three *trans*-amide conformers (Figure 43(a)–(c)) and lowest two *cis*-amide conformers (Figure 43(d), (e)) of MEL, calculated at the DFT Becke3LYP/6-31+G*(5d) level of theory. As noted previously, the calculations predict that the *cis*-amide NH stretch fundamentals are characteristically lower in frequency than their *trans*-amide counterparts by about 40-50 cm^{-1}. No other structural change (e.g., syn/anti methoxy or gauche/anti N-acetyl) is capable of producing a change in the amide NH stretch of this magnitude. Table 10 compares the experimental and calculated shift of the amide NH stretch frequency from the indole NH stretch for the lowest three *trans*-amide and lowest two *cis*-amide conformers. This shift serves as an excellent indicator of the orientation of the amide group, *trans* versus *cis*, and leads us to assign the dominant MEL A, B, and C conformers to *trans*-amide conformers with shifts of 43, 31, and 42 cm^{-1}, respectively, while the minor population D and E conformers are both *cis*-amides with shifts of 103 and 88 cm^{-1}. These assignments are consistent with previous work by Simons and co-workers on N-phenylformamide[245] and N-benzylformamide,[242] where the *cis*/*trans* amide NH stretch frequencies are 3441/3463 cm^{-1} and 3443/3478 cm^{-1}, respectively.

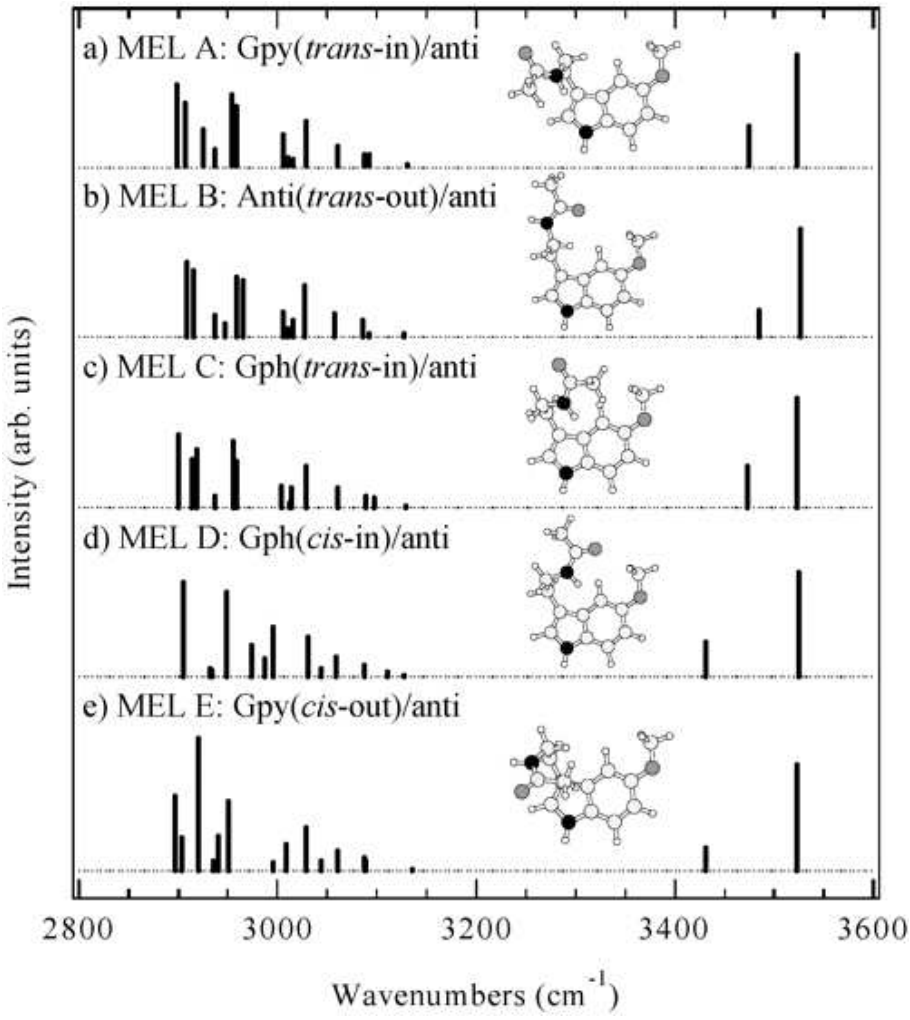

Figure 43: (a)-(e): Calculated harmonic vibrational frequencies and infrared intensities for the CH and NH stretch vibrations of the Gpy(*trans*-in)/anti, Anti(*trans*-out)/anti, Gph(*trans*-in)/anti, Gph(*cis*-in)/anti, and Gpy(*cis*-out)/anti conformers of MEL. The structures of these conformers are shown as insets. All calculated frequencies have been scaled by 0.96 in order to bring the calculated indole NH stretch frequency into coincidence with its experimental value (3525 cm^{-1}).

Having assigned MEL A, B, and C as *trans*-amide conformers, it remains to assign the three to specific *trans*-amide conformational isomers. Fortunately, the frequency shifts in Table 10 also provide a basis for distinguishing between the various positions of the *N*-acetyl group relative to the indole ring, gauche versus anti. Of the three *trans*-amide conformers, MEL B has a shift of only 31 cm^{-1}, while that for MEL A and C are about 10 cm^{-1} greater, at 42 and 43 cm^{-1}, respectively. As Table 10 indicates, the calculations predict that the gauche *N*-acetyl positions (Gpy and Gph) have amide NH stretch fundamentals that are about 10 cm^{-1} lower than the corresponding anti position. The amide NH stretch fundamental is shifted down in the gauche position by virtue of a weak interaction of the amide NH with the π cloud of indole, which is not possible in the extended anti *N*-acetyl position. Thus, the comparison between calculation and experiment indicate that two of the *trans*-amide conformers are gauche N-acetyl conformers (A and C), and one (conformer B) is an anti N-acetyl conformer.

Table 10: Experimental and Becke3LYP/6-31+G*(d) calculated frequency shifts between the position of the indole NH stretch and the amide NH stretch for each MEL conformation.

conformer	assignment	experimental frequency shift (cm^{-1})	calculated frequency shift (cm^{-1})
MEL A	Gpy(*trans*-in)/anti	43	50
MEL B	Anti(*trans*-out)/anti	31	41
MEL C	Gph(*trans*-in)/anti	42	51
MEL D	Gph(*cis*-in)/anti	103	94
MEL E	Gpy(*cis*-out)/anti	88	91

Further support for the assignment of conformer A to a gauche conformer and conformer B to an anti conformer comes from the R2PI spectra of conformers A and B. MEL A has substantially greater Franck-Condon intensity in the low-frequency vibrations than conformer B, consistent with its assignment to a gauche conformer, in which the *N*-acetyl group interacts with the indole π cloud, and can respond to electronic excitation of the indole ring

to change its position, thereby turning on Franck-Condon progressions in the low-frequency rocking vibrations of the side-chain.

On the basis of energetics (Table 8), the three lowest-energy conformers (Anti(*trans*-out)/anti, Gpy(*trans*-in)/anti, and Gph(*trans*-in)/anti) have relative energies of 0.00, 0.58, and 0.72 kcal/mol, while the next highest *trans*-amide structure (Anti(*trans*-in)/anti) is at 1.50 kcal/mol, almost 0.8 kcal/mol higher than the other three. As a result, we anticipate based on the calculations that these lowest three *trans*-amide structures are those observed experimentally. Furthermore, two of these three lowest-energy *trans*-amide conformers are gauche *N*-acetyl conformers, while the third is an anti structure, consistent with the deductions based on the amide NH stretch frequencies. We therefore assign conformer B to the Anti(*trans*-out)/anti structure, and conformers A and C to the lowest energy Gpy and Gph structures.

The present experimental results cannot easily distinguish which gauche conformer (A or C) to assign to which gauche position, Gpy or Gph. On the basis of energetics, we tentatively assign conformer A to the Gpy(*trans*-in)/anti structure which is 0.58 kcal/mol above the global minimum, and conformer C to the Gph(*trans*-in)/anti structure, with a slightly higher energy of 0.72 kcal/mol. However, the calculations cannot be depended on to faithfully reproduce this small an energy difference, and future work may come to the opposite conclusion. Rotational analysis should be capable of distinguishing between these possibilities.

On the basis of the greater intensity of the transitions of MEL A relative to B, it is probable that conformer A is lower in energy than conformer B. However, the assignment of conformer A is to a gauche conformer which is higher in energy by 0.58 kcal/mol than the Anti(*trans*-out)/anti global minimum assigned to B. This may be some indication that the calculations are not yet fully converged, even at the LMP2/aug-cc-pVDZ(-f) level of theory. Full geometry optimizations (rather than the present single-point calculations) may lead to a further shuffling of the energies of the low-energy conformers of MEL. Equally important, as Godfrey *et al.*[248] have recently pointed out, differences in free energy between the conformers may skew the populations from that based upon energetics alone. Furthermore, the cooling of population out of higher energy conformaters into A and B may also effect the observed

populations downstream in the expansion.

There is an alternative assignment for the three *trans*-amide conformers A-C that deserves brief mention. We stated previously that conformers A and B have $S_1 \leftarrow S_0$ origins very close to one another, while conformer C is shifted about 200 cm^{-1} to the blue. Since the 5-methoxy group is responsible for much of the large frequency shift of the $S_1 \leftarrow S_0$ origin of MEL from that of bare indole, one might wonder whether conformers A and B could be anti-methoxy structures, while conformer C is a syn-methoxy structure with a smaller electronic frequency shift.

A previous LIF study by Sulkes and co-workers[274] led these authors to conclude that there was only one conformer of 5-MOI present in the expansion. However, 5-hydroxyindole has two $S_1 \leftarrow S_0$ origins due to syn and anti hydroxy isomers, separated from one another by 228 cm^{-1}.[277,278] Furthermore, no hole-burning studies were conducted in the previous work on 5-MOI to address the question of conformational isomers directly. As a result, we carried out LIF and UV-UV hole-burning spectroscopy on 5-MOI. The results, shown in Figure 44(a) and 44(b), prove that all the transitions observed in the LIF spectrum are due to a single conformer of 5-MOI. Calculations we performed at the Becke3LYP/6-31+G*(5d) level of theory indicate that the barrier to isomerization from syn to anti 5-MOI is 1.4 kcal/mol while the syn 5-MOI minimum is about 1 kcal/mol above the anti minimum. On the basis of these calculations, it seems likely that in the preexpansion population in syn-orientated 5-MOI can be converted into the anti conformer via collision with the buffer gas in the expansion. By analogy, unless the side-chain in the 3-position of MEL effects either the relative energies of the syn and anti methoxy isomers or the height of the isomerization barrier separating them substantially, it seems unlikely that conformer C of MEL can be attributed to a syn-methoxy isomer.

We have yet to assign conformers D and E to specific *cis*-amide structures. Based on the relative intensities of the transitions in the R2PI and LIF spectra, conformer D is anticipated to be lower in energy than conformer E. Furthermore, our experience with the *trans*-amide conformers would suggest that the lower frequency of the amide NH stretch for conformer D (3420 cm^{-1}) relative to conformer E (3435 cm^{-1}) might result from the former structure incorporating the amide NH group in a weak π H-bond not experienced by conformer E.

We have not done an exhaustive search for *cis*-amide structures. However, the lowest energy *cis*-amide structures found in our work are the Gph(*cis*)/anti and Gpy(*cis*)/anti structures with energies 2.92 and 3.27 kcal/mol above the global minimum, at the DFT B3LYP/6-31+G*(5d) level of theory (Table 8, Figure 38). Furthermore, the Gph(*cis*-in)/anti structure points the amide NH group in toward the indole π cloud, while the Gpy(*cis*-out)/anti orients the NH group away from indole. This suggests that conformer D be assigned to the Gph(*cis*-in)/anti structure, and conformer E to the Gpy(*cis*-out)/anti conformer. However, the calculated frequencies of the amide NH stretch fundamentals (Table 10) do not show the expected frequency ordering, and no firm assignment to specific *cis*-amide structures can be made based on the present data.

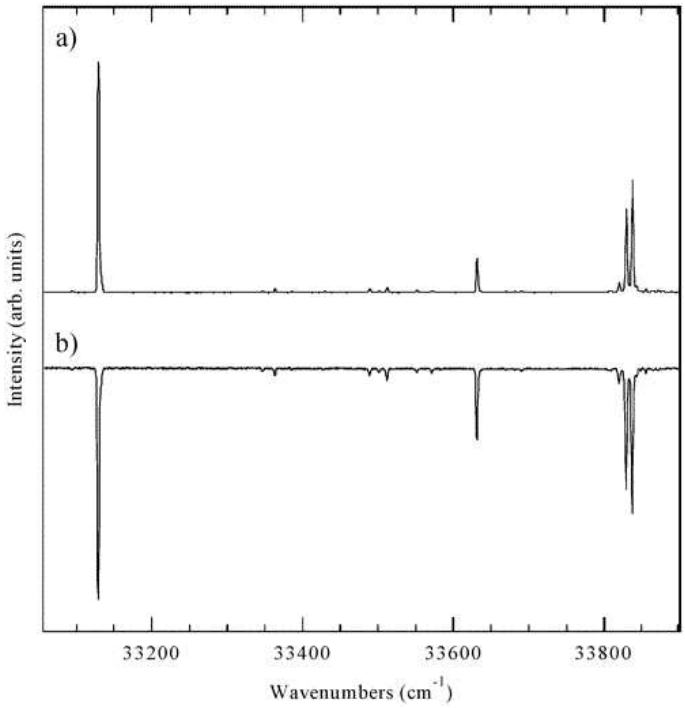

Figure 44: (a) LIF scan of 5-methoxyindole in the region of the $S_1 \leftarrow S_0$ origin. (b) UV-UV hole-burning scan taken with hole-burn laser tuned to the origin at 33130 cm-1. The hole-burn scan demonstrates that all structure in the LIF spectrum arises from a single ground state level, assignable to the anti-methoxy conformer based on energetics.

6.5 DISCUSSION

The conformational preferences of melatonin: In this work, the methods of mass-selected resonant two-photon ionization, laser-induced fluorescence excitation, UV-UV hole-burning, resonant ion-dip infrared spectroscopy, and fluorescence-dip infrared spectroscopy have been used to determine the conformational preferences of melatonin in the gas phase. By studying the isolated molecule under jet-cooled conditions, well-resolved ultraviolet transitions due to five conformations are observed. The double resonance methods of UV-UV hole-burning, RIDIR spectroscopy, and FDIR spectroscopy have been used to acquire the UV and IR spectra of each of the five conformations free from interference from the others present in the expansion.

Not unexpectedly, the three dominant conformations are all *trans*-amide structures. As in other tryptophan analogs, the preferred orientation of the ethyl side chain is nominally perpendicular to the indole ring, leading to three distinct positions for the N-acetyl group: gauche on the pyrrole side of indole, gauche on the phenyl side, and anti. Our assignment of conformers A–C show that population is present in all three positions, with some preference for the Gpy and anti structures over the Gph structure. The low-energy gauche structures point the amide NH group in toward the π cloud, consistent with formation of a weak π H-bond. This is borne out by the spectroscopy of the Gpy and Gph conformers, in which the amide NH is shifted down in frequency by 15 and 13 cm^{-1}, respectively, relative to the anti structure. According to the calculations, the methoxy group in the 5-position is in plane, and prefers an orientation anti with respect to the indole NH, rather than syn. Unfortunately, the calculations show little difference in the methoxy methyl CH stretch frequencies in the two orientations, and we are left to surmise an anti structure for the methoxy group based largely on the calculated energetic preference for this orientation. However, the calculated energy difference between corresponding syn and anti-methoxy structures is rather large ($\approx$3 kcal/mol at the LMP2/aug-cc-pVTZ(-f) level of theory), leaving little doubt that the methoxy group prefers the anti structure, as in the related 5-MOI molecule.

The fourth and fifth conformers, whose $S_1 \leftarrow S_0$ origin intensities are only 5 and 1% that of conformer A, have been assigned to *cis*-amide structures. The present data provides

no firm assignment for which *cis*-amide structures are observed, leaving largely open the question of how the preference for gauche and anti *N*-acetyl groups is changed by the amide conformation. What is clear, however, is that these *cis*-amide structures are observed when several others with energies similar to or below them in energy are not. It is this issue to which we now turn.

Conformational cooling and population trapping in the supersonic expansion: In most previous studies of conformationally flexible biomolecules, the primary criterion used to decide which conformational minima were potential candidates for experimental observation was the energy of the minima relative to one another. In comparing two conformers, the one with lower energy was always preferred. However, the detection of two *cis*-amide conformers in melatonin presents a startling exception to this rule, raising the following questions:

(1) Why are the *cis*-amide conformers observed despite their high energy?

(2) Why are several *trans*-amide or syn-methoxy conformers not observed, despite the fact that they are lower in energy than the *cis* conformers?

One potential solution to both these questions is simply to call into question whether the calculations correctly reproduce the experimental energies of the conformers. Issues of intramolecular basis set superposition error, the lack of dispersion in the DFT calculations, and the use of a modest-sized basis set all point to the need for higher level calculations to address these issues. This motivated our single-point localized MP2/aug-cc-pVTZ(-f) energy calculations which did show considerable differences from the DFT results, and highlight the need for full optimizations at the LMP2 level of theory to further address this point. However, while the LMP2 calculations did change the relative energies of the conformers, they did not change the qualitative picture and general energy ordering of the structures, making it unlikely that arguments based on the relative energies of the conformational minima will answer the above questions satisfactorily.

Instead, the populations of the conformers of MEL observed downstream in the expansion reflect both the energies of the minima and the barriers to isomerization separating them. Thus, the presence of two *cis*-amide conformers can only be accounted for once the large barrier to *trans*/*cis* isomerization about the amide bond is recognized. The pre-expansion

conformer population is in full thermal equilibrium. One anticipates, then, a *cis*-amide Boltzmann population prior to expansion that reflects this energy difference. Using an energy difference of 3 kcal/mol and a temperature of 200 °C, the total population in MEL D should be ≈4% that of the *trans*-amide global minimum. Assuming that population alone determines the relative intensities of the LIF and R2PI origin transitions, this estimate agrees well with the experimental value of ≈5%, determined from the LIF intensity ratio of MEL D to MEL A. Thus, it appears that the Boltzmann population in *cis*-amide conformations is effectively trapped there by the large barrier to *trans*/*cis* isomerization, and cannot be removed by the cooling collisions in the expansion. In retrospect, this is not surprising in light of the magnitude of the barrier to *trans*/*cis* isomerization (15-20 kcal/mol).[249,250,251] The short time-scale of the expansion and the small collision energies available in the expansion cannot overcome such a barrier during the cooling process.

At the same time, the expansion is remarkably effective in collapsing all the *cis*-amide population into two minima and the *trans* population into three minima. One cannot allow the presence of a *cis* population of a few percent of the global minimum without recognizing that the many other *trans* minima calculated to be lower in energy than these *cis* conformers must have had measurable populations in them prior to expansion. The syn-methoxy counterparts of conformers A-C are cases in point. These conformers have similar energies to the *cis*-amide conformers, yet they are not observed, while the *cis*-amide conformers D and E are readily detected. Given the excellent signal-to-noise ratio of the LIF scan of Figure 39 and the R2PI scan of Figure 40, conformational origins of about 0.1% of A or B should have been observable. Our calculations on 5-MOI indicate that there is a barrier of isomerization out of syn methoxy conformer of about 1.4 kcal/mol, which is small enough that collisions may be able to remove this population by expansion. By analogy, we anticipate the barrier out of syn-methoxy MEL conformers to be small as well.

There are several previous studies of conformationally flexible molecules that have addressed the magnitudes of the barriers needed to trap population in local minima.[239,240,241,246,247,248] In molecules that contain two conformational minima and a single isomerization coordinate, the rule-of-thumb that developed from these studies is that a barrier of at least 400 cm^{-1} (1.1 kcal/mol) is needed to trap population in a neon ex-

pansion. In tryptamine and 3-indole-propionic acid, which have two low-energy flexible coordinates, this rule appears to have been followed in large measure.[239,240,241] More recent studies[247,248,257] on molecules with several flexible coordinates have shown that the barrier required to trap population in the expansion is increased to about 1000 cm^{-1} (2.9 kcal/mol) in these larger molecules because of the larger internal energies available to the molecules prior to expansion and the higher preexpansion temperatures used. As a result, Godfrey *et al.* have pointed out[247,248] a proper account of the expansion-cooled populations must consider not only the conformational minima but also the connectivity of the potential energy landscape (e.g., which minima are connected to which), the magnitudes of the barriers separating the minima, the Boltzmann populations prior to expansion (which are determined by the free energies of the conformations), and the dynamics of cooling on the potential energy landscape.

In MEL, we have direct experimental evidence that the population of MEL C is smaller in a 70% neon/30% helium expansion than in a pure helium expansion, demonstrating the importance of cooling collisions in effecting the downstream population of this conformer. However, transition state structures, isomerization pathways, and their energies are not yet available for MEL, especially at a level of theory where they can be considered reliable. Such an exploration of the potential energy landscape even for MEL, is a rather daunting task. Based on experience with other molecules, it seems likely that the magnitudes of the conformational barriers separating the low-energy minima of MEL will be similar to that in tryptamine of 3-indole propionic acid, where barriers of 500 to 1000 cm^{-1} were typical. Clearly, a more thorough knowledge of the potential energy landscape for MEL will be required before a firm answer regarding conformational cooling in the expansion can be given.

The relevance of gas-phase conformations to melatonin binding at the receptor site: One of the motivations for studying the conformational preferences of melatonin in the gas phase is that it may help us understand its preferred conformations in aqueous solution and when bound to membrane receptor sites in the brain. Clearly, melatonin may have different conformational preferences in these environments. Yet, it is precisely this type of comparison that is not typically available. With it, it may be possible to assess the effects

of aqueous solvent and of the receptor site itself, as further data on the conformations of melatonin in these environments becomes available.

In the gas phase, the Anti(*trans*-out)/anti and Gpy(*trans*-in)/anti structures are the two most stable conformations (Figure 38, Table 8), but all three positions for the *N*-acetyl group are relatively close in energy to one another. According to the calculations, almost all the low-energy structures of MEL have the C(α)-C(β) bond nearly perpendicular to the indole ring. However, there are a few low-energy conformations that place this bond in the plane of the indole ring. The lowest of these is only 1.14 kcal/mol above the global minimum (Figure 38). Similarly, the methoxy group prefers an in-plane structure that points the methyl group toward, rather than away from, the *N*-acetyl ethylamine side chain. The energy difference here is about 3 kcal/mol. The difference in energy between conformational families involving the amide bond, *cis* versus *trans*-amides, is also about 3 kcal/mol. Energy differences of this scale are about five times kT at room temperature (0.6 kcal/mol). Such *cis* structures seem not to be seriously considered in biological models of melatonin binding.[252,254,255,256,257,279]

It would seem that the conformational preferences of melatonin are played out on rather modest energy scales that are comparable to, or somewhat greater than kT. It is likely that energy differences of this magnitude can be overcome readily by hydrogen bonds with water in aqueous solution. It would be interesting to determine the conformational preferences of melatonin in aqueous solution for comparison with the present gas phase results. To probe the beginnings of such solvation, we are currently studying the spectroscopy of the water-containing clusters of melatonin.[273]

Without a strong, intrinsic structural preference, it seems likely that nature may be using these small energy differences and modest energy barriers (< 5 kcal/mol) to enable melatonin to deform into the desired shape for binding as it enters into or moves within the receptor binding pocket. It also may facilitate the binding of melatonin to different types of receptor sites in carrying out its multiple biological functions. In fact, as we have suggested previously,[280] the formation of a hydrogen bond to the binding site could provide a source of energy for the rearrangement into the desired configuration.

Even the preference for *trans* over *cis*-amide conformations is not of a size so large as to make it alone the reason that *cis*-amide structures are not likely candidates for binding

to the receptor. One could imagine circumstances under which better binding by the *cis* conformation to the receptor could compensate for the 3 kcal/mol energy difference in a receptor of the right design. Instead, it seems more likely to us that the preference for *trans* over *cis* structures derives in some measure from the large barrier to *trans*/*cis* isomerization of the amide bond. This large barrier could prevent isomerization on the encounter time-scale in the binding pocket. This would give an element of kinetic control to the binding.

6.6 CONCLUSIONS

The present investigation has probed the conformational preferences of melatonin by studying the infrared and ultraviolet spectra of individual conformations in the isolated molecule under jet-cooled conditions. The detection of two *cis*-amide conformations, and the conspicuous absence of many conformations of equal or lower energy, shows clearly that small populations can be trapped behind large barriers on the time-scale of collisional cooling in the expansion. The five conformers show unique amide NH stretch fundamentals. The *trans*-amide anti conformer (MEL B), in which the amide NH is free, occurs at 3495 cm^{-1}. The *trans*-amide gauche structures (MEL A and C) point the amide NH in toward the indole π cloud, producing 15 and 13 cm^{-1} red-shifts to 3480 and 3482 cm^{-1}. The *cis*-amide structures have amide NH stretch fundamentals shifted to lower frequency than their *trans* amide counterparts, providing a definitive signature for their presence. The gauche pyrrole MEL E structure has the amide NH away from the ring and results in a free NH stretch frequency of 3435 cm^{-1}. Finally, the *cis*-amide gauche phenyl structure (MEL D) NH fundamental points the amide NH in toward the indole π cloud, producing a 15 cm^{-1} red-shift to 3420 cm^{-1}.

While these studies have probed the preferred conformational minima of melatonin, they also point out the need for both experimental and theoretical studies that probe the barriers to and preferred pathways for conformational change in molecules of this size. It is also hoped that the present data can serve as a testing ground for higher-level *ab initio* calculations and improved molecular mechanics force fields.

6.7 ACKNOWLEDGEMENTS

T.S.Z. and G.M.F. gratefully acknowledge the National Science Foundation Experimental Physical Chemistry Program for their support of this work under a two-year creativity extension to grant CHE9728636. G.M.F. thanks the Purdue Research Foundation for a graduate student fellowship. The authors acknowledge the assistance of Dr. Asier Longarte, Brian Dian, and Dana Holcomb.

6.8 SUPPORTING INFORMATION AVAILABLE

Table listing Becke3LYP/6-31+G*(5d) calculated infrared frequencies and intensities of select MEL conformations (PDF). This material is available free of charge via the internet at http://pubs.acs.org.

BIBLIOGRAPHY

[1] Haberland, H., Ed.; *Clusters of Atoms and Molecules;* volume 1 Springer-Verlag: Berlin, 1994.

[2] Haberland, H., Ed.; *Clusters of Atoms and Molecules;* volume 2 Springer-Verlag: Berlin, 1994.

[3] Jellinek, J., Ed.; *Theory of Atomic and Molecular Clusters, with a Glimpse at Experiments;* Springer-Verlag: New York, 1999.

[4] Guet, C.; Hobza, P.; Spiegelman, F.; David, F., Eds.; *Atomic Clusters and Nanoparticles;* Springer-Verlag: New York, 2001.

[5] Johnston, R. L. *Atomic and Molecular Clusters;* Taylor and Francis: New York, 2002.

[6] Duley, W. W. *Astrophys. J.* **1999,** *L57,* 471.

[7] Wayne, R. P. *Chemistry of Atmospheres;* Oxford University Press U.K.: Oxford, 1991.

[8] Schindler, T.; Berg, C.; Niedner-Schattenburg, G.; Bondybey, V. *J. Chem. Phys.* **1996,** *94,* 3998.

[9] Wei, S.; Shi, Z.; Castleman Jr., A. W. *J. Chem. Phys.* **1991,** *94,* 3268.

[10] Berry, R. S.; Beck, T. L.; Davis, H. L.; Jellinek, J. Solid-liquid phase behavior in microclusters. In *Evolution of Size Effects in Chemical Dynamics, Adv. Chem. Phys.*, Vol. 70, Part 2; Prigogine, I.; Rice, S. A., Eds.; John Wiley: New York, 1988.

[11] Wales, D. J. *Energy Landscapes: Applications to Clusters, Biomolecules and Glasses;* Cambridge University Press: Cambridge, 2003.

[12] Drexler, K. M. *Nanosystems: molecular machinery, manufacturing and computation;* McGraw Hill: New York, 1992.

[13] Westesen, K. *Colloid. Polym. Sci.* **2000,** *278,* 608.

[14] Berry, R. S.; Haberland, H. Clusters of Atoms and Molecules. In , Vol. 1; Haberland, H., Ed.; Springer-Verlag: Berlin, 1994.

[15] Turton, R. *The Quantum Dot: A Journey into the Future of Microelectronics;* Oxford University Press: New York, 1995.

[16] Liu, K.; Brown, M. G.; Carter, C.; Saykally, R. J.; Gregory, J. K.; Clary, D. C. *Nature* **1996,** *381,* 501.

[17] Wales, D. J. *J. Am. Chem. Soc.* **1993,** *115,* 11180.

[18] Eigen, M. *Angew. Chem. Int. Ed. Engl.* **1964,** *3,* 1.

[19] Campbell, E. E. B. Carbon Clusters. In *Clusters of Atoms and Molecules*, Vol. 1; Haberland, H., Ed.; Springer-Verlag: Berlin, 1994.

[20] Narcisi, R. S.; Bailey, A. D. *J. Geophys. Res.* **1965,** *70,* 3687.

[21] Ferguson, E. E.; Fehsenfeld, F. C.; Albritton, D. L. . In *Gas Phase Ion Chemistry*, Vol. 1; Bowers, M. T., Ed.; Academic: New York, 1979.

[22] Baciou, L.; Michel, H. *Biochemistry* **1995,** *34,* 3697.

[23] Jeffrey, G. A.; Saenger, W. *Hydrogen bonding in biological structures;* Springer-Verlag: Berlin, 1991.

[24] Schuster, P.; Zundel, G.; Sandorfy, C., Eds.; *The Hydrogen Bond: Recent Developments in Theory and Experiment;* volume 1 North-Holland Publishing Group: New York, 1976.

[25] Schuster, P.; Zundel, G.; Sandorfy, C., Eds.; *The Hydrogen Bond: Recent Developments in Theory and Experiment;* volume 2 North-Holland Publishing Group: New York, 1976.

[26] von Grotthuss, C. *Ann. Chim.* **1806,** *LVIII,* 54.

[27] Atkins, P. W. *Physical Chemistry;* Oxford University Press: London, 5 ed.; 1994.

[28] Eigen, M.; Maeyer, L. D. *Proc. Roy. Soc. A.* **1958,** *247,* 505.

[29] Eigen, M. *Angew. Chem.* **1963,** *75,* 489.

[30] Weidemann, E. G.; Zundel, G. *Z. Physik* **1967,** *198,* 288.

[31] Zundel, G.; Metzger, H. *Z. Phys. Chem.* **1968,** *58,* 225.

[32] Zundel, G. *Hydration and Intermolecular Interaction - Infrared Investigations of Polyelectrolyte Membranes;* Academic: New York, 1969.

[33] Zundel, G. *Allgem. Prakt. Chem. (Wien)* **1970,** *21,* 329.

[34] Kebarle, P.; Godbole, E. W. *J. Chem. Phys.* **1963,** *39,* 1131.

[35] Kebarle, P.; Hogg, A. M. *J. Chem. Phys.* **1965,** *42,* 798.

[36] Kebarle, P.; Searles, S. K.; Zolla, A. *J. Am. Chem. Soc.* **1967,** *89,* 7393.

[37] Cunningham, A. J.; Payzant, J. D.; Kebarle, P. *J. Am. Chem. Soc.* **1972,** *89,* 7627.

[38] Ojamäe, L.; Shavitt, I.; Singer, S. J. *Int. J. Quant. Chem.* **1995,** *29,* 657.

[39] Beggs, D. P.; Field, F. H. *J. Am. Chem. Soc.* **1971,** *93,* 1567.

[40] De Paz, M.; Levanthal, J. J.; Friedman, L. *J. Chem. Phys.* **1969,** *51,* 3748.

[41] De Paz, M.; Friedman, A. G. G. L. *J. Chem. Phys.* **1970,** *52,* 687.

[42] Schwarz, H. A. *J. Chem. Phys.* **1977,** *67,* 5525.

[43] Newton, M. D. *J. Chem. Phys.* **1977,** *67,* 5535.

[44] Okumura, M.; Yeh, L. I.; Myers, J. D.; Lee, Y. T. *J. Chem. Phys.* **1986,** *85,* 2328.

[45] Yeh, L. I.; Okumura, M.; Myers, J. D.; Price, J. M.; Lee, Y. T. *J. Chem. Phys.* **1989,** *91,* 7319.

[46] Okumura, M.; Yeh, L. I.; Myers, J. D.; Lee, Y. T. *J. Phys. Chem.* **1990,** *94,* 3416.

[47] Crofton, M. W.; Price, J. M.; Lee, Y. T. IR Spectroscopy of Hydrogen Bonded Charged Clusters. In *Clusters of Atoms and Molecules*, Vol. 2; Haberland, H., Ed.; Springer-Verlag: Berlin, 1994.

[48] Jiang, J.-C.; Wang, Y.-S.; Chang, H.-C.; Lin, S. H.; Lee, Y. T. *J. Am. Chem. Soc.* **2000,** *122,* 1398.

[49] Searcy, J. Q.; Fenn, J. B. *J. Chem. Phys.* **1974,** *61,* 5282.

[50] Sloan Jr., E. D. *Clathrate hydrates of natural gases;* Marcel Dekker: New York, 1990.

[51] Kraemer, W. P.; Diercksen, G. H. F. *Chem. Phys. Lett.* **1970,** *5,* 3362.

[52] Kollman, P. A.; Allen, L. C. *J. Am. Chem. Soc.* **1970,** *92,* 6101.

[53] De Paz, M.; Ehrenson, S.; Friedman, L. *J. Chem. Phys.* **1970,** *1970,* 3362.

[54] Newton, M. D.; Ehrenson, S. *J. Am. Chem. Soc.* **1971,** *93,* 4971.

[55] Fang, J. K.; Godzik, K.; Hofacker, G. F. *Ber. Bunsenges Phys. Chem.* **1973,** *77,* 908.

[56] Del Bene, J. E.; Frisch, M. J.; Pople, J. A. *J. Phys. Chem.* **1985,** *89,* 3669.

[57] Frisch, M. J.; Del Bene, J. E.; Binkley, J. S.; Schaefer III, H. F. *J. Chem. Phys.* **1986,** *84,* 2279.

[58] Lee, E. P. F.; Dyke, J. M. *Mol. Phys.* **1991,** *73,* 375.

[59] Xie, Y.; Remington, R. B.; Schaefer III, H. F. *J. Chem. Phys.* **1994,** *101,* 4878.

[60] Valeev, E. F.; Schaefer III, H. F. *J. Chem. Phys.* **1998,** *108,* 7197.

[61] Rahmouni, A.; Kochanski, E.; Weist, R.; Wormer, P. E. S.; Langlet, J. *J. Chem. Phys.* **1990,** *93,* 6648.

[62] Corongiu, G.; Kelterbaum, R.; Kochanski, E. *J. Phys. Chem.* **1995,** *99,* 8038.

[63] United Nations Environment Programme, "Montreal Protocol on Substances That Deplete the Ozone Layer", http://www.unep.org/ozone/pdfs/Montreal-Protocol2000.pdf.

[64] Ojamäe, L.; Shavitt, I.; Singer, S. J. *J. Chem. Phys.* **1998,** *109,* 5547.

[65] Ciobanu, C. V.; Ojmäe, L.; Shavitt, I.; Singer, S. J. *J. Chem. Phys.* **2000,** *113,* 5321.

[66] Singer, S. J.; McDonald, S.; Ojamäe, L. *J. Chem. Phys.* **2000,** *112,* 710.

[67] Geissler, P. L.; Dellago, C.; Chandler, D.; Hutter, J.; Parrinello, M. *Chem. Phys. Lett.* **2000,** *321,* 225.

[68] Stillinger, F. H.; Weber, T. A. *Chem. Phys. Lett.* **1981,** *79,* 259.

[69] Kozack, R. E.; Jordan, P. C. *J. Chem. Phys.* **1993,** *99,* 2978.

[70] Halley, J. W.; Rustad, J. R.; Rahman, A. *J. Chem. Phys.* **1993,** *98,* 4110.

[71] Lobaugh, J.; Voth, G. A. *J. Chem. Phys.* **1997,** *106,* 2400.

[72] Sagnella, D. E.; Tuckerman, M. E. *J. Chem. Phys.* **1998,** *108,* 2073.

[73] Schmitt, U. W.; Voth, G. A. *J. Phys. Chem. B* **1998,** *102,* 5547.

[74] Schmitt, U. W.; Voth, G. A. *J. Chem. Phys.* **1999,** *111,* 9361.

[75] Vuilleumier, R.; Borgis, D. *J. Mol. Struct.* **1997,** *436,* 555.

[76] Vuilleumier, R.; Borgis, D. *Chem. Phys. Lett.* **1998,** *284,* 71.

[77] Warshel, A. *Computer Modeling of Chemical Reactions in Enzymes and Solutions;* John Wiley and Sons: New York, 1991.

[78] Hodges, M. P.; Stone, A. J. *J. Chem. Phys.* **1999,** *110,* 6766.

[79] Shevkunov, S. V.; Girskii, D. V. *Colloid J. USSR* **1998,** *60,* 104.

[80] Shevkunov, S. V.; Vegiri, A. *J. Chem. Phys.* **1999,** *102,* 9303.

[81] Diercksen, G. H. F.; Kramer, W. P.; Roos, B. O. *Theoret. Chim. Acta* **1975,** *36,* 249.

[82] Scheiner, S. *J. Am. Chem. Soc.* **1981,** *103,* 315.

[83] Stillinger, F. H.; David, C. W. *J. Chem. Phys.* **1978,** *69,* 1473.

[84] Tuckerman, M.; Laasonen, K.; Sprik, M.; Parinello, M. *J. Chem. Phys.* **1995,** *103,* 150.

[85] Wei, D.; Salahub, D. R. *J. Chem. Phys.* **1994,** *101,* 7633.

[86] Geissler, P. L.; Dellago, C.; Chandler, D. *Phys. Chem. Chem. Phys.* **1999,** *1,* 1317.

[87] Becke, A. D. *Phys. Rev. A* **1988,** *38,* 3098.

[88] Perdew, J. P. *Phys. Rev. B* **1986,** *33,* 8822.

[89] Perdew, J. P. *Phys. Rev. B* **1986,** *38,* 7406.

[90] Kim, K.; Jordan, K. D. *J. Phys. Chem.* **1994,** *98,* 10089.

[91] Sim, F.; St.-Amant, A.; Papai, I.; Salahub, D. R. *J. Am. Chem. Soc.* **1992,** *114,* 4391.

[92] Laasonen, K.; Csajka, F.; Parinello, M. *Chem. Phys. Lett.* **1992,** *194,* 172.

[93] Laasonen, K.; Parinello, M.; Car, R.; Lee, C.; Vanderbilt, D. *Chem. Phys. Lett.* **1993,** *207,* 208.

[94] Becke, A. D. *J. Chem. Phys.* **1993,** *98,* 5648.

[95] Lee, C.; Yang, W.; Parr, R. *Phys. Rev. B* **1993,** *37,* 785.

[96] Frisch, M. J. *et al.* "Gaussian 98 (Revision A.1)", Gaussian Inc., Pittsburgh, PA, 1998.

[97] Brooks, B. R.; Bruccoleri, R. E.; Olafson, B. D.; States, D. J.; Swaminathan, S.; Karplus., M. *J. Comput. Chem.* **1983,** *4,* 1987.

[98] Dunning Jr., T. H. *J. Chem. Phys.* **1989,** *90,* 1007.

[99] Kendall, R. A.; Dunning Jr., T. H.; Harrison, R. J. *J. Chem. Phys.* **1992,** *96,* 6796.

[100] Boys, S. F.; Bernardi, F. *Mol. Phys.* **1970,** *19,* 553.

[101] Pedulla, J. M.; Kim, K.; Jordan, K. D. *Chem. Phys. Lett.* **1998,** *291,* 78.

[102] Xantheas, S. S. *J. Chem. Phys.* **1996,** *104,* 8821.

[103] Ayotte, P.; Johnson, M. A. *J. Chem. Phys.* **1997,** *106,* 811.

[104] Ayotte, P.; Weddle, G. H.; Bailey, C. G.; Johnson, M. A.; Vila, F. D.; Jordan, K. D. *J. Chem. Phys.* **1999,** *110,* 6268.

[105] Jongma, R. T.; Huang, Y.; Shiming, S.; Wodkte, A. *J. Phys. Chem. A* **1998,** *102,* 8847.

[106] Bruderman, J.; Buck, U.; Buch, V. *J. Phys. Chem. A* **2002,** *106,* 453.

[107] Tsai, C.-J.; Jordan, K. D. *J. Chem. Phys.* **1991,** *95,* 3850.

[108] Tsai, C.-J.; Jordan, K. D. *J. Chem. Phys.* **1993,** *99,* 6957.

[109] Laria, D.; Rodriguez, J.; Dellago, C.; Chandler, D. *J. Phys. Chem. A* **2001,** *105,* 2646.

[110] Wales, D. J.; Ohmine, I. *J. Chem. Phys.* **1993,** *98,* 7245.

[111] Rodriguez, J.; Laria, D.; Marceca, E. J.; Estrin, D. A. *J. Chem. Phys.* **1999,** *110,* 9039.

[112] Nigra, P.; Carignano, M. A.; Kais, S. *J. Chem. Phys.* **2001,** *115,* 2621.

[113] Tharrington, A.; Jordan, K. D. *J. Phys. Chem. A* **2003,** *107,* 7380.

[114] Neirotti, J. P.; Calvo, F.; Freeman, D. L.; Doll, J. D. *J. Chem. Phys.* **2000,** *112,* 10340.

[115] Tsai, C.-J.; Jordan, K. D. *J. Phys. Chem.* **1993,** *97,* 11227.

[116] Marx, D.; Tuckerman, M. E.; Hutter, J.; Parinello, M. *Nature* **1999,** *397,* 601.

[117] Svanberg, M.; Pettersson, J. B. C. *J. Phys. Chem. A* **1998,** *102,* 1865.

[118] Kusaka, I.; Oxtoby, D. W. *J. Chem. Phys.* **2000,** *113,* 10100.

[119] Frantz, D. D.; Freeman, D. L.; Doll, J. D. *J. Chem. Phys.* **1990,** *93,* 2769.

[120] Wales, D. J.; Ohmine, I. *J. Chem. Phys.* **1993,** *98,* 7257.

[121] Metropolis, N.; Rosenbluth, A. W.; Rosenbluth, M. N.; Teller, A. N. *J. Chem. Phys.* **1953,** *21,* 1087.

[122] Jorgensen, W. L.; Chandrasekhar, J.; Madura, J.; Impey, R.; Klein, M. L. *J. Chem. Phys.* **1983,** *79,* 926.

[123] Hodges, M. P.; Wales, D. J. *Chem. Phys. Lett.* **1999,** *324,* 279.

[124] Stone, A. J.; Dullweber, A.; Hodges, M. P.; Popelier, P. L.; Wales, D. J. "ORIENT: A program for studying interactions between molecules, Version 3.2", 1995 Available at http://fandango.chem.cam.ac.uk.

[125] Wei, D.; Salahub, D. R. *J. Chem. Phys.* **1989,** *90,* 1007.

[126] McDonald, S.; Ojamäe, L.; Singer, S. J. *J. Phys. Chem. A* **1998,** *102,* 2824.

[127] Kim, K.; Jordan, K. D.; Zwier, T. S. *J. Am. Chem. Soc.* **1994,** *116,* 11568.

[128] Xantheas, S. S.; Dunning Jr., T. H. *J. Chem. Phys.* **1993,** *98,* 8037.

[129] Del Bene, J.; Pople, J. A. *J. Chem. Phys.* **1970,** *52,* 4858.

[130] Kim, K. S.; Dupuis, M.; Lie, G. C.; Clementi, E. *Chem. Phys. Lett.* **1986,** *131,* 451.

[131] Honegger, E.; Leutwyler, S. *J. Chem. Phys.* **1988,** *88,* 2582.

[132] Smith, B. J.; Swanton, D. J.; Pople, J. A.; Schaefer III, H. F.; Radom, L. *J. Chem. Phys.* **1990,** *92,* 1240.

[133] Feller, D. *J. Chem. Phys.* **1992,** *96,* 6104.

[134] Millot, C.; Stone, A. J. *J. Mol. Phys.* **1992,** *77,* 439.

[135] Xantheas, S. S.; Dunning Jr., T. H. *J. Chem. Phys.* **1993,** *99,* 8774.

[136] Chakravorty, S. J.; Davidson, E. R. *J. Phys. Chem.* **1993,** *97,* 6373.

[137] Fowler, J. E.; Schaefer III, H. F. *J. Am. Chem. Soc.* **1995,** *117,* 446.

[138] Feyereisen, M. W.; Feller, D.; Dixon, D. A. *J. Phys. Chem.* **1996,** *100,* 2993.

[139] Wales, D. J. *Science* **1996,** *271,* 925.

[140] Hodges, M. P.; Stone, A. J.; Xantheas, S. S. *J. Phys. Chem. A* **1997,** *101,* 9163.

[141] Nielsen, I. M. B.; Siedi, E. T.; Janssen, C. L. *J. Chem. Phys.* **1999,** *110,* 9435.

[142] Mó, O.; Yánez, M.; Elguero, J. *J. Chem. Phys.* **1992,** *97,* 6628.

[143] Xantheas, S. S. *J. Chem. Phys.* **1994,** *100,* 7523.

[144] Gregory, J. K.; Clary, D. C. *J. Phys. Chem.* **1996,** *100,* 18014.

[145] Pedulla, J. M.; Vila, F. D.; Jordan, K. D. *J. Chem. Phys.* **1996,** *105,* 11091.

[146] Masella, M.; Flament, J. P. *J. Chem. Phys.* **1997,** *107,* 9105.

[147] Millot, C.; Soetens, J. C.; Costa, M. T. M. C.; Hodges, M. P.; Stone, A. J. *J. Phys. Chem. A* **1998,** *102,* 754.

[148] Pedulla, J. M.; Kim, K.; Jordan, K. D. *Chem. Phys.* **1998,** *239,* 593.

[149] Dyke, T. R.; Muenter, J. S. *J. Chem. Phys.* **1972,** *57,* 5011.

[150] Dyke, T. R.; Muenter, J. S. *J. Chem. Phys.* **1974,** *60,* 2929.

[151] Dyke, T. R.; Mack, K. M.; Muenter, J. S. *J. Chem. Phys.* **1977,** *66,* 498.

[152] Odutola, J. A.; Dyke, T. R. *J. Chem. Phys.* **1980,** *72,* 5062.

[153] Pugliano, N.; Saykally, R. J. *Science* **1992,** *257,* 1937.

[154] Pugliano, N.; Cruzan, J. D.; Loeser, J. G.; Saykally, R. J. *J. Chem. Phys.* **1993,** *98,* 6600.

[155] Pribble, R. N.; Zwier, T. S. *Science* **1994,** *265,* 75.

[156] Cruzan, J. D.; Braly, L. B.; Liu, K.; Brown, M. G.; Loeser, J. G.; Saykally, R. J. *Science* **1996,** *271,* 59.

[157] Cruzan, J. D.; Braly, L. B.; Liu, K.; Brown, M. G.; Loeser, J. G.; Saykally, R. J. *J. Phys. Chem. A* **1997,** *101,* 9022.

[158] Viant, M. R.; Cruzan, J. D.; Lucas, D. D.; Brown, M. G.; Liu, K.; Saykally, R. J. *J. Phys. Chem. A* **1997,** *101,* 9032.

[159] Walsh, T.; Wales, D. *J. Chem. Soc. Faraday Trans.* **1996,** *92,* 2505.

[160] Wales, D. J. Dynamics and Rearrangements of Water Clusters. In *Advances in Molecular Vibrations and Collision Dynamics*; Bowman, J.; Bacic, Z., Eds.; JAI press: Stamford, 1998.

[161] David, C. W. *J. Chem. Phys.* **1980,** *73,* 5395.

[162] Vegiri, S.; Farantos, S. C. *J. Chem. Phys.* **1993,** *98,* 4059.

[163] Saykally, R. J.; Blake, G. A. *Science* **1993,** *259,* 1937.

[164] Matsuoka, O.; Clementi, E.; Yoshimine, M. *J. Chem. Phys.* **1976,** *64,* 1351.

[165] Clementi, E.; Corongiu, G. *Intern. J. Quantum Chem.* **1983,** *S10,* 31.

[166] Detrich, J.; Corongiu, G.; Clementi, E. *Chem. Phys. Lett.* **1984,** *112,* 426.

[167] Belford, D. E.; Campbell, E. S. *J. Chem. Phys.* **1987,** *86,* 7013.

[168] Campbell, E.; Mezei, M. *J. Chem. Phys.* **1977,** *67,* 2338.

[169] Schröder, K.-P. *Chem. Phys.* **1988,** *123,* 91.

[170] Sauer, J. Thesis, Academy of Sciences of the GDR, 1985.

[171] Dykstra, C. E. *J. Chem. Phys.* **1989,** *91,* 6472.

[172] Franken, K. A.; Jalaie, M.; Dykstra, C. E. *Chem. Phys. Lett.* **1992,** *198,* 59.

[173] Dykstra, C. E. *J. Am. Chem. Soc.* **1989,** *111,* 6168.

[174] Dykstra, C. E. *J. Comput. Chem* **1988,** *9,* 476.

[175] Cieplak, P.; Kollman, P.; Lybrand, T. *J. Chem. Phys.* **1990,** *92,* 6755.

[176] Wales, D. J.; Doye, J. P. K.; Miller, M. A.; Mortensen, P. N.; Walsh, T. R. *Adv. Chem. Phys.* **2000,** *115,* 1.

[177] Burnham, C. J.; Xantheas, S. S. *J. Chem. Phys.* **2002,** *116,* 1500.

[178] Burnham, C. J.; Xantheas, S. S. *J. Chem. Phys.* **2002,** *116,* 5115.

[179] Tissandier, M. D.; Singer, S. J.; Coe, J. V. *J. Phys. Chem. A* **2000,** *104,* 752.

[180] Kim, K. S.; Mhin, B. J.; Choi, U.-S.; Lee, K. *J. Chem. Phys.* **1992,** *97,* 6649.

[181] Tsai, C. J.; Jordan, K. D. unpublished results.

[182] Mhin, B. J.; Kim, J.; Lee, S.; Lee, J. Y.; Kim, K. S. *J. Chem. Phys.* **1994,** *100,* 4484.

[183] Kim, J.; Kim, K. S. *J. Chem. Phys.* **1998,** *117,* 5886.

[184] Xantheas, S. S.; Burnham, C. J.; Harrison, R. J. *J. Chem. Phys.* **2002,** *116,* 1493.

[185] Kryachko, E. S. *Chem. Phys. Lett.* **1999,** *314,* 353.

[186] Losada, M.; Leutwyler, S. *J. Chem. Phys.* **2002,** *117,* 2003.

[187] Krishnan, P. N.; Jensen, J. O.; Burke, L. A. *Chem. Phys. Lett.* **1994,** *217,* 311.

[188] Lee, C.; Chen, H.; Fitzgerald, G. *J. Chem. Phys.* **1994,** *101,* 4472.

[189] Severson, M. W.; Buch, V. *J. Chem. Phys.* **1999,** *111,* 10866.

[190] Diri, K.; Myshakin, E. M.; Jordan, K. D. submitted to J. Phys. Chem. A.

[191] Gregory, J. K.; Clary, D. C.; Liu, K.; Brown, M. G.; Saykally, R. J. *Science* **1997,** *275,* 814.

[192] Diken, E. G.; Robertson, W. H.; Johnson, M. A. *J. Phys. Chem. A* **2004,** *108,* 64.

[193] Steinbach, C.; Andersson, P.; Melzer, M.; Kazimirski, J. K.; Buck, U.; Buch, V. *Phys. Chem. Chem. Phys.* **2004,** *6,* 3320.

[194] Nauta, K.; Miller, R. E. *Science* **2000,** *287,* 293.

[195] Burnham, C. J.; Xantheas, S. S.; Miller, M. A.; Applegate, B. E.; Miller, R. E. *J. Chem. Phys.* **2002,** *117,* 1109.

[196] Ren, P.; Ponder, J. W. *J. Phys. Chem. B* **2003,** *107,* 5933.

[197] Jordan, K. D. unpublished results.

[198] Kristyán, S.; Pulay, P. *Chem. Phys. Lett.* **1994,** *229,* 175.

[199] Pérez-Jordá, J. M.; Becke, A. D. *Chem. Phys. Lett.* **1995,** *233,* 134.

[200] Pulay, P. *Chem. Phys. Lett.* **1983,** *100,* 151.

[201] Pulay, P.; Saebø, S. *Theor. Chim. Acta.* **1986,** *69,* 357.

[202] Saebø, S.; Pulay, P. *J. Chem. Phys.* **1987,** *86,* 914.

[203] Saebø, S.; Pulay, P. *Annu. Rev. Phys. Chem.* **1993,** *44,* 213.

[204] Weigend, F.; Häser, M. *Theor. Chem. Acc.* **1997,** *97,* 331.

[205] Weigend, F.; Häser, M.; Patzelt, H.; Ahlrichs, R. *Chem. Phys. Letters* **1998,** *294,* 143.

[206] Challacombe, M.; Schwegler, E. "MondoSCF a suite of programs for linear scaling SCF theory", 1999.

[207] Niesar, U.; Corongiu, G.; Huang, M.-J.; Dupuis, M.; Clementi, E. *Int. J. Quantum Chem. Symp.* **1989,** *23,* 421.

[208] Niesar, U.; Corongiu, G.; Clementi, E.; Kneller, G. R.; Bhattacharya, D. K. *J. Phys. Chem.* **1990,** *94,* 7949.

[209] Mas, E. M.; Szalewicz, K.; Bukowski, R.; Jeziorski, B. *J. Chem. Phys.* **1997,** *107,* 4207.

[210] Mas, E. M.; Bukowski, R.; Szalewicz, K.; Groenenboom, G.; Wormer, P. E. S.; van der Avoird, A. *J. Chem. Phys.* **2000,** *113,* 6687.

[211] Mas, E. M.; Bukowski, R.; Szalewicz, K. *J. Chem. Phys.* **2003,** *118,* 4404.

[212] "Jaguar 4.2, Schrödinger, Inc., Portland, OR", 1991-2000.

[213] Hehre, W. J.; Ditchfield, R.; Pople, J. A. *J. Chem. Phys.* **1972,** *56,* 2257.

[214] Clark, T.; Chandrasekhar, J.; Spitznagel, G. W.; v. R. Schleyer, P. *J. Comp. Chem.* **1983,** *4,* 294.

[215] Frisch, M.; Pople, J.; Binkley, J. *J. Chem. Phys.* **1984,** *80,* 3265.

[216] Amos, R. D. *et al.* "MOLPRO, a package of ab initio programs designed by H.-J.Werner and P. J. Knowles, version 2002.3", 2002.

[217] Ferrenberg, A. M.; Swendsen, R. H. *Phys. Rev. Lett.* **1988,** *61,* 2635.

[218] Hura, G.; Sorenson, J. M.; Glaeser, R. M.; Head-Gordon, T. *J. Chem. Phys.* **2000,** *113,* 9140.

[219] Zundel, G. . In *The Hydrogen Bond - Recent Developments in Theory and Experiments. II. Structure and Spectroscopy*; : , 1976.

[220] Agmon, N. *Chem. Phys. Lett.* **1995,** *244,* 456.

[221] Castleman Jr., A. W.; Bowen Jr., K. H. *J. Phys. Chem.* **1996,** *100,* 12911.

[222] Kassner Jr., J. L.; Hagen, D. E. *J. Chem. Phys.* **1976,** *64,* 1860.

[223] Khan, A. *Chem. Phys. Lett.* **2000,** *319,* 440.

[224] Begemann, M. H.; Gudeman, C. S.; Pfaff, J.; Saykally, R. J. *Phys. Rev. Lett.* **1983,** *51,* 554.

[225] Laasonen, K.; Klein, M. L. *J. Phys. Chem.* **1994,** *98,* 10079.

[226] Kelterbaum, R.; Kochanski, E. *J. Mol. Struc. (THEOCHEM)* **1996,** *371,* 205.

[227] Asmis, K. R.; Pivonka, N. L.; Santambrogio, G.; Brümmer, M.; Kaposta, C.; Neumark, D. M.; Wöste, L. *Science* **2003,** *299,* 1375.

[228] Davidson, D. W. . In *Water: A Comprehensive Treatise*, Vol. 2; Franks, F., Ed.; Plenum: New York, 1973.

[229] Johnson, M. S.; Kuwata, K. T.; Wong, C.-K.; Okumura, M. *Chem. Phys. Lett.* **1996,** *260,* 551.

[230] Johnson, M. A.; Lineberger, W. C. . In *Techniques for the Study of Ion-Molecule Reactions*, Vol. XX; Farrar, J. J. M.; Saunders, W. H., Eds.; Wiley: New York, 1988.

[231] Duncan, M. A. *Int. Rev. Phys. Chem.* **2003,** *22,* 407.

[232] At Yale, the $H^+(H_2O)_n$ clusters were prepared in an electron beam-ionized supersonic expansion, while the Georgia ion source uses a pulsed laser plasma on a metal target located just outside the pulsed nozzle. The electron beam ion source is also pulsed and is operated under conditions close to the evaporative ensemble, and likely creates ions warmer than the laser plasma source when operated in this mode. The two spectrometers differ in the timescales required for dissociation upon photoexcitation, with the Yale system allowing about 15 ms after excitation while the Georgia instrument is sensitive to decay in 1 to 2 ms. Both instruments use infrared light generated by a pulsed Nd:YAG-pumped OPO/OPA (LaserVision) laser. All features reported

here are observed independently under all conditions. It is interesting to note that the laser plasma source (Georgia) yields similar vibrational spectra even though the intensity profile of $H^+(H_2O)_n$ clusters does not display a pronounced intensity anomaly at $n = 21$, as did the electron impact source, which yields the distribution shown in Fig. 1.

[233] Frisch, M. J. *et al.* "Gaussian 03, Revision B.03", Gaussian Inc., Pittsburgh, PA, 2003.

[234] The calculations were performed with the Becke3LYP density functional with the aug-cc-pVDZ† basis set, which was formed by omitting the diffuse functions from the H atoms in the full aug-cc-pVDZ basis set. The geometries were optimized using analytical gradients, and for each optimized structure, the vibrational frequencies and intensities were calculated in the harmonic approximation.

[235] Campagnola, P. J.; Posey, L. A.; Johnson, M. A. *J. Chem. Phys.* **1991,** *95,* 7998.

[236] Klots, C. E. *J. Chem. Phys.* **1985,** *83,* 5854.

[237] Shi, Z.; Ford, J. V.; Wei, S.; Castleman Jr., A. W. *J. Chem. Phys.* **1993,** *99,* 8009.

[238] Shin, J.-W.; Hammer, N. I.; Diken, E. G.; Johnson, M. A.; Walters, R. S.; Jaeger, T. D.; Duncan, M. A.; Christie, R. A.; Jordan, K. D. paper presented at the 227th American Chemical Society National Meeting, Anaheim, CA, 31 March 2004.

[239] Zwier, T. *J. Phys. Chem. A* **2001,** *105,* 8827 and references therein.

[240] Carney, J. R.; Zwier, T. S. *J. Phys. Chem. A* **2000,** *104,* 8677.

[241] Carney, J.; Zwier, T. *Chem. Phys. Lett.* **2001,** *341,* 77.

[242] Robertson, E.; Hockridge, M.; Jelfs, P.; Simons, J. *J. Phys. Chem. A* **2000,** *104,* 11714.

[243] Snoek, L.; Kroemer, R.; Hockridge, M.; Simons, J. *Phys. Chem. Chem. Phys.* **2001,** *3,* 1819.

[244] Unamuno, I.; Fernndez, J. A.; Longarte, A.; Castao, F. J. *Phys. Chem. A* **2000,** *104,* 4364.

[245] Robertson, E.; Simons, J. *Phys. Chem. Chem. Phys.* **2001,** *3,* 1 and references therein.

[246] Ruoff, R.; Klots, T.; Emilsson, T.; Gutowsky, H. *J. Chem. Phys.* **1990,** *93,* 3142-3150.

[247] Godfrey, P. D.; Brown, R. D.; Rodgers, F. M. *J. Mol. Struct.* **1996,** *376,* 65.

[248] Godfrey, P. D.; Brown, R. D. *J. Am. Chem. Soc.* **1998,** *120,* 10724.

[249] Scherer, G.; Kramer, M.; Schutkowski, M.; Reimer, U.; Fischer, G. *J. Am. Chem. Soc.* **1998,** *120,* 5568.

[250] Schiene-Fischer, C.; Fischer, G. *J. Am. Chem. Soc.* **2001,** *123,* 6227.

[251] Li, P.; Chen, X. G.; Shulin, E.; Asher, S. *J. Am. Chem. Soc.* **1997,** *119,* 1116.

[252] Mor, M.; Plazzi, P.; Spadoni, G.; Tarzia, G. *Current Medicinal Chemistry* **1999,** *6,* 501 and references therein.

[253] Reiter, R. *Endocrine Rev.* **1991,** *12,* 151.

[254] Jansen, J.; Copinga, S.; Gruppen, G.; Molinari, E.; Dubocovich, M.; Grol, C. *Bioorganic Med. Chem.* **1996,** *4,* 1321.

[255] Grol, C.; Jansen, J. *Bioorganic Med. Chem.* **1996,** *4,* 1333.

[256] Sicsic, S.; Serraz, I.; Andrieux, J.; Bremont, B.; Mathe-Allainmat, M.; Poncet, A.; Shen, S.; Langlois, M. *J. Med. Chem.* **1997,** *40,* 739.

[257] Butz, P.; Kroemer, R. T.; MacLeod, N. A.; Simons, J. P. *J. Phys. Chem. A* **2001,** *105,* 544.

[258] Dian, B.; Longarte, A.; Mercier, S.; Zwier, T. 2002 In preparation.

[259] Dian, B. C.; Longarte, A.; Zwier, T. S. *Science* **2002,** *296,* 2369.

[260] Park, Y.; Rizzo, T.; Peteanu, L.; Levy, D. *J. Chem. Phys.* **1986,** *84,* 6539.

[261] Tubergen, M.; Cable, J.; Levy, D. *J. Chem. Phys.* **1990,** *92,* 51.

[262] Cannington, P. H.; Ham, N. S. *J. Electron Spectrosc. Relat. Phenom.* **1983,** *32,* 139.

[263] Beachy, M.; Chasman, D.; Murphy, R.; Halgren, T.; Friesner, R. *J. Am. Chem. Soc.* **1997,** *119,* 5908 and references therein.

[264] Mohamadi, F.; Richard, N.; Guida, W.; Liskamp, R.; Lipton, M.; Caufield, C.; Chang, G.; Hendrickson, T.; Still, W. *J. Comput. Chem.* **1990,** *11,* 440.

[265] Jorgensen, W.; Maxwell, D.; Tirado-Rives, J. *J. Am. Chem. Soc.* **1996,** *118,* 11225.

[266] Lee, C.; Yang, W.; Parr, R. G. *Phys. Rev. B* **1988,** *37,* 785.

[267] Saebø, S.; Pulay, P. *Theor. Chim. Acta.* **1986,** *69,* 357.

[268] Woon, D. E.; Dunning Jr., T. H. *J. Chem. Phys.* **1993,** *98,* 1358.

[269] Murphy, R. B.; Beachy, M. D.; Friesner, R. A.; Ringnalda, M. N. *J. Chem. Phys.* **1995,** *103,* 1481.

[270] Pipek, J.; Mezey, P. G. *J. Chem. Phys.* **1989,** *90,* 4916.

[271] Vasilescu, D.; Broch, H. *J. Mol. Struct. (THEOCHEM)* **1999,** *460,* 191.

[272] Sastre, J. L.; Miguel, R.; Molina, R.; Zarzuelo, M.; Romero-Avila, C.; Ramos, A. *J. Mol. Struct. (Theochem)* **2001,** *537,* 271.

[273] Florio, G.; Zwier, T. In preparation.

[274] Huang, Y.; Sulkes, M. *J. Phys. Chem.* **1996,** *100,* 16479.

[275] Carney, J. R.; Hagemeister, F. C.; Zwier, T. S. *J. Phys. Chem. A* **1999,** *103,* 9943.

[276] Carney, J.; Hagemeister, F.; Zwier, T. *J. Chem. Phys.* **1998,** *108,* 3379.

[277] Arnold, S.; Sulkes, M. *Chem. Phys. Lett.* **1992,** *200,* 125.

[278] Sulkes, M. 2001.

[279] Spadoni, G.; Mor, M.; Tarzia, G. *Biol. Signals Recept.* **1999,** *8,* 15.

[280] Carney, J.; Dian, B.; Florio, G.; Zwier, T. *J. Am. Chem. Soc.* **2001,** *123,* 5596.